

Measurement of the $K^+ \rightarrow \pi^+ \nu \bar{\nu}$ Branching Ratio

The E949 Collaboration

Abstract

The E949 experiment at Brookhaven National Laboratory (BNL) has collected a data sample equivalent to 1.77×10^{12} K^+ decays at rest during its 2002 physics run. These data were analyzed via a blind analysis in order to obtain an unbiased background estimate in the signal box for the rare kaon $K^+ \rightarrow \pi^+ \nu \bar{\nu}$ of 0.30 ± 0.02 events. One candidate event is observed, giving an upper limit for the branching ratio $\mathcal{B}(K^+ \rightarrow \pi^+ \nu \bar{\nu}) < 8.8 \times 10^{-10}$ (90% CL). Combining with the other two candidate events observed by the predecessor E787 experiment gives the branching ratio $(1.47_{-0.93}^{+1.60}) \times 10^{-10}$, which is consistent with the Standard Model prediction of $(0.78 \pm 0.12) \times 10^{-10}$. The resulting limit on the magnitude of the Cabibbo-Kobayashi-Maskawa matrix element V_{td} is $0.0024 < |V_{td}| < 0.0322$.

Contents

1	Introduction	1
1.1	CP Violation and Rare Decay $K^+ \rightarrow \pi^+ \nu \bar{\nu}$	1
1.2	History of $K^+ \rightarrow \pi^+ \nu \bar{\nu}$ Experiments	5
2	Experimental Method	8
2.1	Overview	8
2.2	The Accelerator and K^+ Beam Line	9
2.3	Beam Counters	11
2.4	Target	14
2.5	Tracking chamber	15
2.6	Range Stack	17
2.6.1	Scintillator Counters	17
2.6.2	Straw chambers	19
2.6.3	Resolutions of energy and range	19
2.7	Photon veto counters	19
2.8	Trigger	22
2.8.1	Level-0	22
2.8.2	Level-1.1	23
2.8.3	Level-1.2	23
2.8.4	$K^+ \rightarrow \pi^+ \nu \bar{\nu}$ Triggers	23
2.8.5	Monitor Triggers	24
2.9	Data Acquisition	25
2.10	Data Collection	28
3	Data analysis	29
3.1	Overview of background	29
3.2	Analysis Strategy and Method	31
3.3	Track reconstruction and data processing	33
3.3.1	Track reconstruction	33
3.3.2	Data processing	35
3.4	Monte Carlo simulation	35
3.5	Selection criteria	37
3.5.1	Single K^+ beam selection criteria	37
3.5.2	Kinematic reconstruction	39
3.5.3	π^+ identification	44
3.5.4	Photon veto	49
3.6	Signal and background	51
3.6.1	Technique of background measurement	54
3.6.2	Determination of signal region	57
3.6.3	$K_{\pi 2}$ background	58
3.6.4	μ^+ background	61

3.6.5	Single beam background	63
3.6.6	Double beam background	64
3.6.7	Charge exchange background	64
3.6.8	Correlation study and single cut failure study	66
3.6.9	Summary of background	69
3.7	Examining the signal region	69
3.8	Background distributions inside the signal region	71
3.8.1	$K_{\mu 2}$ and $K_{\pi 2}$ background functions	71
3.8.2	Beam background functions	72
3.9	Acceptance measurement and sensitivity	72
3.9.1	Acceptance measurements	73
3.9.2	$K_{\pi 2}$ branching ratio measurement	73
3.9.3	Summary of acceptance and sensitivity	75
4	Branching ratio of $K^+ \rightarrow \pi^+ \nu \bar{\nu}$	76
4.1	Signal/noise cell definitions and likelihood estimator	76
4.2	Branching ratio of $K^+ \rightarrow \pi^+ \nu \bar{\nu}$	77
4.3	Estimation of systematic uncertainty	79
4.4	Implication for $BR(K^+ \rightarrow \pi^+ X^0)$	80
4.5	Impact of $K^+ \rightarrow \pi^+ \nu \bar{\nu}$ branching ratio on unitarity triangle	81
5	Conclusion	85

1 Introduction

The Standard Model (SM) has so far well explained almost of all the experimental results in particle physics. Despite this success, there are still some experimental observations which the SM cannot account for. The matter and antimatter asymmetry is one of these exceptions, for example, the cosmological baryon asymmetry in our universe[1]. According to Sakharov[2], one of necessary condition to generate such an asymmetry is that the elementary interaction violates charge conjugation symmetry (C) and the combined CP symmetry (where P is parity symmetry). However, the strength of asymmetry cannot be derived by the model calculations based on the SM[3]. Whether or not there are new sources of CP violation has been searched for many years in particle physics experiments. In this paper, we will detail the analysis of BNL-E949 experiment, which are mostly in common with BNL-E787 experiment.

This paper is arranged as following. We will first review CP violation and rare kaon decays. And then we will describe the sources of background and how we can suppress the background in designing the kaon beamline, the detector and the selection criteria in data analysis. We will describe our unique methods in estimating the background level and in evaluating the acceptance. After opening the signal box, we will present our method in extracting branching ratio, making full use of our knowledge on the background in the signal box. In the end of this paper, we will also show how the result of rare kaon decay can give an impact on discovery of the new physics beyond the SM.

1.1 CP Violation and Rare Decay $K^+ \rightarrow \pi^+ \nu \bar{\nu}$

In the Standard Model, CP violation in flavor changing processes is related to a imaginary phase in the quark mixing matrix[4], assuming that there are three generations of quarks. This matrix is known as the Cabibbo-Kobayashi-Maskawa (CKM) matrix. In Wolfenstein parameterization [5], the CKM matrix can be written in powers of $\lambda = \sin \theta_c = 0.22$:

$$V_{CKM} = \begin{pmatrix} V_{ud} & V_{us} & V_{ub} \\ V_{cd} & V_{cs} & V_{cb} \\ V_{td} & V_{ts} & V_{tb} \end{pmatrix} \simeq \begin{pmatrix} 1 - \lambda^2/2 & \lambda & A\lambda^3(\rho - i\eta) \\ -\lambda & 1 - \lambda^2/2 & A\lambda^2 \\ A\lambda^3(1 - \rho - i\eta) & -A\lambda^2 & 1 \end{pmatrix}. \quad (1)$$

Where A , λ , ρ and η are real numbers. CP invariance of the Lagrangian for weak interactions is violated when the CKM matrix is a complex one. The parameter η describes CP violation in the SM, since a non-zero value of the parameter η breaks the CP invariance for weak interactions.

The unitarity of the CKM matrix can be expressed in terms of six unitarity conditions, which can be represented graphically in the form of triangles, all of which must have the same area. The area of these triangles is equal to one half of the Jarlskog invariant, J_{CP} [7]. Applying the unitarity property $V^\dagger V = 1$ to the CKM matrix in (1) implies

$$V_{ub}^* V_{ud} + V_{cb}^* V_{cd} + V_{tb}^* V_{td} \simeq V_{ub}^* - \lambda V_{cb}^* + V_{td} = 0, \quad (2)$$

where the approximations $V_{ud} \simeq V_{tb}^* \simeq 1$ and $V_{cd} \simeq -\lambda$ have been made. This equation can be represented graphically, as shown in Figure 1, where we have divided all of the sides

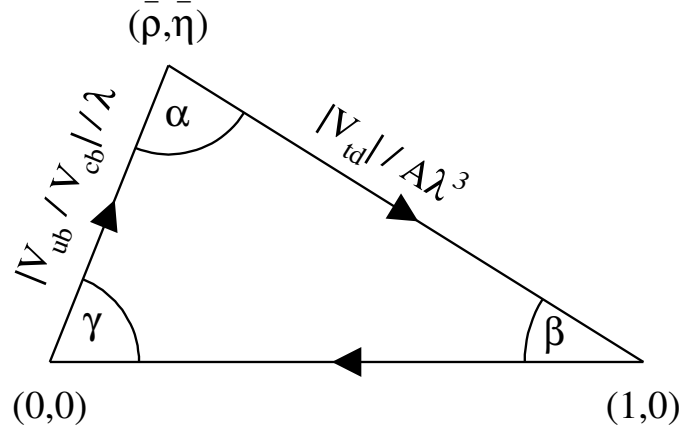


Figure 1: Unitarity triangles in the $\rho-\eta$ plane. Two sides of the triangle can be expressed by the CKM matrix elements $|V_{td}|/A\lambda^3$ and $|V_{ub}/V_{cb}|/\lambda$, respectively, where A and λ are parameters in the Wolfenstein parameterization.

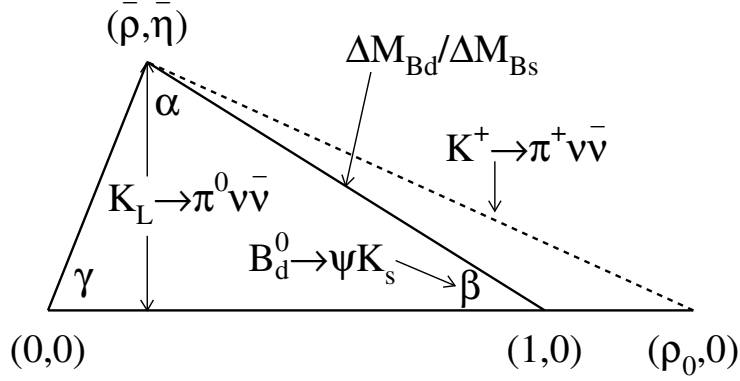


Figure 2: Unitarity triangle determined by B and K decays. The ρ and η can be determined by two ways: angle β from the CP violation asymmetry in the decay $B_d^0 \rightarrow J/\psi K_s^0$, and the length of the side from $\Delta M_{B_s}/\Delta M_{B_d}$ in $B^0 - \bar{B}^0$ mixing; the height of the triangle from $\mathcal{B}(K_L^0 \rightarrow \pi^0 \nu \bar{\nu})$ and the radius of a circle centered at $(\rho_0, 0)$ from $\mathcal{B}(K^+ \rightarrow \pi^+ \nu \bar{\nu})$.

by λV_{cb}^* . The apex of the triangle is given by two well-known Wolfenstein parameters, $\bar{\rho}$ and $\bar{\eta}$, where $\bar{\rho} = \rho(1 - \lambda^2/2)$ and $\bar{\eta} = \eta(1 - \lambda^2/2)$.

B and kaon are by now the only two mesons showing evidence of CP violation in their decay processes. Whether or not the observed CP violation can be explained by the CKM phase within the SM, the determination of ρ and η independently from B and K decays as shown in Figure 2 becomes very crucial. can be examined in two ways, as follows:

- A comparison of angle β from the ratio $\mathcal{B}(K_L^0 \rightarrow \pi^0 \nu \bar{\nu})/\mathcal{B}(K^+ \rightarrow \pi^+ \nu \bar{\nu})$ and from CP violation asymmetry (\mathcal{A}_{CP}) in the decay $B_d^0 \rightarrow J/\psi K_s^0$.
- A comparison of the magnitude $|V_{td}|$ from $K^+ \rightarrow \pi^+ \nu \bar{\nu}$ and from the mixing frequencies of B_s and B_d mesons, expressed in terms of the ratio of the mass differences, $\Delta M_{B_s}/\Delta M_{B_d}$.

Although the decay $K^+ \rightarrow \pi^+ \nu \bar{\nu}$ is a Flavor Changing Neutral Current (FCNC) process prohibited in the tree level and the first order of loop level, this decay is allowed in

the second order, and is described by a "Box" diagram and two "Z-penguin" diagrams, as shown in Figure 3. The weak amplitude for this process is represented as

$$\mathcal{M} \sim \sum_{i=u,c,t} V_{is}^* V_{id} \frac{\gamma^\mu q_\mu + m_i}{q^2 - m_i^2}, \quad (3)$$

where the V_{ij} 's are the CKM matrix elements, the γ^μ 's are the Dirac matrices, the q_μ is the momentum transfer, and the m_i 's are quark masses. \mathcal{M} vanishes if all of the quark masses, m_i , are equal, because of the unitarity of the CKM matrix. However, the breaking of flavor symmetry, which results in the different quark masses, allows this decay to proceed at a very small rate, especially the discovery of the top quark violates the quark mass equality at a maximum, giving a largest contribution to the $K^+ \rightarrow \pi^+ \nu \bar{\nu}$ branching ratio via the weak coupling of top to down quarks in term of V_{td} in the CKM matrix element.

The branching ratio for $K^+ \rightarrow \pi^+ \nu \bar{\nu}$ is calculated by following the convention in [8]. The effective Hamiltonian can be written in the SM as

$$\mathcal{H}_{eff}^{SM} = \frac{G_F}{\sqrt{2}} \frac{\alpha}{2\pi \sin^2 \Theta_W} \sum_{l=e,\mu,\tau} (V_{cs}^* V_{cd} X_{NL}^l + V_{ts}^* V_{td} X(x_t)) (\bar{s}d)_{V-A} (\bar{\nu}_l \nu_l)_{V-A}, \quad (4)$$

where

$$X(x_t) \equiv X_0(x_t) + \frac{\alpha_s(m_t)}{4\pi} X_1(x_t) = \eta_X \cdot X_0(x_t) \quad (5)$$

and

$$X_0(x_t) \equiv C_0(x_t) - 4B_0(x_t), \quad \eta_X = 0.995. \quad (6)$$

$B_0(x_j)$ and $C_0(x_j)$ in (6) are functions of $x_j \equiv m_j^2/M_W^2$, and were derived for the first time by Inami and Lim in 1981 [9]. The coefficient X_{NL}^l and the function $X(x_t)$ are the charm and top quark contributions, including QCD corrections at the next-leading-order (NLO) level [10, 11, 12].

With the top quark mass in the minimal subtraction (\overline{MS}) scheme $m_t = (168.1 \pm 4.1)$ GeV[8],

$$X(x_t) = 1.529 \pm 0.042 \quad (7)$$

is obtained.

The perturbative charm contribution gives the largest theoretical uncertainty and can be described in terms of the parameter

$$P_c(X) \equiv \frac{1}{\lambda^4} \left[\frac{2}{3} X_{NL}^e + \frac{1}{3} X_{NL}^\tau \right] = 0.39 \pm 0.07, \quad (8)$$

where $\lambda = \sin \theta_c$, and the error is obtained by varying the charm mass, m_c , the scale factor, $\mu_c = \mathcal{O}(m_c)$ and the coupling constant, $\alpha_s(M_Z^2)$, by certain amounts. Therefore, one can have

$$\mathcal{B}(K^+ \rightarrow \pi^+ \nu \bar{\nu}) = \kappa_+ \cdot \left[\left(\frac{\text{Im} \lambda_t}{\lambda^5} X(x_t) \right)^2 + \left(\frac{\text{Re} \lambda_c}{\lambda} P_c(X) + \frac{\text{Re} \lambda_t}{\lambda^5} X(x_t) \right)^2 \right], \quad (9)$$

$\lambda = V_{us} = 0.2240 \pm 0.0036$
$\bar{\rho} = 0.187 \pm 0.059$
$\bar{\eta} = 0.354 \pm 0.027$
$ V_{cb} = (41.5 \pm 0.8) \times 10^{-3}$
$ V_{ub}/V_{cb} = 0.092 \pm 0.014$
$ V_{td} = (8.24 \pm 0.54) \times 10^{-3}$
$A = V_{cb} /\lambda^2 = 0.827 \pm 0.016$
$\sin 2\beta = 0.732 \pm 0.049$
$m_t = 168.1 \pm 4.1 \text{ GeV}$
$X(x_t) = 1.529 \pm 0.042$
$P_c(X) = 0.389 \pm 0.073$
$\rho_0 = 1 + \lambda^4 P_c(X)/ V_{cb} ^2 X(x_t) = 1 + P_c(X)/A^2 X(x_t) = 1.373 \pm 0.068$
$\xi = f_{B_s} \sqrt{B_s}/f_{B_d} \sqrt{B_d} = 1.24 \pm 0.08$

Table 1: Parameters that are used in the SM prediction of the $\mathcal{B}(K^+ \rightarrow \pi^+ \nu \bar{\nu})$.

where

$$\kappa_+ \equiv r_+ \frac{3\alpha^2 \mathcal{B}(K^+ \rightarrow \pi^0 e^+ \nu)}{2\pi^2 \sin^4 \Theta_W} \lambda^8 = (4.84 \pm 0.06) \times 10^{-11} \left[\frac{\lambda}{0.224} \right]^8 \quad (10)$$

and the λ_j 's ($\equiv V_{js}^* V_{jd}$) are from the CKM matrix elements. The r_+ ($= 0.901$) represents isospin breaking corrections in relating $K^+ \rightarrow \pi^+ \nu \bar{\nu}$ to the well-measured leading decay $K^+ \rightarrow \pi^0 e^+ \nu$ [13]. In obtaining the numerical value in (10), we used [14]

$$\sin^2 \Theta_W = 0.231, \quad \alpha = \frac{1}{127.9}, \quad \mathcal{B}(K^+ \rightarrow \pi^0 e^+ \nu) = (4.87 \pm 0.06) \times 10^{-2}. \quad (11)$$

Employing the improved Wolfenstein decomposition of the CKM matrix [15], expression (9) describes in the $\bar{\rho} - \bar{\eta}$ plane an ellipse with a small eccentricity, namely

$$(\sigma \bar{\eta})^2 + (\bar{\rho} - \bar{\rho}_0)^2 = \frac{\sigma \mathcal{B}(K^+ \rightarrow \pi^+ \nu \bar{\nu})}{\bar{\kappa}_+ |V_{cb}|^4 X^2(x_t)}, \quad (12)$$

where

$$\bar{\rho}_0 \equiv 1 + \frac{\lambda^4 P_c(X)}{|V_{cb}|^2 X(x_t)}, \quad \sigma \equiv \left(1 - \frac{\lambda^2}{2} \right)^{-2}, \quad \bar{\kappa}_+ \equiv \frac{\kappa_+}{\lambda^8} = (7.64 \pm 0.09) \times 10^{-6}. \quad (13)$$

Using (9) and varying m_t , $|V_{cb}|$, $P_c(X)$ and $|V_{td}|$, which is constrained by $|V_{ub}/V_{cb}|$ and the $B^0 - \bar{B}^0$ mixing in the $\bar{\rho} - \bar{\eta}$ plane, the branching ratio of $K^+ \rightarrow \pi^+ \nu \bar{\nu}$ is predicted to be

$$\mathcal{B}(K^+ \rightarrow \pi^+ \nu \bar{\nu}) = (0.78 \pm 0.12) \times 10^{-10} \quad (14)$$

within the SM. Here, the parameters used are summarized in Table 1. It should be noted that, for an uncertainty of 15% in (14), the theoretical uncertainty is $\sim 7\%$ at present, mainly due to the charm quark contribution.

Theoretically, one of the cleanest ways to extract the $|V_{td}|$ is regarded to be from a precise measurement of $\mathcal{B}(K^+ \rightarrow \pi^+ \nu \bar{\nu})$. This is due to the following reasons:

- Long-distance contributions to the branching ratio are negligible (at most 10^{-13}) [16].
- The uncertainty from the hadronic matrix element has been removed by using $\mathcal{B}(K^+ \rightarrow \pi^0 e^+ \nu)$.
- The remaining theoretical uncertainties (7%) are relatively small and reliable as compared with the errors in other K and B decays.

The theoretical uncertainty will be reduced if we can have a better knowledge about the QCD corrections to the charm contribution at the next-to-next-leading-order (NNLO) level. A precise measurement of $\Delta M_{B_d}/\Delta M_{B_s}$ in $B^0 - \bar{B}^0$ mixing would also narrow down the SM prediction, once $B_s^0 - \bar{B}_s^0$ mixing has been observed [17]. A precise measurement of the $K^+ \rightarrow \pi^+ \nu \bar{\nu}$ branching ratio is therefore a stringent test of the SM and also a probe for new physics.

1.2 History of $K^+ \rightarrow \pi^+ \nu \bar{\nu}$ Experiments

Searches for this process which began over 35 years ago all have used stopped- K^+ beams. It was believed at the time of the first of these that the branching ratio might be as high as a few $\times 10^{-5}$ [25]. It was recognized that even at this level, a poor signature process such as $K^+ \rightarrow \pi^+ \nu \bar{\nu}$ would need effective particle identification, precise kinematic measurement and the ability to veto extra charged and neutral tracks to discriminate it from common decay modes such as $K^+ \rightarrow \mu^+ \nu$ and $K^+ \rightarrow \pi^+ \pi^0$. The earliest published result was from a heavy liquid bubble chamber experiment [26] at the Argonne Zero Gradient Synchrotron, in which a 90% CL upper limit $B(K^+ \rightarrow \pi^+ \nu \bar{\nu}) < 10^{-4}$ was obtained. In this paper it was recognized that $K^+ \rightarrow \pi^+ \pi^0$ decay in flight and hadronic π^+ interaction in the detector were dangerous sources of potential background.

The final analysis of the Argonne experiment improved the limit to 5.7×10^{-5} [27], but before it appeared in print, a subsequent counter/spark-chamber experiment at the Berkeley Bevatron improved the limit to 1.4×10^{-6} [28]. However this experiment was sensitive to only the most energetic of π^+ , whereas the bubble chamber experiment covered a wide kinematic range. In addition to the background from common K^+ decay modes, this experiment considered possible background from K^+ charge exchange in the stopping target followed by $K_L \rightarrow \pi^+ e^- \nu$, and from beam π^+ which scatter into the detector. The Chicago-Berkeley group continued their program with a setup sensitive to π^+ in the kinetic energy range 60-105 MeV, *i.e.* below that of the potential background process $K^+ \rightarrow \pi^+ \pi^0$ rather than above it. This required reconfiguring their photon veto system so that it became nearly hermetic. Combining results from the two configurations, the branching ratio upper limit was improved slightly to 5.6×10^{-7} [29].

About a decade later, an experiment at the KEK Proton Synchrotron improved the limit to 1.4×10^{-7} [30]. This experiment also was sensitive only to the π^+ with momenta greater than that from $K^+ \rightarrow \pi^+ \pi^0$ (“ $pnn1$ ” region) and its setup resembled that of Ref. [28].

The BNL series of experiments was initiated in the early 1980's. It was based on a large-acceptance solenoidal spectrometer with a hermetic photon veto situated at the end

of a highly pure, very intense stopped- K^+ beam[32] from the Brookhaven Alternating Gradient Synchrotron (AGS). The first phase of BNL-E787 ran in 1988-91 and achieved a 90% CL upper limit on the branching ratio of 2.4×10^{-9} [33], using data from the $pnn1$ region. A separate limit of 1.7×10^{-8} [31] was extracted from the kinematic region in which the π^+ is softer than that of the π^+ from $K^+ \rightarrow \pi^+\pi^0$ (“ $pnn2$ ” region). This program also completed the identification of backgrounds needed to reach the 10^{-10} level of sensitivity and developed methods to reliably measure them.

A major upgrade of both the beamline and the detector was undertaken between 1992 and 1994. The search for $K^+ \rightarrow \pi^+\nu\bar{\nu}$ resumed in 1995 and continued through 1998. The limit on the branching ratio from the $pnn2$ region was improved by an order of magnitude to 2.2×10^{-9} at 90% CL but the major output of this series of runs was the observation of two clean $K^+ \rightarrow \pi^+\nu\bar{\nu}$ events[24] in the $pnn1$ region and a measurement of the branching ratio $B(K^+ \rightarrow \pi^+\nu\bar{\nu}) = (1.57^{+1.75}_{-0.82}) \times 10^{-10}$. The result from the first year’s run[23] (in which an event was observed), $B(K^+ \rightarrow \pi^+\nu\bar{\nu}) = 4.2^{+9.7}_{-3.5} \times 10^{-10}$, was even higher with respect to the SM prediction of the time $((0.82 \pm 0.32) \times 10^{-10}$ [10]) and it stimulated a 1999 proposal[34] to continue the program with an upgraded detector, using the entire proton flux of the AGS.

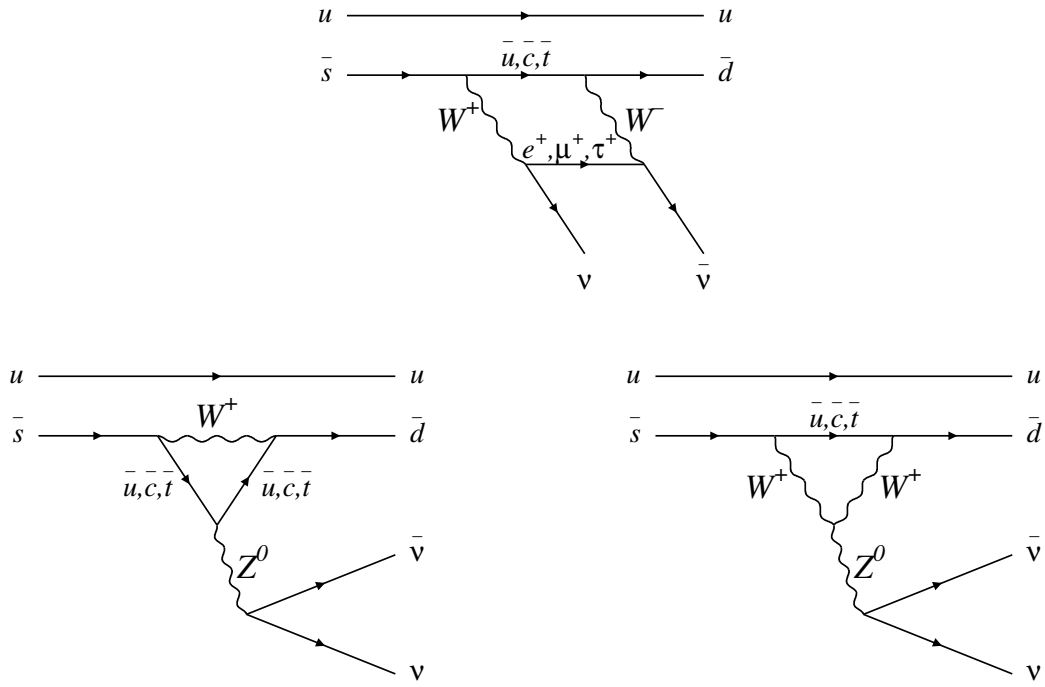


Figure 3: Second-order weak processes that contribute to the $K^+ \rightarrow \pi^+ \nu \bar{\nu}$ branching ratio: the "Box" diagram (upper) and two "Z-penguin" diagrams (bottom).

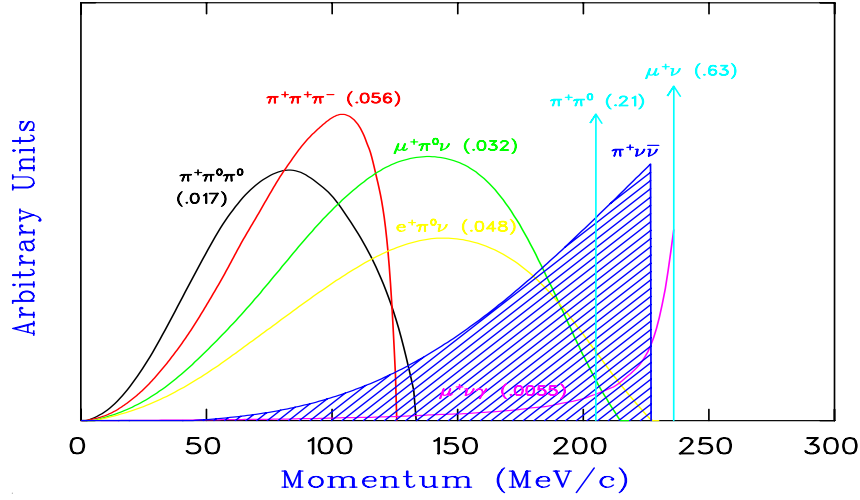


Figure 4: Momentum spectra (in MeV/c) of charged particles from K^+ decays in the rest frame. The values in the parentheses represent the branching ratios for their decay modes. The hatched spectrum shows the π^+ momentum in the $K^+ \rightarrow \pi^+ \nu \bar{\nu}$ decay assuming the $V - A$ interaction.

2 Experimental Method

2.1 Overview

The advantage of a K^+ -stop experiment is that momenta of charged particles can be used as a distinguish feature in all the K^+ decay modes as shown in Figure 4. The experimental signature of the $K^+ \rightarrow \pi^+ \nu \bar{\nu}$ decay is a single π^+ track plus no other particle from a K^+ decay. Theoretically, the maximum π^+ momentum is 227 MeV/c. The $K^+ \rightarrow \mu^+ \nu_\mu$ ($K_{\mu 2}$), $K^+ \rightarrow \mu^+ \nu_\mu \gamma$ ($K_{\mu 2 \gamma}$) $K^+ \rightarrow \pi^+ \pi^0$ ($K_{\pi 2}$) decays are mainly concerned when the search is only conducted above the $K_{\pi 2}$ peaks. Signal imitation comes from either a μ^+ from the $K_{\mu 2}$ being misidentified as π^+ and the gamma from $K_{\mu 2 \gamma}$ being lost as well, or the photons from π^0 decay being missed together with the π^+ momentum, range and energy being shifted downward due to the experimental resolution effect or the occurrence of scattering along the π^+ trajectory in the $K_{\pi 2}$.

In addition to the background from the K^+ decays, there are also backgrounds from the beam contamination, including the single π^+ beam being mis-identified as a K^+ beam, the decay-in-flight K^+ beam, the double beam with an accompanying K^+ or a π^+ beam and the interaction of $K^+ + n \rightarrow p + K_L^0$, $K_L^0 \rightarrow \pi^+ l^- \bar{\nu}_l$.

This experiment used the same technique as all the previous $K^+ \rightarrow \pi^+ \nu \bar{\nu}$ experiments: a low momentum K^+ beam stopped in the detector. Measurement of the $K^+ \rightarrow \pi^+ \nu \bar{\nu}$ decay involved an observation of the π^+ in the absence of other coincident activity. The π^+ was identified by its kinematic feature from the energy, momentum and range measurements, and by the observation of a $\pi^+ \rightarrow \mu^+ \rightarrow e^+$ decay sequence. Since the signal rate is expected to be about 10^{-10} level, to achieve this sensitivity the detector was designed to have a powerful π^+ identification to reject the $K_{\mu 2(\gamma)}$, a 4π solid angle plus full energy coverage photon veto to reject the $K_{\pi 2}$, and a perfect beam K^+ identification to

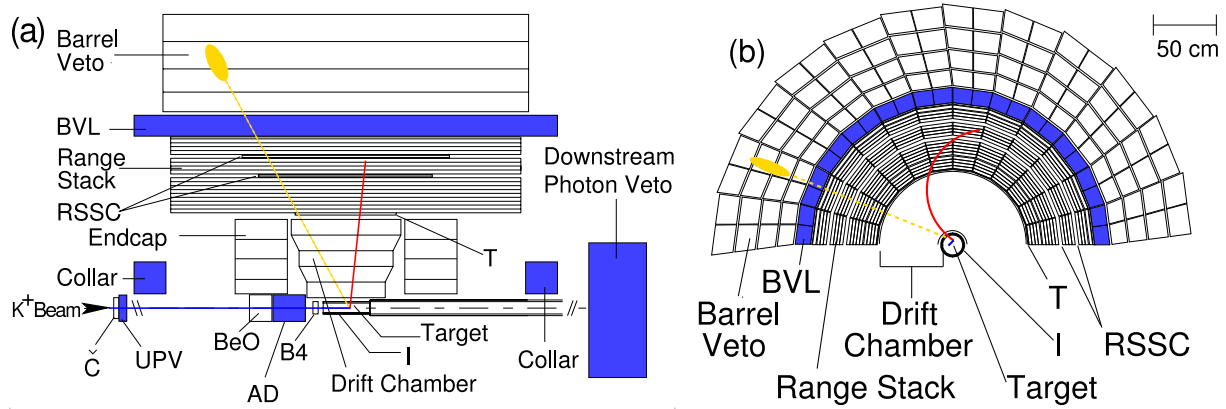


Figure 5: Schematic side (left) and end (right) views of the upper half of the E949 detector.

eliminate the beam backgrounds.

The E949 experiment (BNL-E949) was a successor to the E787 experiment (BNL-E787) that ran at the Alternating Gradient Synchrotron (AGS) at BNL from 1987–1999. The E787 detector has been described previously [32] as it existed during the period 1987–1991. The E787 detector was upgraded during 1992–1994, some of these upgrades have been described elsewhere [37, 39, 41, 42], while others will be described here. The E949 detector (see Figure 6) was upgraded over the period from 1999–2001 [34, 35]. Several improvements were made to the detector: additional and improved photon veto systems, improved tracking systems, improved trigger efficiency, and reduced DAQ dead time. E949 was designed to run at the same instantaneous rate as E787, and to achieve a factor of five improvement in average sensitivity by running with substantially more proton flux and a higher duty factor and reduced K^+ momentum. In practice the higher duty factor was not achieved in the engineering run in 2001 or the first physics run in 2002 due to a broken motor generator set at the AGS (the Siemens was removed from operation on 8/3/01 and the backup Westinghouse MG set was used during the rest of 2001 and 2002) and E949 ran at about twice the beam rate of E787. The experiment was proposed and approved by the U.S. Department of Energy’s Office of High Energy Physics to run for 60 weeks. After the first 12 weeks of running in 2002 no further funds were provided to complete the experiment. In this section, we will describe the detector and beam.

2.2 The Accelerator and K^+ Beam Line

The K^+ beam was produced by a high-intensity proton beam from the AGS at BNL: the entire AGS beam of 65×10^{12} (Tp) was delivered to the E949 K^+ production target (C-target). Protons were accelerated to a momentum of 21.5 GeV/ c . Prior to 2001 the AGS typically ran at 24 GeV/ c , but at this higher momentum the longest spill achievable with the Westinghouse MG set was 0.5 sec. Combined with the longer cycle time of the Westinghouse (3.2 sec between spills, as compared to 2.3 sec with the Siemens), the duty

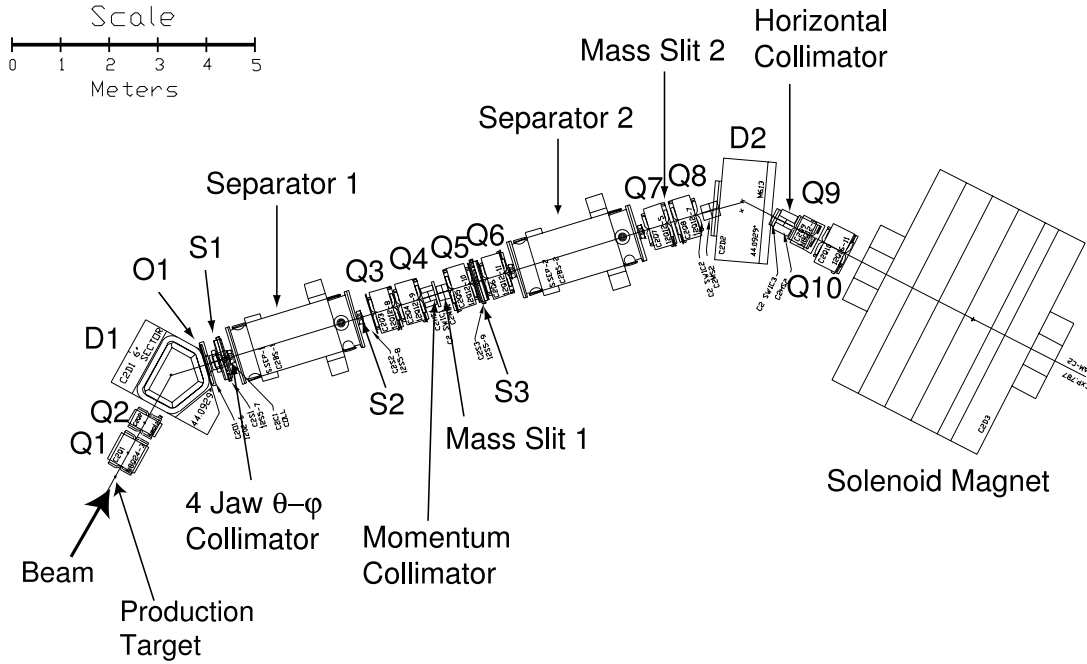


Figure 6: Low-energy separated beam line III at BNL.

factor at 24 GeV/ c was unacceptably low. By lowering the proton momentum to 21.5 GeV/ c , the spill length was increased to a maximum of 2.2 sec, resulting in a duty factor of 2.2sec/5.4sec. At this lower proton momentum the production of 710 MeV/ c K^+ s was reduced by 10%. The K^+ production target is made of 2/3 of an interaction length of platinum (6 cm along the beam direction), and is located on a water-cooled copper base. At the typical AGS running condition 65 Tp on the production target per 2.2 second spill at 21.5 GeV/ c the target temperature was measured to be $\sim 700^\circ\text{C}$.

The Low Energy Separated Beam [36] (LESB III), shown in Figure 6, collects and focuses K^+ s emitted at 0° (along with 500 π^+ s and 500 protons at the target for every K^+), and is momentum-selected by dipole magnet D1 (see Figure 6). Two electro-magneto-static separators (Separators 1 and 2 in Figure 6) sweep π^+ s and protons out of the beam. The resulting beam is further selected by a second dipole magnet (D2 in Figure 6). LESB III contains a number of focusing quadrupole (Q1-10), sextupole (S1-3), and octupole (O1) magnets and collimating slits, and has a total length of 19.6 m from the production target to the E949 target with an angular acceptance of 12 msr and a momentum acceptance of 4.5% FWHM. K^+ s with a mean 710 MeV/ c were transported to E949. During most of the 2002 running period the first separator voltage was lowered from the standard voltage of 600kV to $\sim 250\text{kV}$ due to high voltage discharges. This reduced operating voltage necessitated a retuning of the beam line to remove π^+ s with a consequent loss of K^+ s. Under these conditions a $K^+ : \pi^+$ ratio in the beam of 3:1 was achieved with a 40% loss in K^+ flux (typically E787 ran with 4:1). Proton contamination was negligible due to a large deflection of protons by the separators. At the typical AGS running condition of 65 Tp on the production target per spill, 1.3×10^7 K^+ s were transported through the beam line.

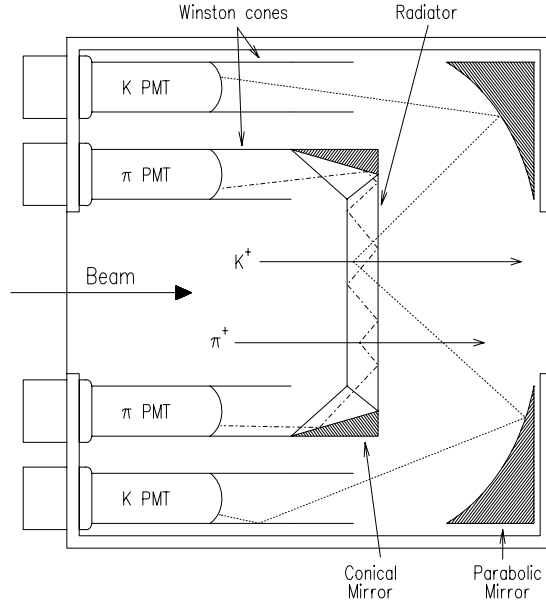


Figure 7: Side view of the Čerenkov counter.

2.3 Beam Counters

The beam instrumentation had three roles: K^+ identification, K^+ momentum degradation, and detection of any extra particles coincident with K^+ of interest or its decay products. The beam instrumentation from upstream to downstream consisted of a large scintillator counter (B0), a Čerenkov counter, a photon detector (UPV), two beam wire chambers, a degrader and a beam hodoscope.

The B0 counter was located just downstream of the last quadrupole magnet (Q10) and counted all charged particles in the beam. The Čerenkov counter (see Figure 7) located just downstream of the B0 counter identified particles as K^+ s or π^+ s. The refractive index (n) of the 25 mm thick acrylic radiator is 1.49, providing a threshold for Čerenkov radiation of $\beta_{\check{C}} = 1/n = 0.671$ and a threshold for total internal reflection of $\beta_{ref} = \sqrt{1/(n^2 - 1)} = 0.905$. K^+ s and π^+ s with a momentum of 710 MeV/c have $\beta_{K^+} = 0.82$ and $\beta_{\pi^+} = 0.98$, respectively; the Čerenkov light from K^+ s (π^+ s) was transmitted (reflected) at the downstream surface of the Čerenkov radiator. The K^+ light exited the radiator and was reflected by a parabolic mirror to the outer ring of 14 EMI9954 photomultiplier (PMT) tubes (K^+ Čerenkov counter, C_K), while that from a π^+ was internally reflected within the radiator and directed to the inner ring of 14 PMT's (π^+ Čerenkov counter, C_π). The PMT signals were split, with 90% fed to time-to-digital converters (TDC's) via discriminators and 10% fed into a $\times 10$ amplifier and then to 500 MHz transient digitizers based on gallium-arsenide (GaAs) charge-coupled devices (CCD's) [37]. The pulse-height information in every 2 ns interval was recorded in CCD's to reproduce the time development of the pulses and to detect two particles close in time to each other. In addition the total number of photoelectrons in all PMT's provided additional particle identification. A charged particle passing through the Čerenkov counter fired many PMT's in the K^+ or π^+ Čerenkov counter. At the trigger level the number of Čerenkov discriminator channels firing (typically 6) was used to identify K^+ s and π^+ s.

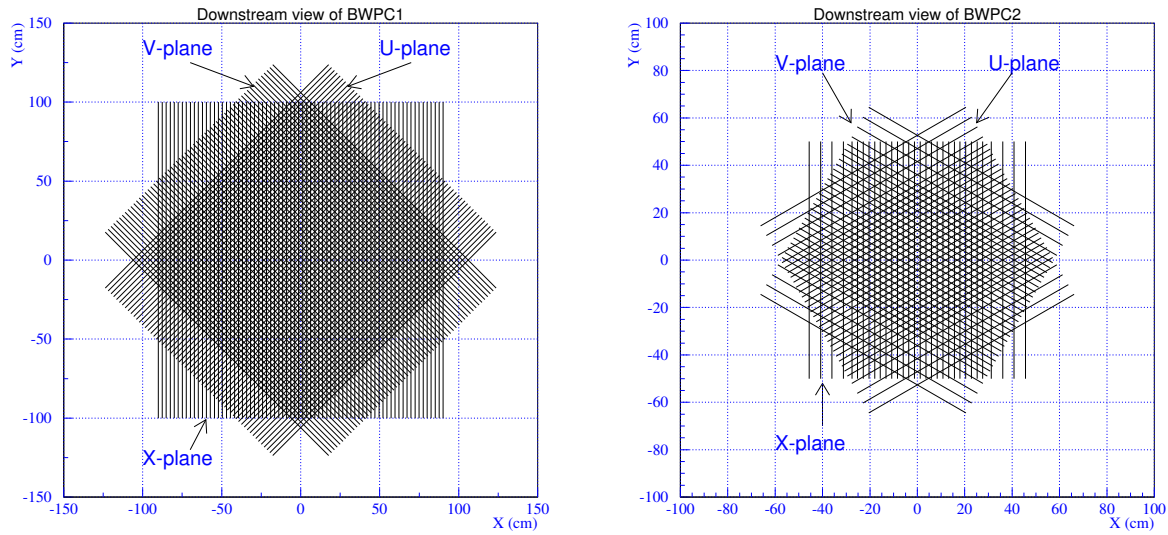


Figure 8: Cross-sectional views of the beam wire chambers (BWPC's): the first BWPC (left) and the second BWPC (right).

Offline analysis treated all PMT hits coincident with each other as a cluster. It is possible that extra particles may pass through the Čerenkov counter, causing additional clusters. A K^+ was therefore identified by requiring that the K^+ Čerenkov counter had only one hit cluster. The average time of the hits in each cluster was compared to the K^+ decay time; any event with an extra particle coincident with the K^+ decay time was rejected, since an extra particle, not the decay of the initial K^+ , might be origin of the charged track that entered the fiducial region of the detector. Since two incoming particles close in time can fire the same PMT's, and these pileup signal may not be identified by the TDC's. The pulse shapes recorded in the CCD's were therefore used to discriminate such pileup signals.

Mounted to the downstream face of the Čerenkov counter was a photon detector, the upstream photon veto (UPV). The UPV was 3.1 radiation length thick, with an outer dimension of 284 mm \times 284 mm and an inner hole for the beam of 175 mm (horizontal) \times 40 mm (vertical). The 12 layers of 2 mm BC404 plastic scintillator were each read out by 21 WLS fibers to one of two Hamamatsu R1924 PMT's. The UPV signals were split three ways to ADC's, TDC's and CCD's.

The two beam wire chambers (BWPC's) were located downstream of the Čerenkov counter and UPV, and monitored the beam profile and identified multiple incoming particles. Cross-sectional views of the BWPC's are shown in Figure 8. The first chamber (BWPC1) contained three planes of sense wires: U, V and X. The direction of the sense wires was vertical (X-plane) and $\pm 45^\circ$ to the vertical (U- and V-planes). The sense wires were 0.012 mm diameter gold-plated tungsten. The X-, U- and V-planes had 72, 60 and 60 readout channels respectively, with 2.54 mm wire spacing. The spacial resolution was 1.5 mm and the active area was 178 mm (horizontal) by 50.8 mm (vertical). The cathode foils were 0.025-mm thick aluminized mylar coated with carbon. The anode-cathode

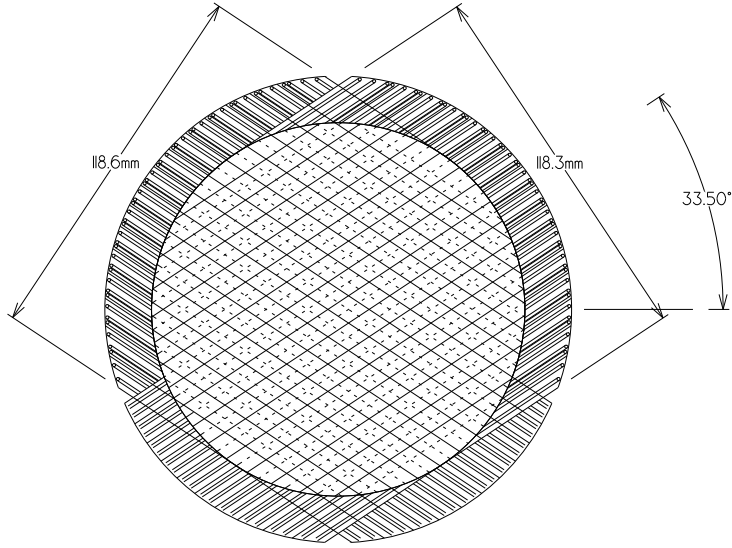


Figure 9: End view of the B4 hodoscope. Patterns of scintillator fingers on the downstream and upstream surfaces are shown in solid and dashed lines separately.

distance was 3.175 mm, and the total thickness of BWPC1 was approximately 56 mm. The second chamber (BWPC2) was located 900 mm downstream of BWPC1 and contained three planes (U, V and X). The direction of the sense wires was vertical (X-plane) and $\pm 60^\circ$ to the vertical (U- and V-planes). Each plane had 24 readout channels with a 2.40-mm wire spacing in the central region (57.6 mm) and 8 channels with a 4.80-mm wire-spacing in the peripheral region (19.2 mm on each end). The cathode foils were 0.008-mm single-side aluminized mylar coated with carbon. The anode-cathode distance was 1.5875 mm. Both chambers were filled with a mixture of CF₄ (80%) and Isobutane (20%).

Downstream of the BWPC's, a degrader slowed the K^+ s to come to rest in the center of the target. The upstream section of the degrader was inactive with 111.1 mm of beryllium oxide (BeO) and 4.76 mm of Lucite. The total thickness was tuned to stop K^+ s with a momentum of 710 MeV/ c in the center of the target. BeO, with high density and low atomic number, minimized the multiple scattering. The downstream active degrader (AD) consisted of 40 layers of 2 mm thick scintillator disks (139 mm diameter) alternating with 2.2-mm thick copper disks (136 mm diameter). The AD was divided into 12 azimuthal segments, and the scintillation light in each segment was sent to a single Hamamatsu R1924 PMT through 14 Bicon BCF99-29-AA-MC wave length shifting (WLS) fibers. The PMT outputs were fed to TDC's and CCD's. The signals from 4 PMT's were multiplexed and fed to a single analog-to-digital converter (ADC). The AD identified the beam particles and detected activity coincident with K^+ decays.

Between the degrader and the target was a beam hodoscope (B4 hodoscope) that detected the position of the incoming particle, giving a 3-dimensional space-point to match to the target and identified the particle as a K^+ or π^+ by measuring its energy deposit. An end view of the B4 hodoscope is shown in Figure 9. The B4 hodoscope consisted of two planes, U and V, with a 119 mm diameter oriented at an 56.50° angle to the vertical. Each plane had 12 scintillator fingers with a 7.2 mm pitch. The cross section of each finger

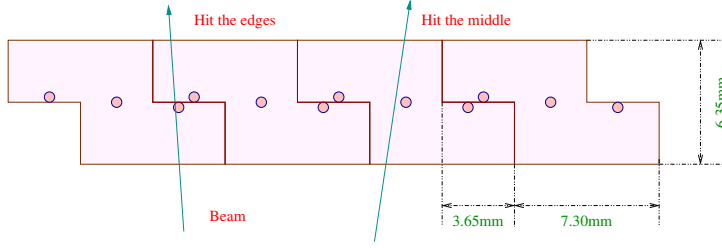


Figure 10: Schematic cross section of the B4 hodoscope. Arrows indicate difference situations of beam particles passing through the B4 hodoscope.

had a ‘Z-shape’, as shown in Figure 10, with a 6.35-mm thick middle part and 3.175-mm thick edges. This shape reduced inactive regions and improved the spatial resolution. Three Bicron BCF99-29-AA-MC WLS fibers were embedded in each finger and fed to a single Hamamatsu H3165-10 PMT that was read out by TDC’s, ADC’s and CCD’s. A double-pulse fit was performed on signals recorded by the CCD’s to find possible pileup. The time development of the output signals were fit with both single- and double-pulse assumptions. If the fitted pulse was more likely to be a double pulse and the time of the second pulse was coincident with the K^+ decay time, the event was rejected. At the same position as the B4 hodoscope, but at larger radius was another scintillator counter, the ring veto (RV). The RV was designed to veto particles that passed through the B4 hodoscope fibers. The RV was composed of two 180° arcs of 3.27 mm thick scintillator with an inner diameter varying from 118.5 mm to 120 mm and an outer diameter of 145.5 mm. The two RV elements were readout to H3165-10 PMT’s and the signals were split three ways to ADC’s, TDC’s and CCD’s.

The K^+ s underwent decay-in-flight, nuclear interactions in the degrader or scattering out of beam that didn’t reach the target. Approximately 27% of the incident K^+ s penetrated far enough into the target to satisfy the online target criteria of ~ 20 MeV. Typically 3.5×10^6 K^+ s entered the target per beam spill.

2.4 Target

The K^+ s, slowed down by the degraders, entered the scintillating fiber target located in the center of the spectrometer. And then they lost energy, came to rest, and decayed in the target. The target consisted of 413 5-mm square and 3.1-m long plastic scintillating fibers that were bundled to form a 12-cm diameter cylinder. A number of smaller fibers (called “edge fibers”) were filled in the gaps near the outer edge of the target, in order to have a uniform thickness of the target material. End and side views of the target are shown in Figure 11. Each of the 5.0-mm fibers was connected to a PMT, whereas the edge fibers were grouped into 12 and each group of the edge fibers was connected to a single PMT. The PMTs were read out by ADCs, TDCs and CCDs. The K^+ s, whose velocities were small, typically lost a large amount of energy (few tens MeV) in each fiber, while π^+ s from K^+ decays lost about 1 MeV per fiber, since they traveled nearly perpendicularly and lost energy as minimum ionizing particles (MIPs). Pattern recognition was performed to find fibers that belonged to a K^+ ’s path or a π^+ ’s path. The CCD pulse information was

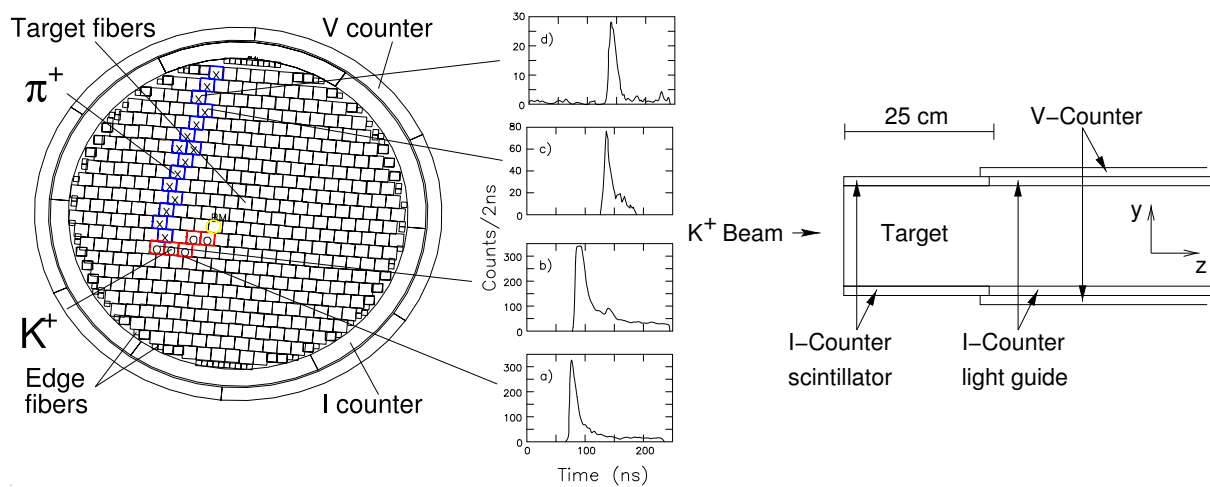


Figure 11: End (left) and side (right) views of the target. The CCD pulse-shape information is used to find K^+ and π^+ clusters, as shown in the left figure; the lower two plots, labeled by "a)" and "b)", are CCD pulses for a K^+ , and the upper two plots, labeled by "c)" and "d)", are those for a π^+ . Two layers of 6 plastic scintillators, I-Counter (IC) and V-Counter (VC), surround the target.

used to find clusters for K^+ s (K^+ fibers) and π^+ s (π^+ fibers). A double-pulse fitting was performed to find the fiber where a $K^+ \rightarrow \pi^+$ decay vertex was located and to estimate the energy loss and range of the π^+ hiding in the K^+ fiber.

The fiducial region of the target was defined by two layers of 6 plastic-scintillating counters that surrounded the target (see Figure 11). The inner scintillators, called I-Counter (IC), tagged charged decay products before they entered the drift chamber, and provide a trigger signal to the data acquisition system. The IC was 6.4-mm thick at an inner radius of 6.0 cm, and extended 24 cm downstream from the upstream face of the target. Each scintillator was instrumented with a PMT, and was read out by an ADC, a TDC and a 500 MHz transient digitizer based on flash ADC (TD) [38]. The outer scintillators, called the V-Counter (VC), overlapped the downstream edge of the IC by 6 mm, and served to detect particles that decayed downstream of the fiducial region of the target. The VC was 5-mm thick and 1.96-m long, and was staggered with respect to the IC. Each scintillator was instrumented with a PMT, which was read out by an ADC and a TDC.

2.5 Tracking chamber

The tracking chamber is also called "Ultra Thin Chamber" (UTC), which was located just outside of the IC. The whole spectrometer was in a 1 Tesla magnetic field. Positively charged particles were bent clockwise in the view from downstream. The primary functions of the UTC was to measure the momenta of charged particles and to provide matching of the tracks between the target and the Range Stack (RS) as well.

The UTC had a length of 51 cm, and an inner and an outer radii of 7.85 cm and 43.31 cm, respectively. The 12 layers of drift cells were grouped into 3 super layers. The inner, middle and outer super layers all had 4 sub layers each, consisting of 48, 96 cells,

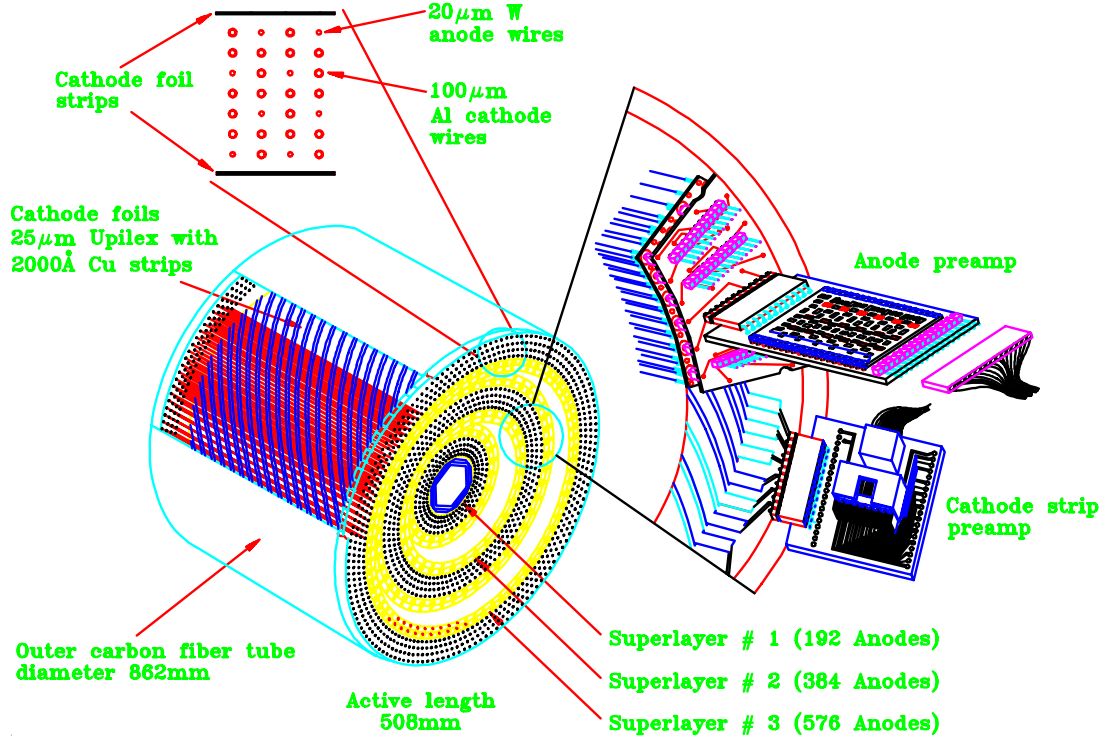


Figure 12: Schematic view of the Ultra Thin Chamber.

144 cells in them, respectively as shown in Figure 12. Each cell was composed of 9 wires strung axially. A single anode wire, made of gold-coated tungsten with 20- μm diameter, was surrounded in a square by 8 cathode wires made of gold-coated aluminum with 100- μm diameter. Adjacent cells shared the cathode wires at the boundaries. The cells in each layer were staggered by one-half cell with respect to the neighboring layers in order to resolve the left-right ambiguity in track fitting. The super layers were filled with a mixture of argon (49.6%), ethane (49.6%) and ethanol (0.8%) gases. The cathode wires were all grounded, while the anode wires were maintained at 2 kV to achieve a 8×10^4 of gain and a 5 cm/ μs of drift velocity. Each anode wire was instrumented with an ADC and a TDC. The drift time to the anode wires was used to determine the (x, y) positions for a charged track.

The inner and outer radii of each super layer had helical arrays of cathode strips with a pitch angle of 45° . The strips with a 7 mm of width each and 1 mm of gap between them were made of 1200-Å thick copper coated with 300-Å thick nickel, and mounted on a 25- μm thick Kapton foil. The cathode foils had 48, 72, 108, 144, 180, and 216 strips from the inner to the outer layers, respectively. Each cathode strip was instrumented with an ADC and a TDC. The z position of a charged track was determined by the charge-weighted mean of the cluster of hit strips. The resolution was measured to be about 1 mm.

There were 2 inactive regions filled with nitrogen gas between the 3 super layers. Differential pressures in the 5 gas volumes supported the cathode foils (excluding the innermost and outermost foils, which were held in place by support tubes). The total mass in the active region of UTC (excluding the inner and outer support tubes and

innermost and outermost foils) amounted to 2×10^{-3} radiation lengths.

The momentum resolutions ($\Delta P/P$) for the two body decays $K_{\pi 2}$ and $K_{\mu 2}$ are measured to be 1.1% and 1.3%, respectively. Detail information can be seen elsewhere [39].

2.6 Range Stack

Range Stack (RS) consisted of both the scintillator counters and the embedded straw chambers, providing energy and range measurement of the charged particles, information of the $\pi^+ \rightarrow \mu^+ \rightarrow e^+$ decay sequence and measurement of the photon activity as well.

2.6.1 Scintillator Counters

The RS scintillator counters were used to measure the energy and range of charged particles and to observe the $\pi^+ \rightarrow \mu^+ \rightarrow e^+$ decay sequence. The RS was located just outside the UTC at an inner radius of 45.08 cm and an outer radius of 84.67 cm. It consisted of 19 layers of plastic scintillators, azimuthally segmented into 24 sectors as shown in Figure 13. Four contiguous sectors (i.e., sectors 1-4, 5-8, etc.) were grouped into “hexants” for read out and triggering purposes. The scintillators of layers 2-18 had a thickness of 1.905 cm and a length of 182 cm. The scintillators of layer 19 had a thickness of 1 cm; this layer was mainly used to veto charged particles with range longer than that expected for the π^+ from $K^+ \rightarrow \pi^+ \nu \bar{\nu}$. The scintillation light in the layer 2-19 counters was led by Lucite light guides to PMTs at both the upstream and downstream ends. The innermost counters were the trigger-counters (T-counters) and had a thickness of 6.35 mm and a length of 52 cm. The T-counters are thinner than layers 2-19 to suppress triggers due to photon conversions. Seventeen 1mm diameter WLS fibers (Bicron multi-clad BCF-92) with a pitch of 6.9mm were embedded in each scintillator were grouped to illuminate a single PMT for each end. The T-Counters also defined the fiducial region as 2π sr solid angle, nearly the same as the solid-angle acceptance of UTC.

The signal from each PMT of the RS scintillators was passively split 1:2:2 for ADC:TDC:TD read out. Signals from 4 PMTs at the same end, same hexant and same layer were multiplexed and read out by a single Transient Digitizer (TD) [38]. The TDs record the charge in 2 ns intervals (500 MHz sampling) in a $(-0.5, +2.0)\mu\text{s}$ interval about the trigger time with a resolution of 8bits (0-255 counts). The 500 MHz sampling provides sufficient pulse shape information to separate the pulses from different energy deposits as close as 5 ns apart, and enabling the detection of the $\pi^+ \rightarrow \mu^+$ decay for particle identification as described in Section 3.5.3. The gate width of the TDs was narrower than that of the TDCs in order to reduce the data size. TD signals were demultiplexed offline using TDC information. The ADCs (LeCroy 4300) record charge in a $(-20, +85)$ ns interval about the trigger time, and the TDCs (LeCroy 3377) recorded up to 16 hits in a $(-0.5, +10.0)\mu\text{s}$ interval about the trigger time. The large time interval after the trigger for the TDCs allows detection of the $\mu^+ \rightarrow e^+$ decay. The time of a hit in the RS counters was obtained from the average of the upstream and downstream TDC times, and the z position of the hit was obtained from the time difference.

The π^+ s from $K^+ \rightarrow \pi^+ \nu \bar{\nu}$ decay had a maximum momentum of 227 MeV/ c and a maximum range in plastic scintillator of ~ 40 cm, which is shorter than 45 cm for the

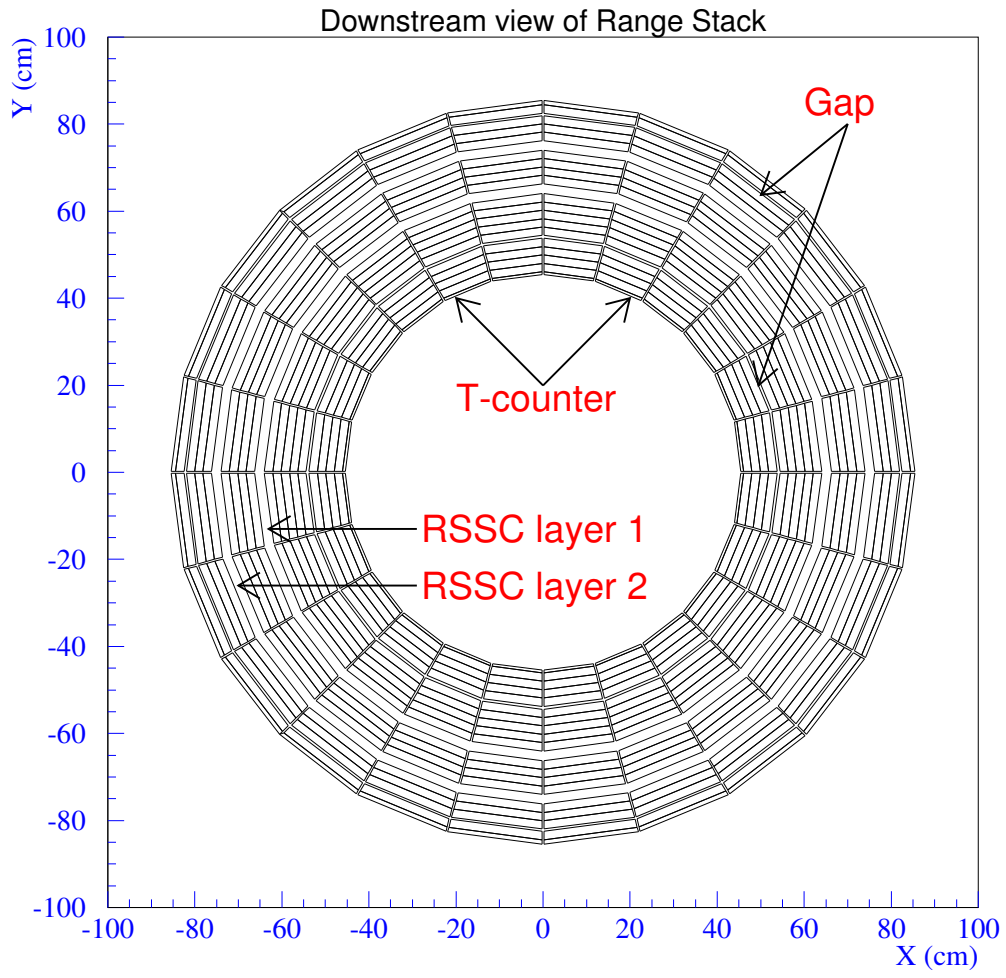


Figure 13: End view of the Range Stack. Two layers of the Range Stack Straw Chambers are located after layers 10 and 14.

total radical thickness of the RS and target. All of the π^+ s, bent in a 1 Tesla magnetic field, lost their entire kinetic energy and came to rest in the RS. In comparison, the μ^+ s from the $K_{\mu 2}$ decay ($Br(K^+ \rightarrow \mu^+ \nu_\mu) = 63.4\%$ [6]) at rest have a momentum of 236 MeV/c and a range of 54.3 cm in plastic scintillator, and can thus penetrate the RS with a stop. It is noted that lower momentum μ^+ s from the $K_{\mu 2 \gamma}$ and $K_{\mu 3}$ decays ($Br(K^+ \rightarrow \mu^+ \nu_\mu \gamma) = 0.55\%$ and $Br(K^+ \rightarrow \mu^+ \pi^0 \nu_\mu) = 3.27\%$ [6]) as well as the μ^+ s from π^+ decay in flight could come to rest in the RS. In such a situation, one must rely on the observation of the $\pi^+ \rightarrow \mu^+ \rightarrow e^+$ decay sequence in the TDs and TDCs of the counter where the π^+ stops (called the stopping counter), to get a powerful separation between μ^+ and π^+ .

2.6.2 Straw chambers

The range stack straw chambers (RSSCs) were located after layers 10 and 14 in the RS. The inner (outer) RSSC consisted of two staggered layers of 24 (28) straws per sector with a length 97.8 (113.0) cm. The straw tubes had a radius of 3.3 mm and operate with 67% argon and 33% isobutane mixture bubbled through water in self-quenching streamer mode. Wires in neighboring chambers were connected at the upstream end and read-out from the downstream end. The time difference as well as the relative pulse height ratio provided a z measurement. The resolution was measured to be about 1 cm. The position of the hit straws also provided the azimuthal position information. All of which were used to aid in the determination of the trajectory and the range of a charged particle in the RS [40].

2.6.3 Resolutions of energy and range

Energy and range measurements of charged tracks, as well as the momentum measurement, are crucial to distinguish the π^+ s in the signal region from backgrounds due to the $K_{\pi 2}$ and $K_{\mu 2}$ decays, since both of them have monochromatic momenta of 205 and 236 MeV/c, respectively. The RS provided most of energy and range measurements for the charged tracks. Final results should also combine the measurements from the target and the correction for the UTC dead material as well. In this analysis, the energy and range resolutions were measured to be 2.8% and 2.9% for the fully contained $K_{\pi 2}$. For the $K_{\mu 2}$ decays, they were 2.9% and 3.1%.

2.7 Photon veto counters

The detection of any activities coincident with the charged track is crucial for suppressing the backgrounds for $K^+ \rightarrow \pi^+ \nu \bar{\nu}$. Photons from the $K_{\pi 2}$ and the other radiative decays were detected by the hermetic photon detectors as already shown in Figure 5. The photon detectors, surrounding the K^+ decay vertex in a 4π solid angle, were located in the barrel, upstream and downstream end caps, and near the beam line. The photon veto was performed by the Barrel Veto (BV), the Barrel Veto Liner (BVL), the upstream and downstream End Caps (ECs), the upstream and downstream Collar detectors (CO), the downstream Microcollar detector (MC), the Upstream Photon Veto (UPV), the Down-

stream Photon Veto (DPV), the Ring Veto (RV), as well as the target and the RS photon vetos.

The 1.9-meter-long BV was located in the outermost barrel region with an inner radius of 94.5 cm and an outer radius of 145.3 cm. Two thirds of the 4π sr solid angle was covered by 48 azimuthal sectors. Each sector consisted of four radial segments, in which there were 16, 18, 20, 21 layers of 1-mm thick lead and 5-mm thick plastic scintillator from the inner to the outer modules, respectively. The azimuthal boundaries of each sector were tilted so that no crack was left along the radial direction for the photons from the decay vertex. The BV measured 14.3 radiation lengths in total. Each end of every module was read out by a PMT and the signals were recorded by an ADC and a TDC. The photon energy left in the scintillators accounted for 30% of the total energy deposit in the BV. The time resolution of individual BV counter, which was measured to be 1.0 ns, was limited by the sampling time of the TDCs.

The BVL, a newly installed detector for the E949, was located just outside the RS and inside the BV. It measured 85.2 cm in inner radius and 93.5 cm in outer radius, and also had 48 azimuthal sectors. Each sector consisted of 12 layers of 1-mm thick lead and 5-mm thick plastic scintillators, all of which gave a total of 2.3 radiation lengths in thickness. The length of BVL was designed to be 2.2 m, which was longer than the BV in order to add more active material to the region where the radiation length is relatively shorter. Each end of a BVL module was read out by a PMT and the signals were recorded by an ADC and a TDC. Adjacent sectors in each end were grouped and read out by the TDs. The timing resolution of individual BVL counter was observed to be 0.5 ns, which was also limited by the TDC sampling time.

The EC[41] was located in the 1 Tesla magnetic field and had roughly one-third of the 4π sr photon coverage. Since the EC was exposed in a high counting-rate environment near the beam line, beam particles could cause many irrelevant hits so that the photons from a $K_{\pi 2}$ decay might be masked if this accidental hit arrived earlier (see Figure 14). The upstream EC detector consisted of 75 undoped Cesium Iodide (CsI) crystals segmented to the four rings (13, 14, 21 and 27 crystals from the inner to outer rings, respectively), and the downstream EC detector consisted of 68 crystals in the four rings (11, 13, 19 and 25 from inner to outer rings, respectively). A total of 143 crystals with a pentagonal cross-section were used in the EC as shown in Figure 15. Each crystal measured in 25 cm long (13.5 radiation lengths), and the whole EC detector was designed to minimize photon escape through its radial cracks. Fine-mesh PMTs [42], which maintained high gains in strong magnetic fields, were attached directly to the crystals to achieve efficient light collection (see Figure 15). Only the fast component of the CsI light output with a decay time of a few tens of nanosecond at a wavelength of 305 nm was selected by ultraviolet (UV) transmitting optical filters. The PMT signals were read out by ADCs, TDCs, and CCDs. The pulses recorded in the CCDs were analyzed by a pulse-finding algorithm, in order to separate two pulses close in time and reduce the possibility of accidental vetoes and the inefficiencies of photon detection.

The other photon detectors, including the CO, MC, UPV, DPV and RV, were located around the beam line to cover the region with small angles. These detectors were used to detect photons that were emitted along the beam line and escaped from the detection by the BV, BVL, EC and RS.

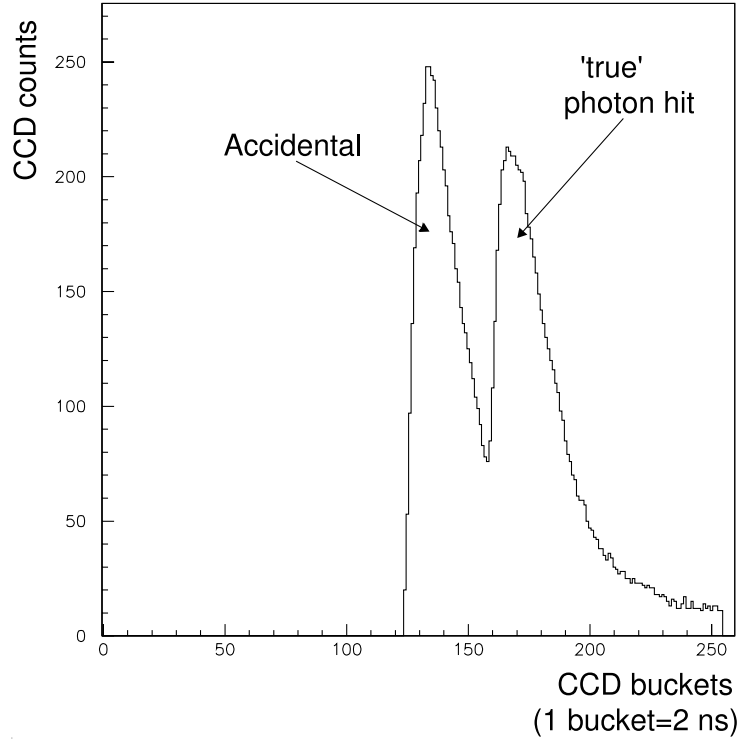


Figure 14: Pulses recorded in the End Cap CCD. The first pulse is due to an early accidental hit and the second pulse is due to the photon from the $K_{\pi 2}$ decays.

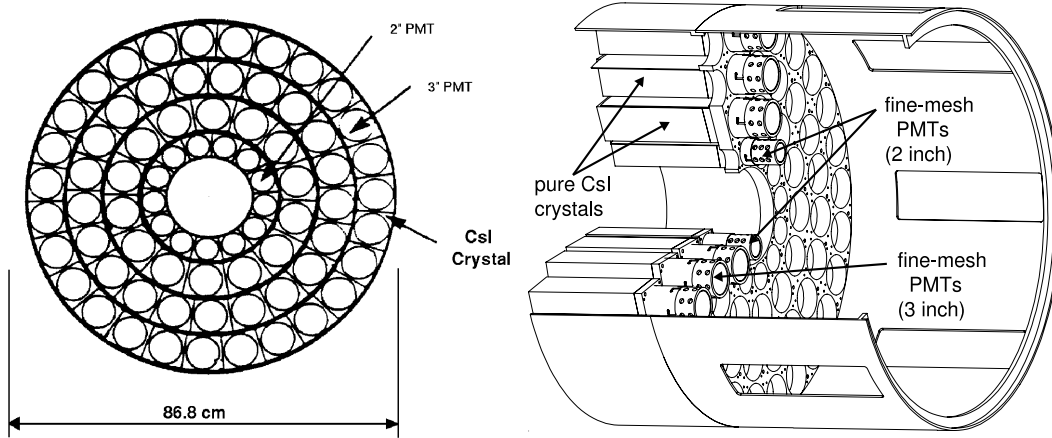


Figure 15: End view (left) and back view (right) of the End Cap.

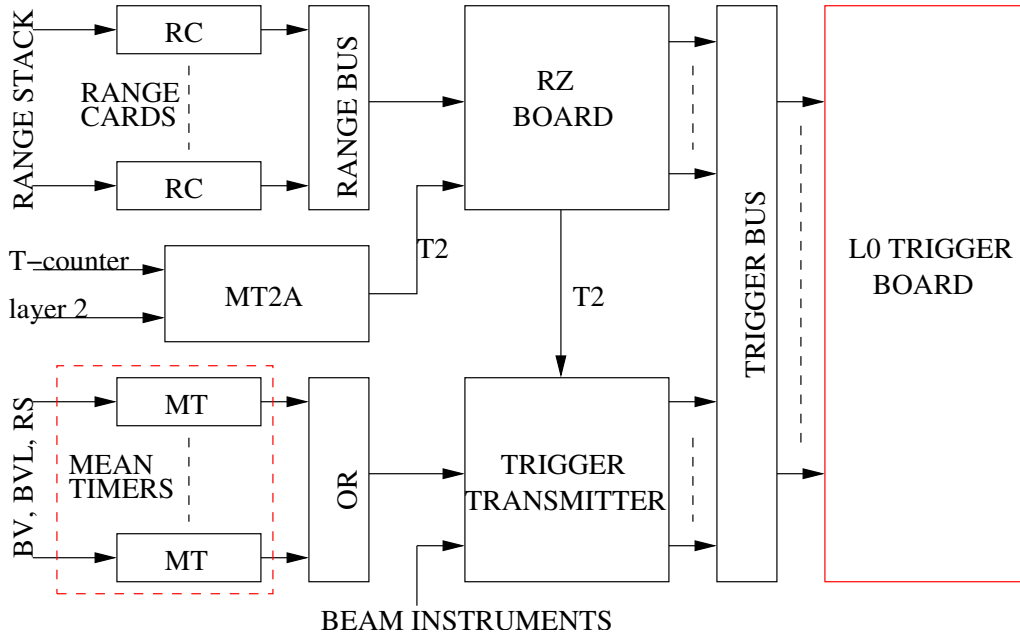


Figure 16: Block diagram of the L0 trigger system.

2.8 Trigger

Typically 3.5×10^6 K^+ s entered the E949 target every spill. The trigger selected $K^+ \rightarrow \pi^+ \nu \bar{\nu}$ events from the large number of K^+ decays and scattered beam particles with requirements on the range of the π^+ track, the presence of a $\pi^+ \rightarrow \mu^+ \nu_\mu$ decay, the absence of other activity at the time of the π^+ and the presence of a K^+ at an appropriately earlier time.

The trigger was composed of two stages: a fast level-0 trigger with a decision time of ~ 100 ns and a slower level-1.n trigger with a decision time of 10-100 μ s. The level-0 trigger was based on scintillator signals from the beam, target, range stack and photon veto systems, processed with a combination of NIM logic and custom-built boards. The level-1.n trigger was composed of two components running in parallel, level-1.1 and -1.2 triggers, that involve partial processing of TD and ADC data, and operated on the lower rate events that pass the level-0 trigger.

The trigger was constructed in Fastbus and contained the following modules:... The trigger was upgraded for E949 with the addition of a new level-0 trigger board and mean-timers for the photon veto signals [43].

E949 collected data with triggers for $K^+ \rightarrow \pi^+ \nu \bar{\nu}$ signal, and for other physics studies and calibrations. The latter were prescaled and used for the purpose of detector calibration and monitoring and measurement of acceptance. In this paper, the triggers for calibration and other physics are called the “monitor sample”.

2.8.1 Level-0

A block diagram of the L0 trigger system is shown in Figure 16.

More description of L0 here....

The level-0 introduced a minimum of 40 ns of dead time for every coincident signal in the first two layers of the Range Stack (T·2). When an event passed the L0 trigger, the dead time was extended to 100ns to allow further processing. In total, the L0 trigger contributed 2.5% to the dead time at typical operating conditions.

2.8.2 Level-1.1

The Level-1.1 trigger was based on information from the TD system for the Range Stack counter in which the charged track was determined to have stopped. Stopped π^+ s were preferentially selected (over μ^+ s) by looking for the $\pi \rightarrow \mu$ decay by comparing the pulse height to the pulse area (for early decays) or by looking for a second detached pulse. This was done by a custom-built ASIC which had access to the TD memories.¹ For typical running conditions, L1.1 provided a decision in about 20 μ s with a rejection of ~ 11 (?) and a signal acceptance (measured after the full offline cuts) of 85%(?). (How much dead time...? 1kHz out of L0 times 20 μ s is 2%...)

2.8.3 Level-1.2

Description goes here..

The level-1.2 trigger introduced a dead time of up to 100 μ s per level-1.1 trigger.

2.8.4 $K^+ \rightarrow \pi^+ \nu \bar{\nu}$ Triggers

The trigger conditions for $K^+ \rightarrow \pi^+ \nu \bar{\nu}$ were designed differently according to the π^+ momentum. For high π^+ momentum, the trigger condition, called *pnn1*, was defined as:

$$pnn1 = \frac{KB \cdot DC \cdot (T \cdot 2) \cdot (6_{ct} + 7_{ct}) \cdot \overline{19_{ct}} \cdot zfrf \cdot L0rr1 \cdot \overline{(BV + BVL + EC)} \cdot HEX \cdot L1.1 \cdot L1.2}{(15)}$$

where *KB* required that a K^+ was identified in the K^+ Čerenkov counter, and was detected in the B4 counter and the target. The delayed coincidence (DC) required that the time of the outgoing π^+ in the IC was at least 1.5 ns later than the time of the incoming K^+ in *KB*. The $T \cdot 2$ signal was a coincidence of the OR of the IC's and the first layer of the RS (T counter) with the second layer (2 counter) in the same sector, which ensured that the π^+ entered the RS and defined the fiducial volume of the detector. The trigger bit $6_{ct} + 7_{ct}$ required that π^+ reached the 6th or 7th layer of the RS and suppressed the copious 3-body $K^+ \rightarrow \pi^+ \pi^- \pi^+$ or $K^+ \rightarrow \pi^+ \pi^0 \pi^0$ backgrounds. The $\overline{19_{ct}}$ signal required that the π^+ does not reach the 19th layer in order to suppresses $K^+ \rightarrow \mu^+ \nu_\mu$ ($K_{\mu 2}$) background. The “*ct*” designated the RS sectors that were associated with a $T \cdot 2$ ($T \cdot 2$ sector plus the next two clockwise sectors: this was the direction that a positive particle moves in the magnetic field). The *L0rr1* bit was a refined calculation of the charged track range, which includes the number of target fibers hit and a measurement of the z-position of the

¹The ASIC also reduced the TD data size for readout by discarding the waveform samples outside the “prompt” time window, keeping instead a calculation of the pulse area and leading-edge time. The prompt window typically extended from 0.5 (2) μ s before (after) the π^+ track.

track from flash TDC's on layers 10–12 as well as the deepest layer of penetration of the track; this rejected events with long range such as the μ^+ from $K_{\mu 2}$ decay. The photon veto $\overline{BV + BVL + EC}$ and HEX are from the barrel veto, barrel veto liner, endcap and RS, respectively, which removed events with photons such as $K^+ \rightarrow \pi^+ \pi^0$ ($K_{\pi 2}$), $K^+ \rightarrow \pi^0 \mu^+ \nu_\mu$ ($K_{\mu 3}$) and $K^+ \rightarrow \mu^+ \nu_\mu \gamma$ ($K_{\mu 2\gamma}$). The \overline{zfrf} condition was an fiducial cut on the z-position of the charged track in each layer from the meantimers, vetoing tracks that cross anywhere near the edge of the fiducial volume. The $L1.1$ and $L1.2$ represent the level-1.1 and level-1.2 triggers, which used data processed from the TD's and ADC's respectively.

For lower π^+ momenta the trigger condition, called $pnn2$, was defined as:

$$pnn2 = \frac{KB \cdot DC \cdot (T \cdot 2) \cdot 3_{ct} \cdot 4_{ct} \cdot 5_{ct} \cdot 6_{ct} \cdot}{(13_{ct} + \dots + 18_{ct}) \cdot 19_{ct} \cdot \overline{(BV + BVL + EC)} \cdot HEX \cdot L0rr2 \cdot L1.1 \cdot L1.2 \cdot (ps16 + \overline{C_\pi})} \quad (16)$$

Where $L0rr2$ was a cut on the refined range calculation of the low-momentum charged track (it was set to cut only events with too many target hits).

The level-0 $pnn1$ ($pnn2$) trigger had a rejection of ~ 700 (1200), combined with the level-1.1 trigger rejection of ~ 11 (10) and the level-1.2 trigger rejection of ~ 2 (2), the entire trigger therefore had a rejection of ~ 15000 (25000), and reduced the 2.6×10^6 K^+ s entering the target when the detector was live to 160 (100) events per spill.

2.8.5 Monitor Triggers

In addition to the $K^+ \rightarrow \pi^+ \nu \bar{\nu}$ triggers, there were monitor triggers for calibration and normalization, as well as triggers for other physics modes. All triggers were prescaled except for the $K^+ \rightarrow \pi^+ \nu \bar{\nu}$ triggers and the 1γ trigger for study of the decays $K^+ \rightarrow \pi^+ \gamma \gamma$ and $K^+ \rightarrow \pi^+ \gamma$.

To monitor detector performance several triggers were employed, including $K_{\pi 2}$, $K_{\mu 2}$, π^+ beam and K^+ beam. These monitor samples were used for calibration and acceptance studies. They were taken simultaneously with the pnn triggers and were prescaled so that their impact on the total dead time was small.

The $K_{\mu 2}$ decay has the largest branching ratio. Since the final state does not contain photons or additional tracks and the daughter μ^+ does not interact with the nuclei it was a convenient sample for a variety of acceptance measurements as well as several calibrations. This sample was also used for the normalization of the experiment; the measurement of the $K_{\mu 2}$ branching ratio effectively normalizes the counting of K^+ s to the well known $K_{\mu 2}$ branching ratio. The trigger condition for $K^+ \rightarrow \mu^+ \nu_\mu$ ($Km2$) was defined as follows

$$Km2 = KB \cdot (T \cdot 2) \cdot (6_{ct} + 7_{ct}) \cdot \overline{17_{ct} + 18_{ct} + 19_{ct}} \quad (17)$$

The final state of the $K_{\pi 2}$ decay mode contains one charged π^+ and two photons from π^0 decay. Since the π^+ momentum is monochromatic, it can be used to check the measurements of charged track momentum, range and energy. Also the π^+ can be used to study particle identification, and the photons can be used to study the photon veto. Two $K_{\pi 2}$ triggers were defined, a loose one, $Kp21$:

$$Kp21 = KB \cdot (T \cdot 2) \cdot (6_{ct} + 7_{ct}) \cdot \overline{19_{ct}} \quad (18)$$

and a tighter one, $Kp22$:

$$Kp22 = KB \cdot DC \cdot (T \cdot 2) \cdot (6_{ct} + 7_{ct}) \cdot \overline{19_{ct}} \cdot HEX \cdot L1.n \quad (19)$$

Among the incoming beam particles there were many π^+ s, including some that scattered into the fiducial volume of the RS. These beam π^+ s were identified by the Čerenkov counter. The kinematic features of this π^+ sample was almost the same as the $K^+ \rightarrow \pi^+ \nu \bar{\nu}$ signal except that the target pattern was different. This sample was suitable for calibrating the dE/dx of π^+ s and for studying the acceptance. The trigger condition for the beam π^+ was defined as:

$$\text{Beam } \pi^+ = \frac{\pi B \cdot \overline{DC} \cdot IC \cdot (T \cdot 2)}{(BV + BVL + EC) \cdot HEX} \quad (20)$$

In the K^+ beam trigger, only the K^+ Čerenkov counter was involved. Therefore, this monitor sample was used to evaluate the individual trigger efficiencies. The trigger condition for the K^+ beam monitor was defined as:

$$\text{Beam } K^+ = KB \quad (21)$$

The charge exchange process (CEX), $K^+ n \rightarrow p + K_L^0$ followed by $K_L^0 \rightarrow \pi^+ l^- \bar{\nu}_l$ can be a background to the $K^+ \rightarrow \pi^+ \nu \bar{\nu}$ search when the low momentum charged lepton from the K_L^0 decay is undetected. The main issue for this background study is how to precisely obtain the corresponding reaction rate. Since K^0 has equal fraction of K_L^0 and K_S^0 , there is no difference between $K^+ n \rightarrow p + K_L^0$ and $K^+ n \rightarrow p + K_S^0$. The K_S^0 decays to $\pi^+ \pi^-$ can be well identified. The decay rate as measured from $K^+ n \rightarrow p + K_S^0$ can be applied to the determination of the $K^+ \rightarrow \pi^+ \nu \bar{\nu}$ background from $K^+ n \rightarrow p + K_L^0$. The trigger condition for CEX, $K^+ n \rightarrow p + K_S^0$, $K_S^0 \rightarrow \pi^+ \pi^-$, was defined as:

$$\text{CEX} = KB \cdot \overline{DC} \cdot 2(T \cdot 2) \cdot (6_{ct} + 7_{ct}) \cdot \overline{EC + \pi B} \quad (22)$$

High energy cosmic rays can penetrate the entire detector with almost no deflection, leaving a straight track in the detector when the magnetic field is off. This feature of high energy cosmic rays can be used for the geometrical alignment of the detector elements. The trigger condition required:

$$\text{Cosmic} = T \cdot 2 \cdot IC \cdot \overline{BG} \text{ or } T \cdot 2 \cdot (> 1 \text{ non-adj IC}) \quad (23)$$

2.9 Data Acquisition

Analog- and discriminated- signals from the detector were digitized by commercial ADC and TDC, and custom-built waveform digitizer (TD and CCD) systems. When an event

Type	Model	Standard	Resolution	Subsystems
ADC				
	LRS 4300B LRS 1881	Camac Fastbus	10 bits 13 bits	RS,BV,BVL,EC,Beam TT,UTC
TDC				
	LRS 3377 LRS 1879 LRS 1876	Camac Fastbus Fastbus	0.5ns 2ns 1ns?	RS, BVL UTC,EC,Beam BV,TT
WFD				
	TD CCD	Fastbus Fastbus	500 MHz sampling 8 bits, 10 μ s depth 500 MHz sampling 8 bits, 256ns depth	RS,BVL TT,EC

Table 2: Digitizing electronics for E949 (needs to be double-checked)

was accepted by the trigger system, the digitized data for the event was transferred to a buffer module or a local crate controller. At the end of each spill, the data for the spill was transferred to a host computer. A block diagram of the DAQ system is shown in Figure 17. A summary of the digitizing electronics is in Table 2.

For the Fastbus systems, SLAC Scanner Processor (SSP) modules [44] served as crate controllers and to read out and reformat/buffer the data from the front-end after each trigger accept. The CAMAC ADCs were read out through the FERA bus by a Struck XXX DSP (Fastbus) module. The CAMAC TDC's were read out by custom-built DYC3 modules[45] which pushed the data into VME memory boards. The readout time per event (as determined by the slowest crate) was typically 850 μ s.

At the end of each spill, the data from the Fastbus buffer memories were read out via the cable segment (12-15 MB/sec) by Struck XXX SFI modules, each controlled by a MVME 2604 single-board computer (SBC) running VxWorks. The VME memory boards were read out by a separate SBC. Data was transferred from the SBC's to the host computer (SGI Origin 200) via Ethernet (9 MB/sec per link) through a simple network switch. Event fragments from the readout segments were combined by Event Builder processes running on the host computer. Complete events were distributed to "consumer" processes which included data logging and online monitoring. $K^+ \rightarrow \pi^+ \nu \bar{\nu}$ triggers were written to two DLT-7000 drives at 5 MB/sec per drive; a third DLT drive was used to log monitor triggers.

A slow control system, based on the MIDAS [46] framework, ran independently of the main DAQ system and was used to monitor a variety of experiment conditions, including crate voltages and temperatures.

Under typical running conditions, we wrote 300(?) events/spill with a typical event size of 80(?) kB. This was well within the maximum throughput of the system of about 50 MB/spill. The DAQ dead time was due entirely to the speed of the event-by-event readout of the front-end electronics at the crate level; typically this amounted to about 12(?)%.

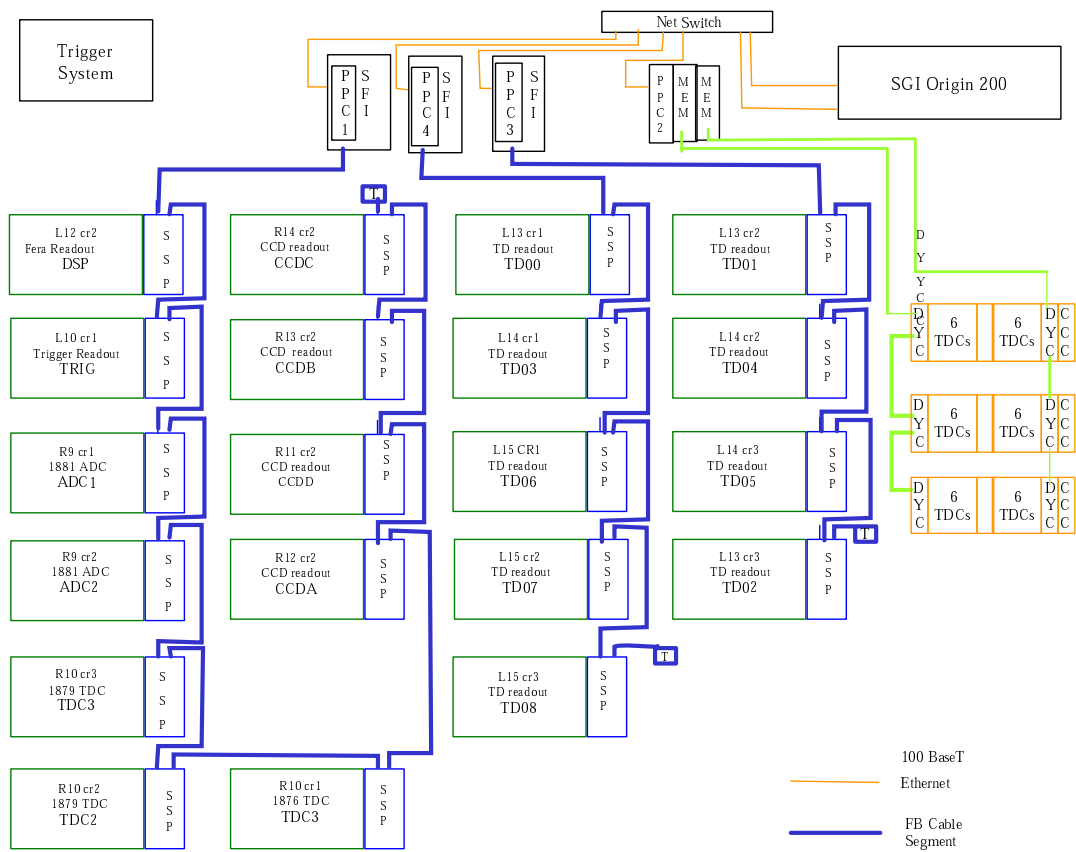


Figure 17: Block diagram of the data acquisition system.

The total dead time introduced by the trigger and DAQ was typically 25%.

2.10 Data Collection

The E949 experiment had its first physics runs for 12 weeks from March to June in 2002, about 20% out of the approved beam time by DOE. The data collected on disk in this run period corresponds to 1.77×10^{12} K^+ 's exposure in the target. The $K^+ \rightarrow \pi^+ \nu \bar{\nu}$ data sample are classified into two categories: the momentum region above and below the $K_{\pi 2}$ peak, referred as *pnn1* and *pnn2* sample.

3 Data analysis

The branching ratio of the $K^+ \rightarrow \pi^+ \nu \bar{\nu}$ decay is expected to be a level of 10^{-10} in the SM. Toward an observation of signal requires at least 10^{10} K^+ s stop in the apparatus. Considering the acceptance that can be achieved, this figure should be increased to at least 10^{12} . To ensure that an observed candidate event really come from the $K^+ \rightarrow \pi^+ \nu \bar{\nu}$ decay, one must require the backgrounds be suppressed to about 0.1 event level. In this article, only the search in the $pnn1$ region is described.

3.1 Overview of background

Although the trigger already overwhelmingly suppressed the backgrounds, the data accumulated by the trigger still contain many background events. It is therefore important to investigate the backgrounds surviving from the triggers and to understand the origin of the backgrounds. An good approach can start from a study of Figure 18. In this figure, there are various sources of background. Events in the $K_{\pi 2}$ peak are due to the π^+ tracks from $K^+ \rightarrow \pi^+ \pi^0$ decays with momenta at 205 MeV/c, energies at 108 MeV and ranges at 30 cm. Events in the $K_{\mu 2}$ peak are due to the μ^+ tracks from $K^+ \rightarrow \mu^+ \nu_\mu$ decays with momenta at 236 MeV/c, energies at 153 MeV and ranges at 55 cm. Events in the $K_{\mu 2}$ range tail are due to the μ^+ 's undering an elastic or inelastic scattering in the RS. Events in the μ^+ band are due to multi-body decays, such as radiative $K_{\mu 2}$, or $K_{\mu \nu \gamma}$ and $K_{\mu 3}$, π^+ decay in flight in the target, and $K_{\mu 2}$ decay with μ^+ undering an inelastic scattering in the target. The momentum end points of the $K_{\mu \nu \gamma}$ and $K_{\mu 3}$ decays are 236 MeV/c and 215 MeV/c, respectively. Events in the π^+ band are due to the π^+ beam surviving from the $pnn1$ or $pnn2$ trigger. Therefore, the backgrounds can be categorized into those from K^+ decays and those from non- K^+ -stop and non- K^+ decay backgrounds.

The K^+ -originated backgrounds can be further categorized into two types based on the particle type: π^+ -related and μ^+ -related backgrounds. As shown in Figure 4, the K^+ -originated backgrounds from the multi-body decays are suppressed by choosing a momentum region higher than the $K_{\pi 2}$ peak for the signal region. They can also be suppressed by the photon veto, since some of them include π^0 's in their decay. The remaining and most contributing backgrounds from K^+ decays are therefore $K_{\pi 2}$ and $K_{\mu 2}$. $K_{\mu \nu \gamma}$ can also be one of main backgrounds because the momentum of the decay can be in the signal region.

The non- K^+ -stop and non- K^+ decay backgrounds are categorized into three types: the single beam background, the double beam background, and the charge exchange interaction background.

The single beam background contains both K^+ entering and π^+ entering cases. If a single K^+ entering the apparatus decays in flight to π^+ and π^0 (see the top diagram in Figure 19), the kinematic values of the π^+ can be shifted upward due to the Lorentz boost. If the two photons from the $K_{\pi 2}$ decay are missed, such an event can fake a $K^+ \rightarrow \pi^+ \nu \bar{\nu}$ signal. It is noted that these events tend to have earlier decay timings in the target than the events of K^+ decays at rest. If a π^+ in the beam scatters in the target and then enters the fiducial region of the detector (see the bottom diagram in Figure 19), the event can fake a the $K^+ \rightarrow \pi^+ \nu \bar{\nu}$ signal because some of these scattered π^+ 's can

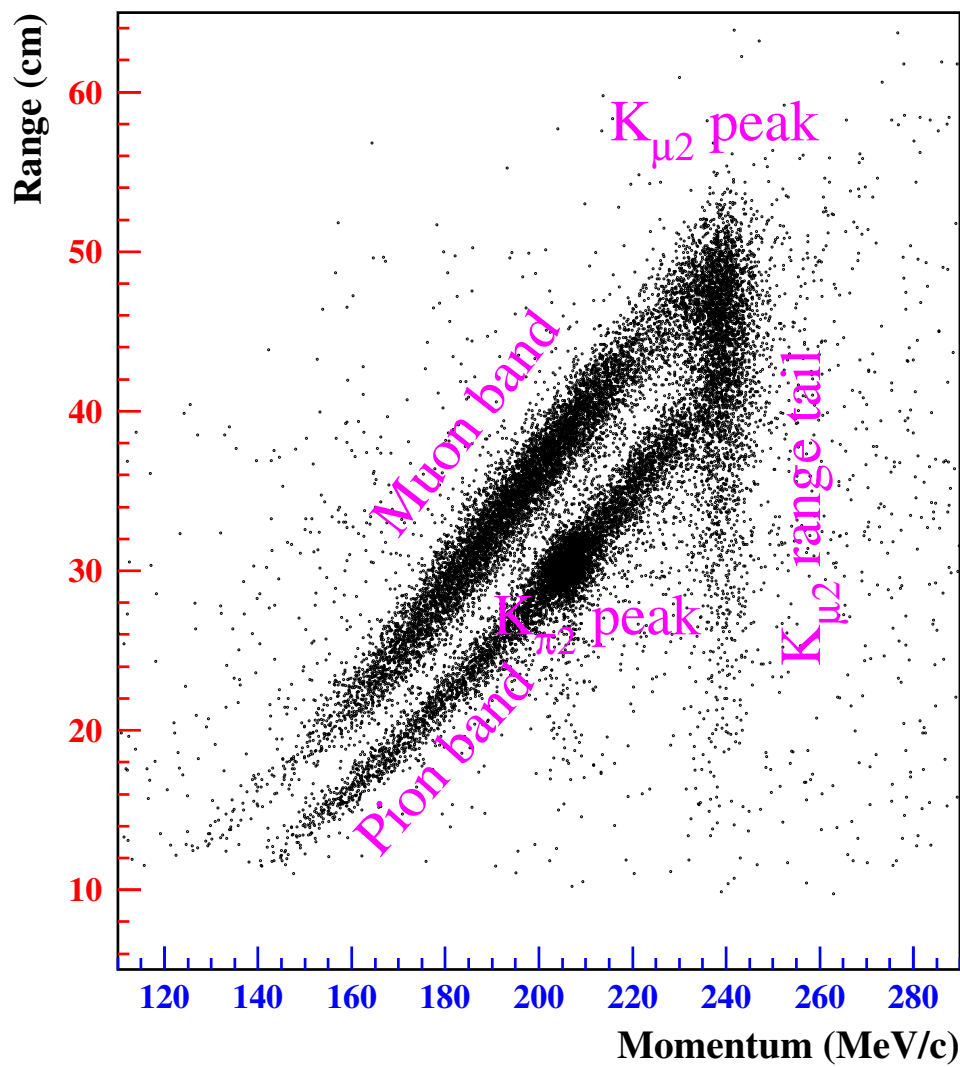


Figure 18: Range in a plastic scintillator (in cm, y -axis) versus the momentum (in MeV/c, x -axis) of the charged particles for events that pass the $pnn1$ or $pnn2$ trigger.

satisfy the kinematics of the signal. Time delay coincidence and K^+ identification using the Čerenkov counter and the B4 hodoscope measurements will be the key ingredient to reject these single beam backgrounds.

The double beam background can be categorized into two classes: $K^+ - K^+$ entering and $K^+ - \pi^+$ entering. In the $K^+ - K^+$ entering case, the first K^+ enters and comes to rest in the target, and the second K^+ entering the target decays in flight to π^+ and the π^+ enters the fiducial region of the detector (see the top diagram in Figure 20). The $K^+ - \pi^+$ case is the same as the $K^+ - K^+$ case, except that the π^+ scatters in the target and enters the fiducial region. (see the bottom diagram in Figure 20). Both cases can imitate the $K^+ \rightarrow \pi^+ \nu \bar{\nu}$ signal if the decay products from the first K^+ is missed and the second K^+ or π^+ cannot be detected in the beam line detectors. Background rejection must rely on the observation of extra activities that are coincident with the charged track in the beam instrumentation, the target, and the RS.

A K^+ beam can interact with a neutron via the strong force when propagating in the target. This reaction produces a proton and a neutral kaon ($K^+ n \rightarrow K^0 p$) and exchanges the charge of a kaon (referred as a charge exchange (CEX) process). In E949, the energy of the incoming K^+ beam is about 100 MeV, and usually can not dislodge an energetic proton from the nucleus. As a result, the energy deposited by the proton can easily be overlapped with that by the incident K^+ and becomes indistinguishable in the measurement. For the neutral kaon, the situation is different since the K^0 is a superposition of the two mass eigenstates: K_S^0 (mean life 8.95 ns) and K_L^0 (mean life 51.8 ns). The K_S^0 decays essentially 100% of the time to two pions, while about 67.6% of K_L^0 decays semi-leptonically ($K_L^0 \rightarrow \pi^\pm l^\mp \nu_l$, l stands for e or μ). In this three body decay, the energy of lepton can be too low to be detected, and faking a signal event. Because both the $pnn1$ and $pnn2$ triggers require only one charged track in each event, most of them will be rejected by the triggers. For the π^- track, it will also be rejected by the UTC track reconstruction. The signature of a K_{e3}^0 or a $K_{\mu3}^0$ background is a π^+ track plus a soft undetected e^- or μ^- (see Figure 21). Since the e^- can also have an electromagnetic shower in the target in addition to the usual minimum ionization as the μ^- , and the shower may overlap with the K^+ or π^+ fiber cluster in the target, one can expect that the K_{e3}^0 will contribute more than the $K_{\mu3}^0$ case. It is noted that a K_L^0 does not deposit energy along the path in the target, leaving a gap between K^+ and π^+ fibers in the target, Also noted that this reaction process has no time delay. Both of which can be used to reject the CEX background.

3.2 Analysis Strategy and Method

In order to make a measurement on the branching ratio of $K^+ \rightarrow \pi^+ \nu \bar{\nu}$, one must achieve a sensitivity down below 10^{-10} . To have a large suppression of the backgrounds does challenge the prevailing background estimate methods, because any measurement involving low statistics can be subject to large statistical fluctuations, and bias on developing selection criteria may be introduced, especially when dealing with a removal of a particular event based on a limited statistics. The strategy in this study is to use a blind analysis method to search for signal. That is, background sources are identified *a priori* and a signal region for the $pnn1$ is determined so that the sensitivity is expected to be

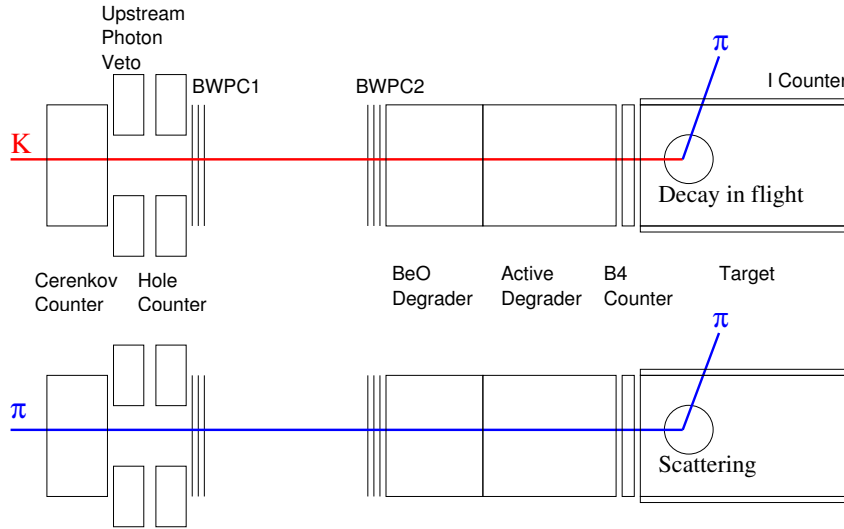


Figure 19: Schematic diagrams of the single beam background: a single K^+ beam background (top) and a single π^+ beam background (bottom).

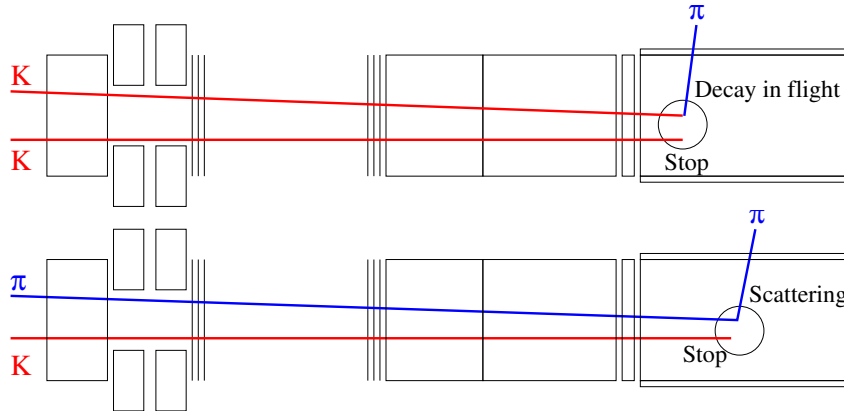


Figure 20: Schematic diagrams of the double beam background: a $K^+ - K^+$ double beam background (top) and a $K^+ - \pi^+$ double Beam background (bottom).

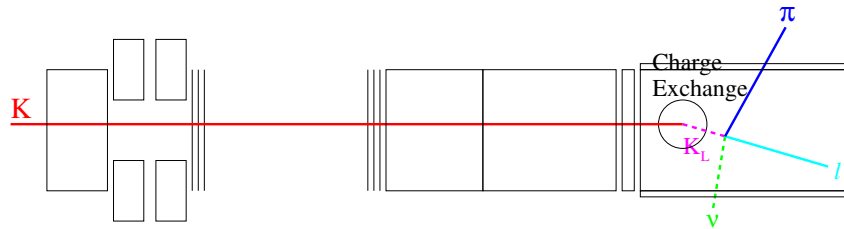


Figure 21: Schematic diagram of the charge exchange interaction background.

optimized. Throughout the analysis, the signal region is always masked out until all the cut development and the background estimation are finalized. Below are the key steps adopted in this analysis.

- Real data will be used wherever possible, because Monte Carlo simulation cannot represent the pathological events occurring in real data, especially if it is due to the hardware problems or the unexpected biases.
- A so-called bifurcation method will be exploited to evaluate the background levels. This method first chooses at least two uncorrelated cuts or groups of cuts with large background rejections, and inverts them sequentially to create high-statistic background samples from real data. Based on the background samples, one can apply simple algebra to derive the estimate of background level in the signal region. The details of the bifurcation method will be explained in Section 3.6.1.
- For a background study, the real data will be randomly divided into two portions: one-third portion of the whole data will be used to develop the cuts, and the remaining two-third portion will be used to measure the final background levels. This will help to estimate the background levels in a less-biased manner.
- Balance between the background levels and the signal acceptances will be controlled continuously by changing the severities of the cuts used in the bifurcation method. The variations of the background levels and acceptances at various cut positions will be numerically tabulated to give the so-called background functions.
- Acceptance measurement of the signal selection cuts will be conducted with the monitor trigger data whenever it is applicable. The $K^+ \rightarrow \pi^+ \nu \bar{\nu}$ phase space acceptance and the π^+ stop efficiency will be obtained from the Monte Carlo $K^+ \rightarrow \pi^+ \nu \bar{\nu}$ sample, in which both the π^+ nuclear interactions rate in the scintillators and the π^+ decay-in-flight effect will be taken into account.
- The final branching ratio will be derived from a likelihood analysis, in order to properly interpret both the signal and background distributions in the signal region.

3.3 Track reconstruction and data processing

The whole data sets collected by E949 first go through the charged track reconstruction. Further data reduction can then be processed.

3.3.1 Track reconstruction

Event reconstruction starts from the check on both the *pnn1* trigger bit and the online stopping counter in the RS. Then, the hit counters of a positively-charged track (referred as the track counters) are searched in the RS. A good T-2 sector must be the first two coincident RS layers in the same sector. From this T-2 sector, the adjacent coincident RS counters are then searched in the outgoing and clockwise direction to find the track counters. Once a RS track cluster is established, the track time will be computed by

averaging the measurements of the track counters. The offline stopping counter is defined as the outermost layer and the most clockwise sector.

After the RS track is found, the UTC track reconstruction will look for the clusters to the region around the T-2 sector of the RS track. Using a circle to fit a track in $x - y$ plane to a set of drift distances plus a left-right ambiguity solution. If an UTC track in $x - y$ plane is successfully found, the corresponding track projection on the $r - z$ plane will be searched at each UTC cathode foil, and making clusters of hit strips based on timing. A ± 15 ns of time consistence is required for the strip hits belonging the same cluster in each foil. The z position for a cluster in each foil is determined using the charge-weighted method. It is noted that this method will introduce a bias on the z position. To reduce this bias, a ratio method as suggested by Reference [52] is applied. A straight line fit is performed in $r - z$ plane if hits are found in at least 3 foils. If there are more than one track pointing to the same T-2 sector, the one which is closest to the first sector crossing in the RS or to the clock-wise edge of the stopping counter in case of no sector crossing, will be picked up as the good UTC track.

After a good UTC track is found, pattern recognition in the target is conducted to determine the K^+ and π^+ fibers using information of the UTC track extrapolation. Once the π^+ fibers are found, the procedure of UTC track fitting is repeated with the information on the π^+ passage and K^+ decay vertex in the target. This will give a better solution for the left-right ambiguity in the UTC measurement. A good charged track should also satisfy a good matching between the target and the UTC. The times of the mother K^+ and the daughter π^+ are obtained from the average of the K^+ and π^+ fiber times, respectively, while the corresponding energies are from the sums of the energy deposits in the K^+ and π^+ fibers. Since a charged track losses its energy in both the target and the IC, the total momentum of the charged track should include the measurements from the UTC, the target and the IC. Also included is the dead material effect from the inner wall of the UTC.

In the stopping counter, a pulse fitting is performed to find a $\pi^+ \rightarrow \mu^+$ decay signature. Both single-pulse and double-pulse fittings are applied to the TD pulse shape and the fitting algorithm returns the χ^2 of both single-pulse and double-pulse fittings, the energy and time of the second pulse, etc.

The total energy deposit of the track in the RS is obtained by summing up the energy deposits in the track counters. The μ^+ energy in the stopping counter is subtracted from the total energy using the result from the TD pulse fit to the stopping counter. The range of the track is calculated via a track-fitting method, taking into account that the track is propagated by losing energy with Bethe-Block equation and by bending in a 1 Tesla magnetic field. A projection of the track onto the $x - y$ plane in the RS is fitted to the sector crossing points, the RSSC hit positions and the energy in the stopping counter. The fitting χ^2 is minimized by changing the incident momentum and the angle at the entrance of the RS (see Figure 22). The projection of the track onto the $r - z$ plane in the RS is from the extrapolation of the UTC track to the center of stopping counter. In the $r - z$ plane, a matching is examined between the extrapolated positions and the measured z positions obtained from the end-to-end time differences in individual RSSCs and the RS counters. This comparison can effectively reduce the possibility that a μ^+ scatters in the RS, and leading to a wrong measurement on its kinematic observables.

The range in the RS is calculated from the path length of the fitted track, and the total range of the track is calculated by adding the target range, the IC range and the range in the dead materials of the UTC.

3.3.2 Data processing

Data collected by the *pnn1* trigger are stored on 300 magnetic tapes with a total data size up to 7 Tera bytes. In order to reduce the data to a reasonable size, two steps of data reductions are taken prior to the background study. In the first step, called "Pass 1", badly reconstructed events and obvious μ^+ and beam background events are removed by several cuts, but maintaining high acceptance for $K^+ \rightarrow \pi^+ \nu \bar{\nu}$ events. This "Pass 1" processing reduces the data by a factor of 10. In the second step, called "Pass 2", some loose versions of the final analysis cuts are applied to the "Pass 1" output data sample. In the "Pass 2" data reduction, some combinations of the "Pass 2" cuts are used to divide the data sample into 3 groups: $K_{\pi 2}$ enhanced, μ^+ enhanced and beam enhanced background samples. The $K_{\pi 2}$ enhanced sample is selected using the target reconstruction cut, the $\pi^+ \rightarrow \mu^+$ decay sequence cut and the B4 dE/dx and extra beam cuts. The μ^+ enhanced sample is selected using the target reconstruction cut, the photon veto cut, the B4 dE/dx and extra beam cuts, and the delayed coincidence cut. The beam enhanced background sample is selected using the target reconstruction cut, the photon veto cut, the $\pi^+ \rightarrow \mu^+$ decay sequence cut, and the $\pi_{scatter}$ selection cut. The developments of the bifurcation cuts and the background estimations can be performed with the Pass 2 output data sample.

3.4 Monte Carlo simulation

The detector and the physics processes in it are modeled by a Monte Carlo simulation program, called UMC, which was written specially for the E787 experiment and has been maintained by the E787 and E949 collaborators. UMC is an amalgam of subroutines from the EGS program package and a number of routines written specially for the experiments. UMC includes all of the detector elements, except for the beam instrumentation upstream of the target, and defines their geometry as close as possible to the actual ones. It generates data, except for the TD and CCD pulse-shape information, which can be analyzed with the offline analysis program for real data.

The simulation of K^+ decays in the E949 detector starts from a beam file with the x , y , z positions of K^+ decays in the target. The file for each beam condition was obtained from an analysis of corresponding $K_{\mu 2}$ monitor data, and stored the energy deposits of each K^+ in the B4 hodoscope and the target (including their accidental hits) before the K^+ came to rest. The $K^+ \rightarrow \pi^+ \nu \bar{\nu}$ decay is generated with the matrix element of semileptonic $K_{\ell 3}^+$ decay due to the (V-A) interaction. Among the K^+ decay products, photon and electron interactions and their energy deposition are calculated using the routines from the EGS4 electromagnetic-shower simulation package [50]. For heavy charged particles (μ^+ s, π^+ s, K^+ s and protons), the energy deposition is calculated by adding the energy losses of each ionization and excitation events along the steps taken by the particles. The number of ionization and excitation events is determined by dividing the total average energy deposited along the step, obtained using the Bethe-Bloch formula, by the minimum energy

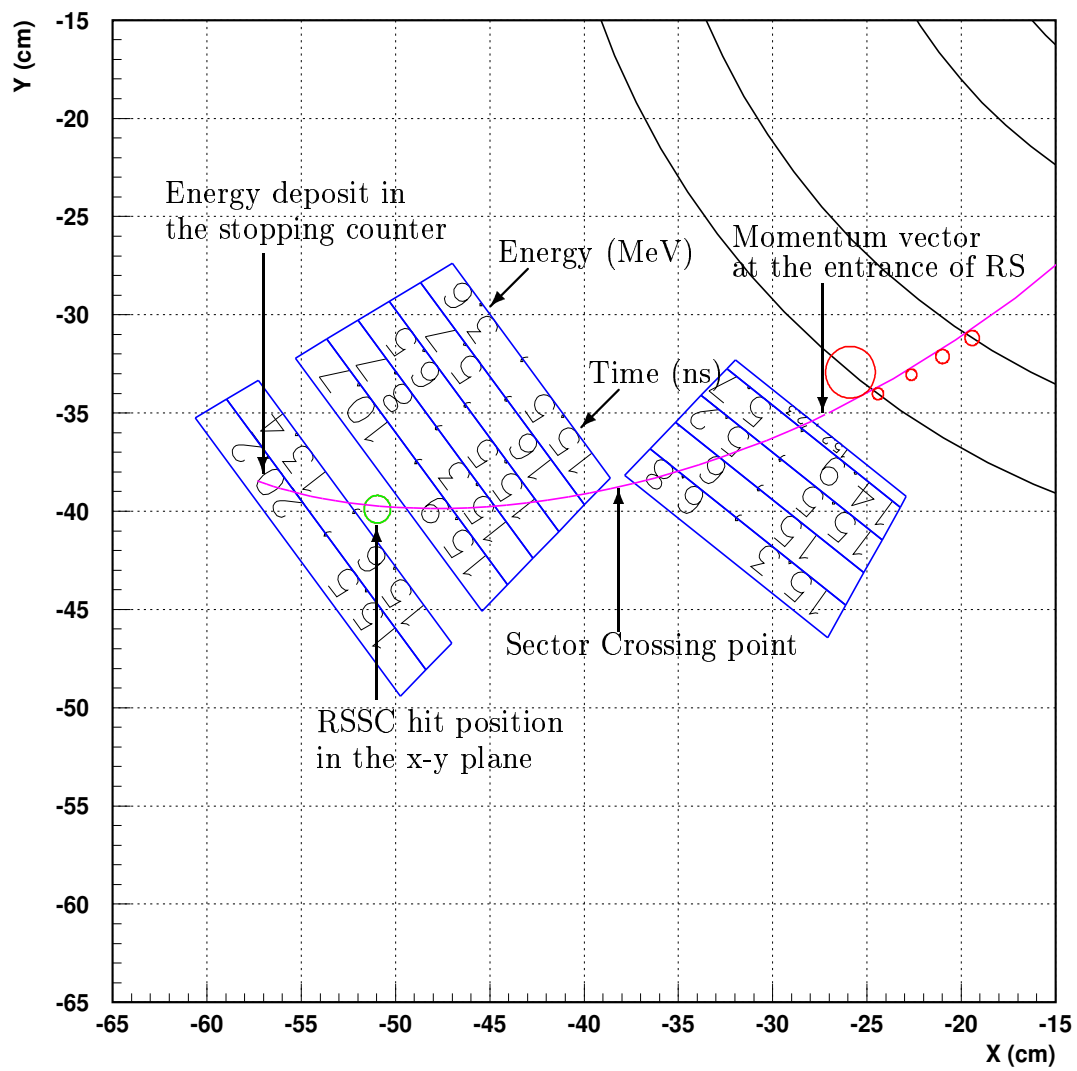


Figure 22: Range Stack track fitting in the x-y plane.

a particle loses because of an event, taken to be 65 eV. Multiple Coulomb scatterings of charged particles with various nuclei in the detector are calculated according to the theory of Moliere [47], with corrections for the spin of the scattered particle and the form factor of the nucleus [48]. Hadronic interactions of positively charged π^+ s in the plastic scintillators are calculated using a combination of data and phenomenological models [49]. There is an option in UMC allowing users to turn off nuclear absorption reactions and decays in flight of π^+ s in a simulation.

The accuracy and the performance of the UMC are verified by comparing the different kinematic variables from data and UMC for $K_{\pi 2}$ and $K_{\mu 2}$ decays. It should also be emphasized that the main role of the Monte Carlo simulation in the E949 experiment is to estimate the acceptance factors that are not obtained from real data (e.g. geometrical and trigger acceptance). In contrast to other particle-physics experiments, background studies and estimations are performed with real data, without help of simulation, except for the specific background due to Charge Exchange reaction.

3.5 Selection criteria

The selection criteria are classified into four groups: single K^+ beam selection criteria, kinematic reconstruction, π^+ identification and photon veto

3.5.1 Single K^+ beam selection criteria

It is crucial to require that a single K^+ enter the target and decay at rest. In order to ensure these requirements, several cuts explained in the following paragraphs are prepared.

Delayed Coincidence Cuts

The offline delayed coincidence cuts require that a K^+ should decay at least 2 ns later than it enters the target, namely $t_\pi - t_K \geq 2$ ns, where t_K is the target K^+ time from the average time of the target K^+ fibers, and t_π is the target π^+ time, which is the average time of the target π^+ fibers. The distribution of $t_\pi - t_K$ is shown in Figure 23. The $t_\pi - t_K$ distribution for the K^+ decays at rest shows an exponential curve with a K^+ lifetime of 12 ns, while that for the scattered π^+ s or K^+ s decaying in flight shows a prompt peak of around 0 ns. Most of these events are removed by the requirement $t_\pi - t_K \geq 2$ ns. Since the precision of timing measurement depends on how many fibers are hit by the π^+ s and the K^+ s, a number of consistency checks are also performed between the measurement of target fibers and the measurement from the other sub-detectors, in order not to introduce any beam background due to a bad timing measurement. If there is any hint of bad consistency, the above delayed coincident cut will be tightened up to 6ns.

dE/dx Cut in the B4 hodoscope

The dE/dx cut in the B4 hodoscope requires that the energy deposit of an incoming beam particle should be consistent with that of the K^+ s. The velocity (β) of K^+ s, whose energy loss in the degrader is large, is about 0.57, while that of π^+ s is about 0.97[51]. The K^+ therefore deposits more energy than the π^+ in the B4 hodoscope as shown in

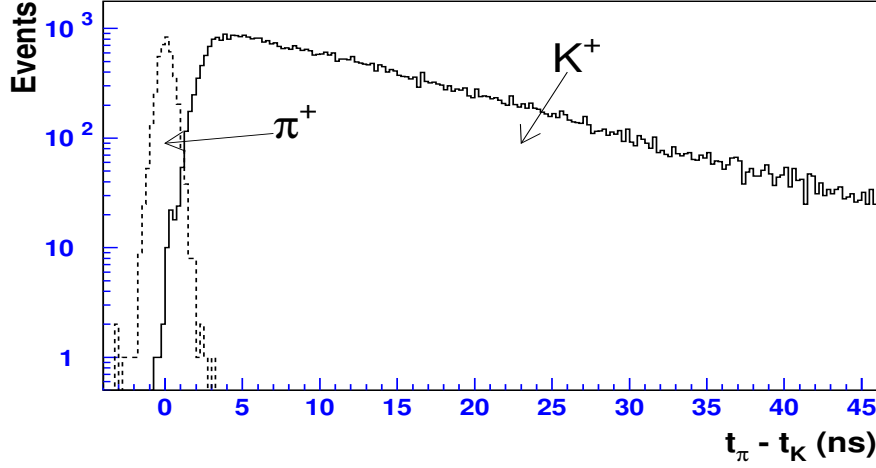


Figure 23: Distribution of the time difference, $t_\pi - t_K$, for decay-at-rest K^+ (dashed) and scattered π^+ (solid) events. The time difference for K^+ s is derived from K^+ decay events in the $K_{\mu 2}$ monitor trigger data, and that for scattered π^+ s is from Π^+ Scattering events in the $\pi\nu\bar{\nu}(1)$ trigger data.

Figure 24. Signal events are required to have a B4 dE/dx measurement greater than 1.3 MeV.

Cuts on extra beam particles at the track time

Timing measurement from the beam counters are first checked and compared to the track time determined by the RS. The TDC times measured by both the C_K and the C_π are used to compare with the track time determined by the RS. Events are rejected if the timing consistency is observed to be within ± 2 ns. Figure 25 show the single K^+ beam signal indicated by the $K_{\mu 2}$ monitor and the $pnn1$ or $pnn2$ trigger. Since the incoming K^+ beam intensity is high and can cause a TDC pile-up, the CCD times and the TDC trailing-edge times provided by the Čerenkov counters are also used to do the same comparison with the track time. Events are rejected if the CCD times of the Čerenkov counters or the TDC trailing-edge times of C_π are consistent with the track times within ± 2 ns. For the TDC trailing-edge times of C_K , the timing windows vary from ± 2 ns to ± 3.5 ns, depending on the length of K^+ decay time determined by the target fibers. The rejected timing regions for the $pnn1$ or $pnn2$ trigger do not show either a $K_{\mu 2}$ momentum peak or a $K_{\pi 2}$ momentum peak, indicating that the corresponding events are not single- K^+ beams. A close look into those events rejected by the C_K times contains almost equal amounts of single beam background and double beam background, while the single beam background increase to about 70% in the events rejected by the C_π times. Since the BWPC can provide timing measurement for the incoming beam, the times from both two chambers are also compared to the track time to see if they are within the timing windows of ± 4.5 ns. The TDC time and the CCD time measured by the B4 hodoscope are also compared to the track time. Events are rejected if the average TDC time of hit modules is within ± 2.5 ns of the track time, or the average CCD time of hit modules is

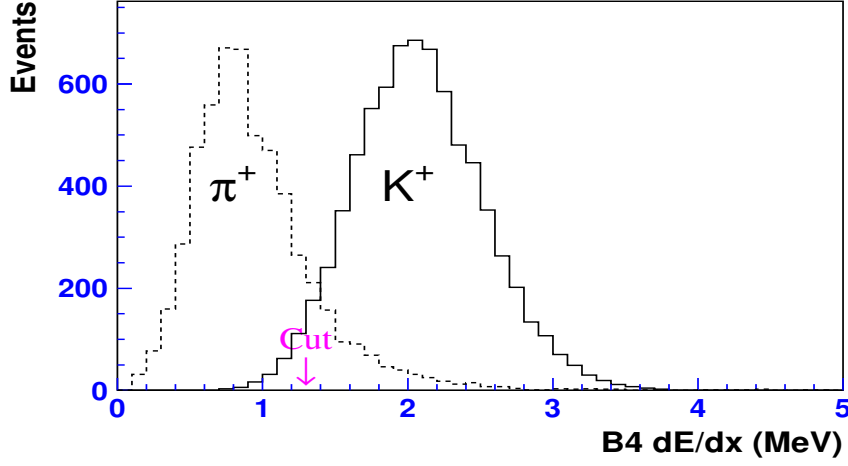


Figure 24: dE/dx in the B4 hodoscope for beam K^+ s (dashed) and π^+ s (solid). The K^+ events are derived from the K^+ decay events in the $K_{\mu 2}$ trigger data and the π^+ events are from Π^+ Scattering events in the $\pi\nu\bar{\nu}(1)$ trigger data. Events with B4 dE/dx less than 1.3 MeV are rejected.

within ± 1.5 ns of the track time. The CCD pulse shape recored by the B4 hodoscope is fitted with a double-pulse assumption. Events are rejected if an observation of double pulses show a time for the second pulse consistent with the track time within ± 3.5 ns.

Beam likelihood cut

The K^+ beam, which come to rest in the target, satisfies a relation between the energy deposits in the B4 hodoscope (B4 dE/dx), the energy deposits in the target and the stopping z positions, which are related to the K^+ path length. The stopping z position for the K^+ can be well measured by the target and can only be derived by extrapolating the UTC track to the decay vertex using the $x - y$ position measurement in the target. The stopping z positions for the scattered π^+ s or the K^+ s decaying in flight represent the positions where the scattering and decay-in-flight occurs. One will therefore expect that the path length will disagree with a normal K^+ coming to rest in the target. A likelihood is constructed by these three quantities to separate the K^+ decays at rest from the other beam particles. The likelihood values for the K^+ decays at rest and the scattered π^+ s are shown in Figure 26. This cut requires that signal events should have the likelihood value greater than 2. It also requires that a K^+ coming to rest should have an energy greater than 25 MeV and the number of K^+ fibers greater than 2.

3.5.2 Kinematic reconstruction

Since the signal is defined inside the region between the $K_{\pi 2}$ and $K_{\mu 2}$ kinematic peaks, it is very important to provide a correct measurement of the charged track kinematics and a powerful particle identification. The $K^+ \rightarrow \pi^+ \nu \bar{\nu}$ signal is selected by the following kinematic requirements:

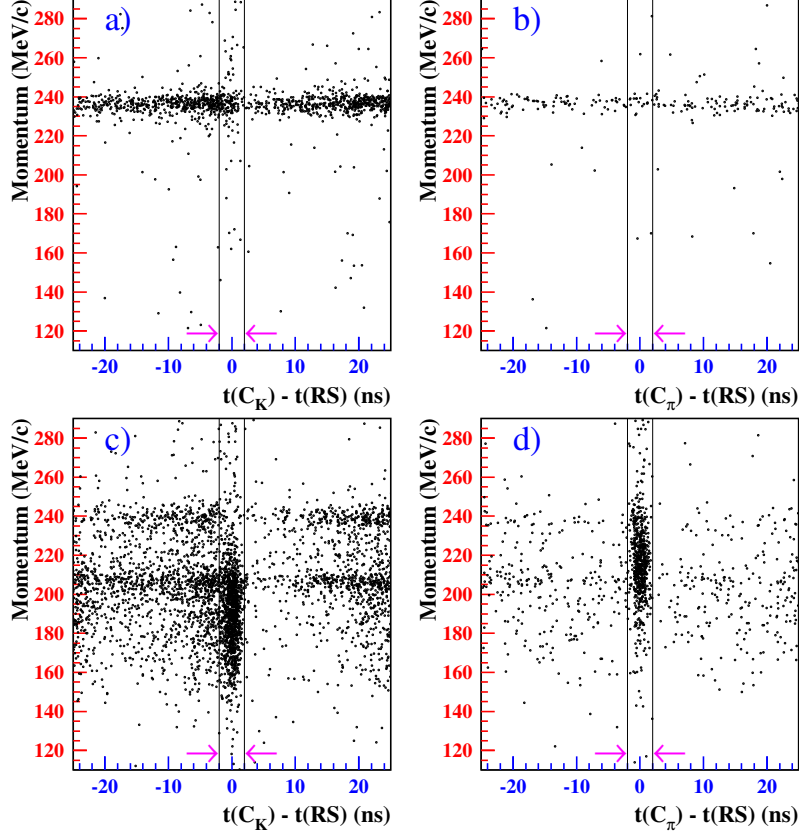


Figure 25: The momentum of charged particle versus the TDC time given by the Čerenkov counters relative to that given by the RS. $K_{\mu 2}$ monitor is used for representing the single K^+ beam events as shown in a) and b). The corresponding plots for the events in $\pi^+\nu\bar{\nu}$ triggers are shown in c) and d). The arrows indicate the rejected timing regions with beam background contamination. The statistics in these plots for $\pi^+\nu\bar{\nu}$ triggers accounts for about 0.1% of total K^+ flux.

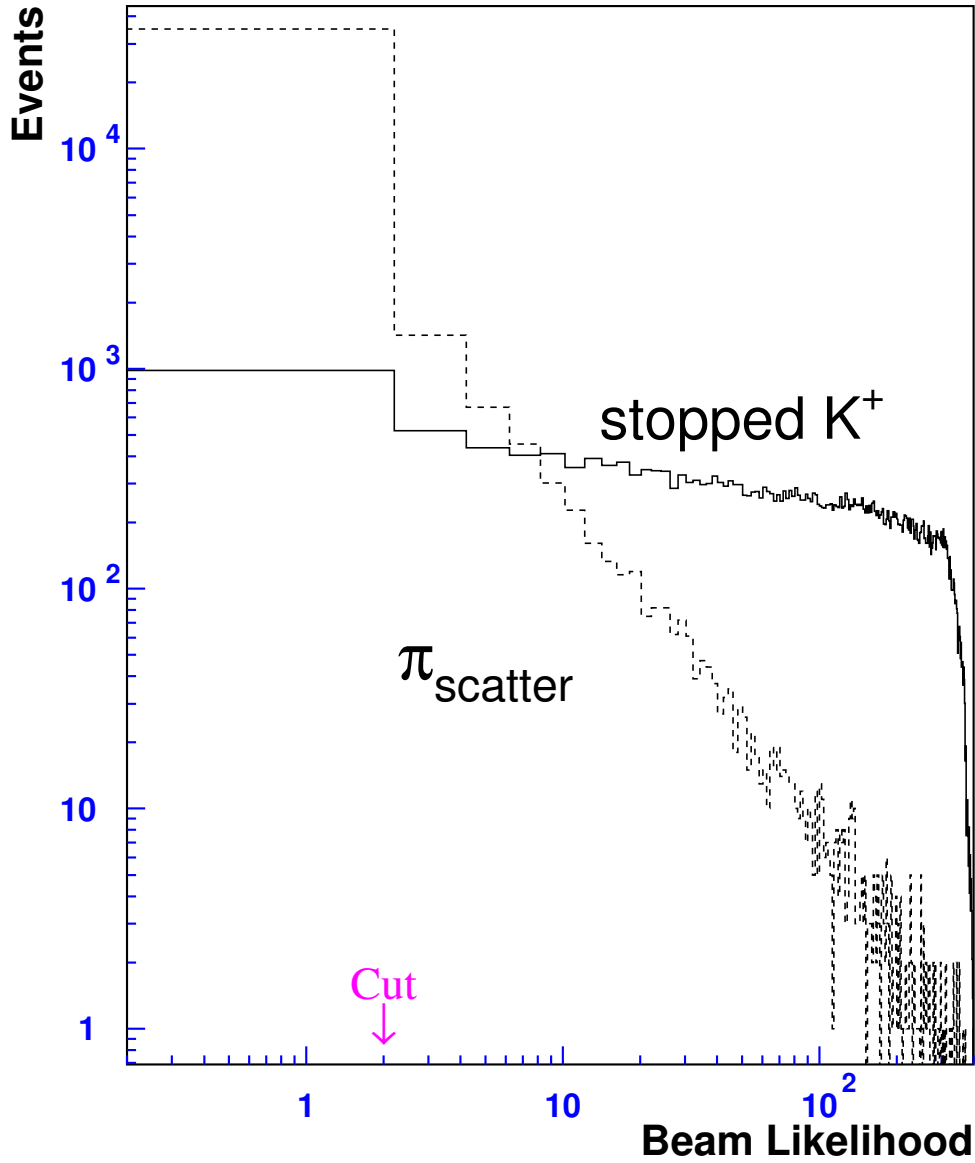


Figure 26: Beam likelihood for K^+ decays at rest (dashed) and scattered π^+ s (solid). The vertical line shows the cut position. It is required that the beam likelihood value is greater than 2. The decay-at-rest K^+ and scattered π^+ events were derived from the $K_{\mu 2}$ monitor trigger data and the $\pi\nu\bar{\nu}(1)$ trigger data, respectively.

Phase space cuts

The phase space cuts require that the momentum, kinetic energy and range should be in the following regions: $211 \leq P \leq 229$ MeV/c, $115 \leq E \leq 135$ MeV, $33 \leq R \leq 40$ cm. Since any systematic shift on either momentum or energy or range of charged track can lead to either the $K_{\pi 2}$ or the $K_{\mu 2}$ background migrating into the signal region, the above kinematic valuables are first checked. It is observed that the resolutions of these kinematic valuables are somewhat dependent on the direction angle of the charged track. The measurement suffers a worse resolution effect when a charged track has a smaller polar angle. To reduce this impact on the background level in the signal box, the Phase Space cut are tightened according to the following conditions: $(P_{meas} - P_{peak})/\sigma_P \geq 2.5$, $(E_{meas} - E_{peak})/\sigma_E \geq 2.5$, $(R_{meas} - R_{peak})/\sigma_R \geq 2.75$. Where P_{meas} , E_{meas} , R_{meas} are the measured values of momentum, energy and range, while P_{peak} , E_{peak} , and R_{peak} are the $K_{\pi 2}$ kinematic peak positions as functions of the polar and azimuthal angles, and σ_P , σ_E , and σ_R are their resolutions as a function of the polar angle.

dE/dx cuts in the range stack

A main purpose of the cuts is to remove events with energy deposits in the RS track counters that are not consistent as π^+ 's. It is noted that a μ^+ from the $K_{\mu 2}$ or a π^+ from the $K_{\pi 2}$ may become a background due to either a scattering process occurring or an overlapping photon (or accidental hit). To remove these background, one must need the dE/dx cuts in the RS, which are composed of three cuts: 1) Cut on the maximum energy deviation in each RS counter as shown in Figure 27. Events are rejected if the absolute value of the maximum deviation is greater than or equal to 4. 2) Cut on the confidence level in the RS energy measurements. A confidence level is computed with the energy deviations in all of the track counters, except for the T-Counter, the stopping counter and the counter in which a sector crossing occurs. The confidence-level distributions for π^+ and μ^+ tracks are shown in Figure 28. Events are rejected if the confidence level is less than 0.04. In the case that the maximum energy deviation is positive, the cut position on the confidence level is tightened from 0.04 to 0.2. 3) Cut on the likelihood for the RS energy measurements. A likelihood is constructed with the energy differences $\Delta E \equiv \log E_{exp}^i - \log E_{meas}^i$ for layers up to the previous layer of the stopping layer. The distributions of the likelihood value for π^+ and μ^+ tracks are shown in Figure 29. Events are rejected if the likelihood value, \mathcal{L}_{RS} , is not in the region $0 < \mathcal{L}_{RS} \leq 10$.

Range-momentum consistency cut

This cut is used to check whether the range of the charged track is consistent with that for π^+ s. A μ^+ typically has a longer range than a π^+ for a given momentum. The range deviation in the RS is defined as $\chi_{rm} = (R_{meas} - R_{exp})/\sigma_R$. Where R_{meas} is the measured range in the RS, while R_{exp} is the expected range calculated from the momentum measured by the UTC with an assumption that the track is a π^+ , and σ_R is the sigma of the measured range as a function of the momentum. The distributions of the range deviation for π^+ s and μ^+ s are shown in Figure 30. Events are rejected if the

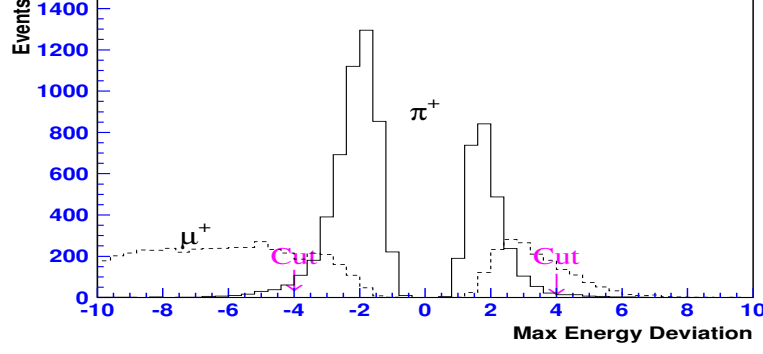


Figure 27: Distributions of the maximum energy deviation for π^+ (solid) and μ^+ (dashed) tracks. The π^+ and μ^+ events are derived from the $\pi\nu\bar{\nu}(1)$ trigger data. It is required that the maximum energy deviation is between -4 and 4 .

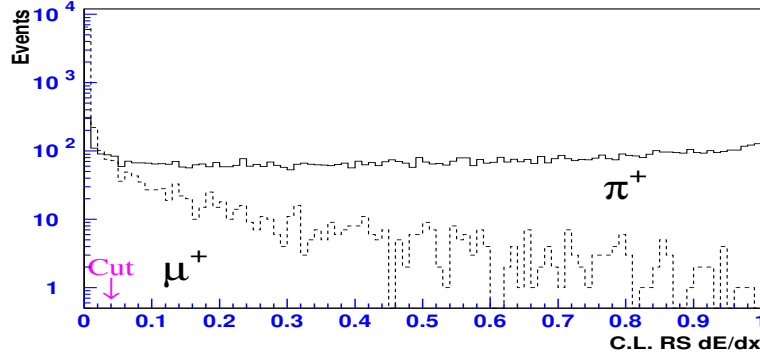


Figure 28: Distributions of the confidence level in the RS dE/dx measurement for π^+ (solid) and μ^+ (dashed) tracks. The π^+ and μ^+ events are derived from the $\pi\nu\bar{\nu}(1)$ trigger data. Events with a confidence level less than 0.04 are rejected.

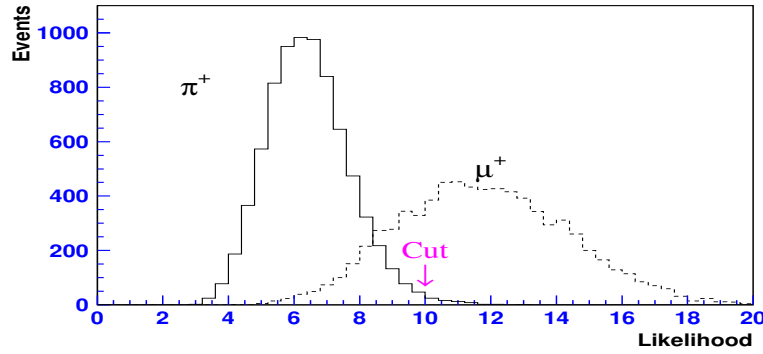


Figure 29: Distributions of the likelihood for the RS energy measurement for π^+ (solid) and μ^+ (dashed) tracks. The π^+ and μ^+ events are derived from the $\pi\nu\bar{\nu}(1)$ trigger data. It is required that the likelihood value \mathcal{L}_{RS} is $0 < \mathcal{L}_{RS} \leq 10$.

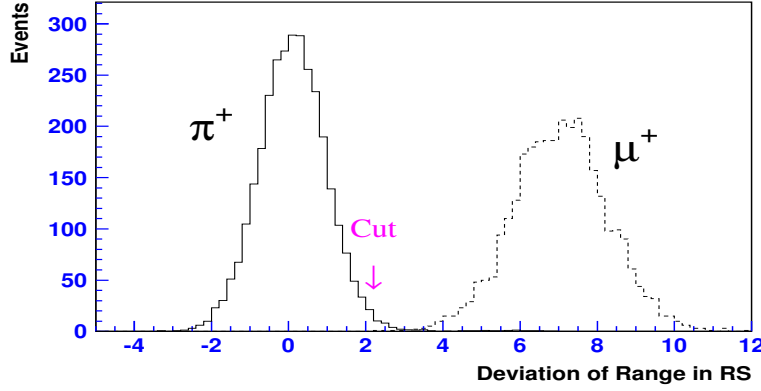


Figure 30: Distributions of the range deviation in the RS for π^+ (solid) and μ^+ (dashed) tracks. The π^+ and μ^+ events are derived from the $\pi\nu\bar{\nu}(1)$ trigger data. It is required that the range deviation is less than or equal to 2.2.

range deviation is greater than 2.2.

3.5.3 π^+ identification

Powerful π^+ identification, largely independent of the kinematic reconstruction and photon veto, is afforded by the observation of the $\pi^+ \rightarrow \mu^+ \rightarrow e^+$ decay sequence in the stopping counter. The signature for this decay sequence is as follows:

- Three energy deposits, also referred to as “pulses” in the following, typical of the $\pi^+ \rightarrow \mu^+ \rightarrow e^+$ decay sequence are found in the stopping counter corresponding to lifetime of π^+ (26.0 ns [6]) and μ^+ (2197 ns [6]) decay at rest.
- The kinetic energy of the μ^+ from $\pi^+ \rightarrow \mu^+ \nu$ decay is 4.1 MeV, but due to saturation the observed energy is 3.04 MeV [53]. The path length of a 4.1 MeV μ^+ is ~ 1.4 mm and the μ^+ exits the stopping counter without depositing more than 1 MeV in only $\sim 1\%$ of π^+ decays.
- The e^+ from $\mu^+ \rightarrow e^+ \bar{\nu}_e \nu_\mu$ decay has a kinetic energy of $E < 53$ MeV. Most of the e^+ 's exit the stopping counter and deposit energy in the other RS counters.

The three energy deposits from the $\pi^+ \rightarrow \mu^+ \rightarrow e^+$ decay sequence should be observed by the TDs and TDCs at both ends of the stopping counter. Figure 31 shows the time development of the activity in and around the stopping counter when all the activity occurs within the TD gate of $(-0.5, 2.0)\mu\text{s}$.

For the μ^+ background, only the two pulses from the $\mu^+ \rightarrow e^+$ decay are produced. A μ^+ can fake a π^+ when an extra pulse is detected in addition to the two pulses of $\mu^+ \rightarrow e^+$ decay. To suppress the μ^+ background, two stages of cuts are imposed.

In the first stage, evidence for the $\pi^+ \rightarrow \mu^+ \nu_\mu$ decay is required. The pulse development in the stopping counter as recorded by the TDs is fitted with a single- and double-pulse hypothesis in an interval of ~ 4 π^+ lifetimes (typically 104 ns). The template shapes used in the fit are derived from the average of measured pulses from μ^+ traversal for each

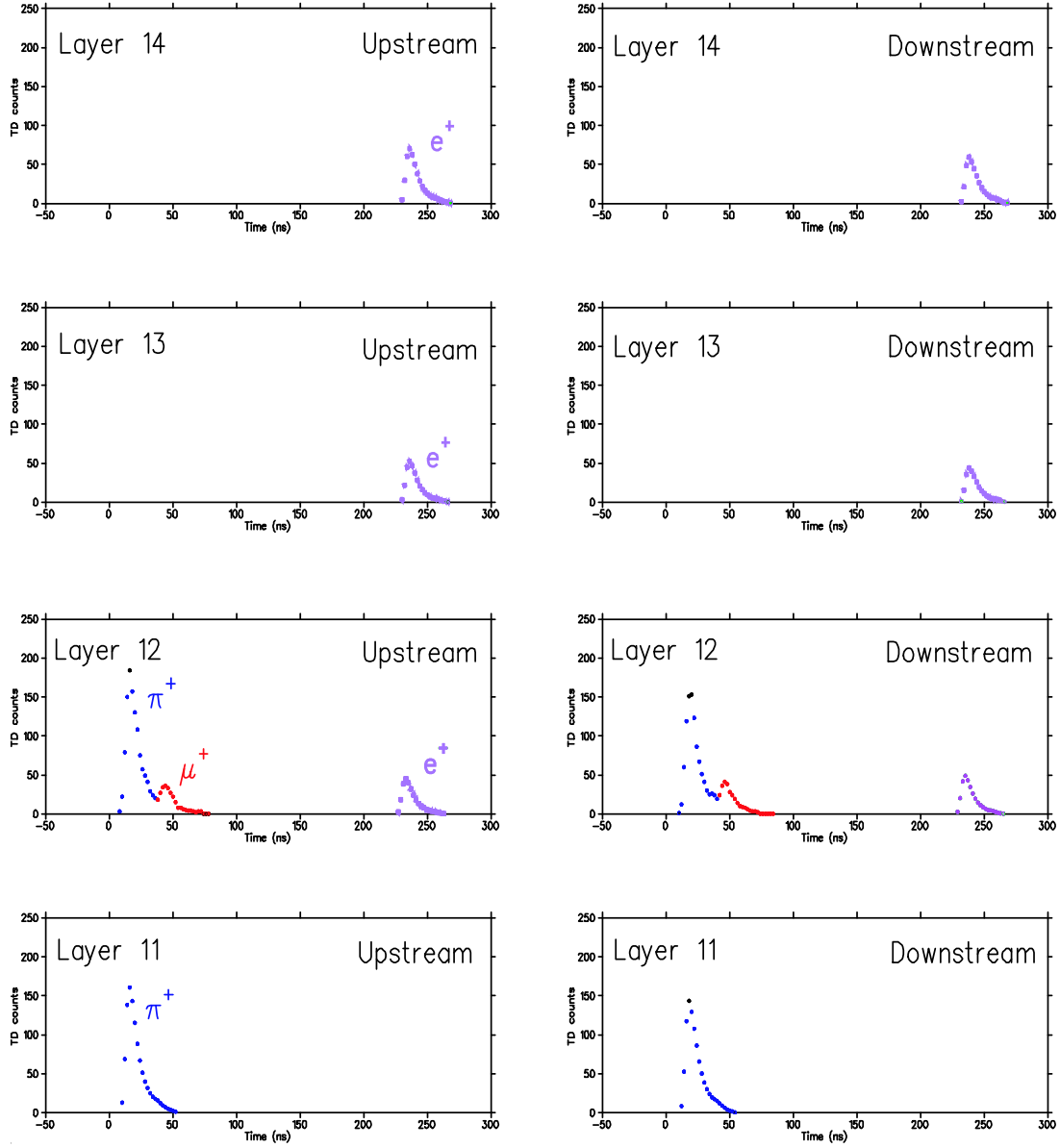


Figure 31: The pulse height in 2 ns intervals in and around the stopping counter recorded by the TDs of the upstream and downstream ends of the RS counters. The π^+ enters from the inner layers, traversing layer 11 and stopping in layer 12. The $\pi^+ \rightarrow \mu^+ \rightarrow e^+$ decay sequence is observed in the stopping counter. The μ^+ from the $\pi^+ \rightarrow \mu^+ \nu_\mu$ decay is contained in the stopping counter. The activity due to the positron from the $\mu^+ \rightarrow e^+ \nu_e \bar{\nu}_\mu$ decay occurs in the stopping counter and layers 13 and 14.

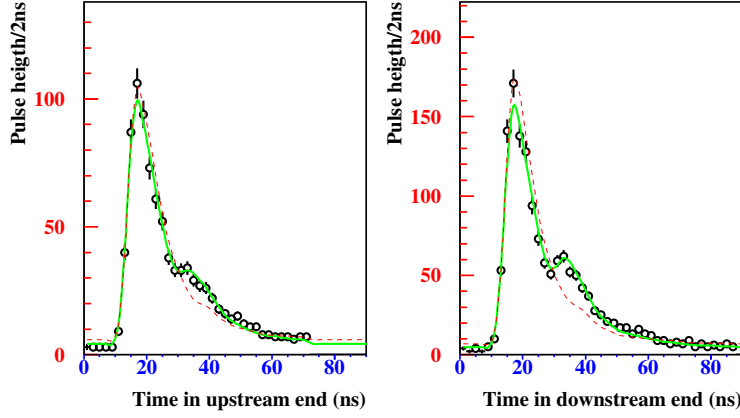


Figure 32: Results of fits with the single- and double-pulse hypotheses to the TD pulse shapes in the stopping counter for $\pi^+ \rightarrow \mu^+ \nu_\mu$ decay. The upper and lower plots are the TD pulse shapes for the downstream and upstream ends, respectively. Data (open circles) from upstream end and downstream end of the stopping counter are fitted separately. The solid curve is for the double-pulse hypothesis and the dashed curve is for the single-pulse hypothesis.

end of each RS counter. In addition, a correction is applied to the template shape to take into account the change in shape due to propagation along the counter. The parameters of the single-pulse fit are the time, the total area of the pulse and a constant corresponding to a pedestal of typically 3 TD counts. The parameters of the double-pulse fit are the time of the first pulse, the time difference of the two pulses, the total pulse area, the fractional area of the second pulse and the pedestal. A fit to a triple-pulse hypothesis is attempted if evidence for a third pulse is found based on a rudimentary analysis of the TD information or if evidence for the $\pi^+ \rightarrow \mu^+ \nu_\mu$ decay from the double-pulse fit is lacking. The two additional parameters in the fit are the time difference of the third pulse with respect to the first and the fractional area of the third pulse. The results of the single- and double-pulse fit hypotheses for $\pi^+ \rightarrow \mu^+ \nu_\mu$ decay are shown in Figure 32.

At the first stage, loose requirements are applied on the observed μ^+ energy $1 < E_\mu < 14$ MeV and on the relative quality of the results of the single- and double-pulse fits, $R(i) > 1$ and $R(1) \times R(2) > 1$ where the quantities are defined in Table 3.

At the second stage, a five cuts (Table 4) are applied to suppress the following four mechanisms when a two-pulse $\mu^+ \rightarrow e^+$ decay can fake the three-pulse $\pi^+ \rightarrow \mu^+ \rightarrow e^+$ decay sequence.

1. π^+ time accidental: Accidental activity produces the first pulse, while the $\mu^+ \rightarrow e^+$ decay gives the second and third pulses in timing sequence.
2. Early μ^+ decay: The two-pulse $\mu^+ \rightarrow e^+$ decay occurs at an early time (≤ 100 ns), producing the first and second pulses, and accidental activity makes the third pulse.
3. μ^+ time accidental: The two-pulse $\mu^+ \rightarrow e^+$ decay makes the first and third pulses, while accidental activity occurring between the time the μ^+ stops and when it decays

Quantity	Definition or use
E_μ	Energy of the second pulse
T_μ	Time of the second pulse
$\chi_N^2(i)$	χ^2 for the N -pulse hypothesis for end i ($i = 1, 2 = \text{upstream, downstream}$)
$R(i)$	$\chi_1^2(i)/\chi_2^2(i)$
$\log_{10}(R(1) \cdot R(2))$	neural net input
$\log_{10}(\chi_1^2(1) \cdot \chi_1^2(2))$	neural net input
dz	$= z_\pi - z_\mu$, neural net input component
dt	time difference between both ends for the second pulse, neural net input component

Table 3: Definitions of quantities determined by the pulse-fitting in the stopping counter. The z positions are determined from the energy ratio between the two ends of the stopping counter. The z position of the nominal π and μ pulse is z_π or z_μ , respectively. The term “second” pulse identifies the μ^+ -candidate pulse. The neural net is described in the second stage of cuts.

Cut	Π^+ time accidental	Early μ^+ decay	μ^+ time accidental	Tail Fluctuation
π^+ Time Consistency Cut	✓			
$\mu^+ \rightarrow e^+$ Decay Requirement		✓		
Cut on μ^+ Time Accidental			✓	
Cut on μ^+ Time Accidental in the Track Counters			✓	
Neural Net $\pi^+ \rightarrow \mu^+$ Decay Cut			✓	✓

Table 4: List of the backgrounds targeted by $\pi^+ \rightarrow \mu^+ \rightarrow e^+$ decay sequence cuts.

produces the second pulse.

4. Tail fluctuation: Noise induced in the transport of the signal from the PMT to the TD, dubbed “tail fluctuation”, on the falling edge of μ^+ -induced pulse is identified as the second pulse. The decay positron from the μ^+ decay makes the third pulse.

π^+ time consistency cut

This cut targets the π^+ time accidental background. When accidental activity makes the first pulse and a charged track makes the second pulse in the stopping counter, the timing of the first pulse obtained by the TD ($t_{\pi,TD}$) is not coincident with the track time (t_{RS}) obtained from the other RS counters along the track. Events are rejected if $|t_{\pi,TD} - t_{RS}| > 2.5$ ns.

$\mu^+ \rightarrow e^+$ decay requirement

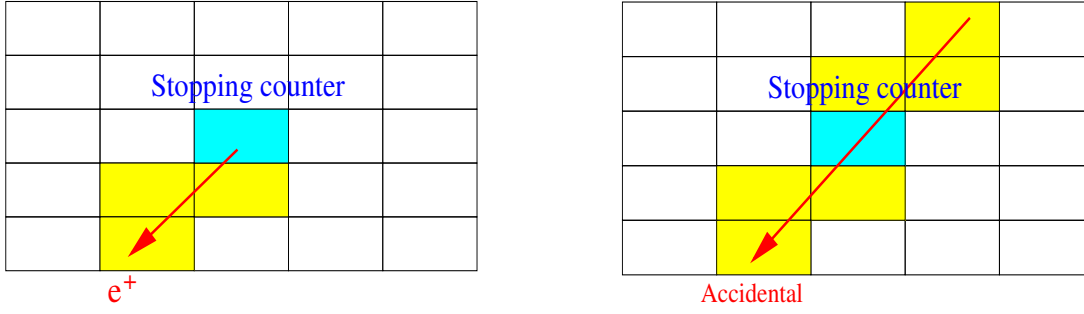


Figure 33: Schematic view of signal (left) and background (right) of the $\mu^+ \rightarrow e^+$ decay. Each rectangle represents a RS counter. The central counter represents the stopping counter and the shaded rectangles represent hit counters. The arrow indicates the possible direction of the positron or charged track producing the hits.

This cut requires that the third pulse in the stopping counter should be consistent with a positron originating from the $\mu^+ \rightarrow e^+$ decay in the stopping counter. The positron from the $\mu^+ \rightarrow e^+$ decay generally deposits energy in the stopping counter and other neighboring counters as depicted in Figure 33. The positron finding starts by looking for a cluster of TDC hits in the RS counters in the region within ± 1 sectors and ± 2 layers of the stopping counter. The cluster is required to be adjacent to the stopping counter and to have hits in the same sector as the stopping counter. Candidates for the positron are found by requiring that the average time of the hits in the cluster is coincident (within ± 2.4 ns) with the TDC time in the stopping counter. The z positions of the hits in the cluster, obtained from the end-to-end time differences of the hits, are also required to be consistent with the z position in the stopping counter. If the coincident TDC hits are due to a track that passed through the stopping counter, then hits may be found on both sides of the stopping counter (Figure 33). The positron from the stopping counter can be determined by distinguishing between one-side and both-side tracks. The early μ^+ decay background is removed by requiring that the nominal μ^+ pulse from the TD pulse fitting is inconsistent with the time of the cluster.

Cut on μ^+ time accidental

Accidental activity in the stopping counter is frequently associated with activity in other RS counters as well as the BV, BVL and EC. Hence, events with activity coincident with the μ^+ time in the stopping counter are targeted for rejection. The time windows and energy thresholds for the various subsystems in RS, BV, BVL and EC are optimized in order to have the highest rejection power at a given acceptance value of 94%. Events are rejected if the energy sum of the hits within a time window in any of the subsystems is greater than the threshold.

Cut on μ^+ time accidental in the track counters

This cut rejects the μ^+ time accidental background by performing fits to a double-pulse hypothesis in the two RS counters along the track prior to the stopping counter. The purpose is to eliminate accidental activity that overlaps the charged track and makes

a second pulse in the stopping counter. If the time of the fitted second pulse is within ± 5 ns of the μ^+ time in the stopping counter, the fitted energy of the second pulse is greater than 1 MeV and the χ^2 ratios of the single- to the double-pulse fit hypotheses, $R(i)$, are greater than four, then the event is rejected.

Neural net $\pi^+ \rightarrow \mu^+$ decay cut

This cut targets the tail fluctuation background. As mentioned previously, fluctuations in the pulse shape can originate due to noise in the transport of the signals from the PMTs to the TDs. Such fluctuations can mimic the energy deposit for a μ^+ on the falling edge of the π^+ -induced pulse, hence the term ‘tail fluctuation’. Tail fluctuations generally yield both a small time difference with respect to the first pulse and a low pulse area in the apparent second pulse. In addition, pulse fluctuations are not correlated between the two ends of the stopping counter. The variables shown in Figure 34 and described in Table 3 differ for events induced by $\pi^+ \rightarrow \mu^+ \nu_\mu$ and $\mu^+ \rightarrow e^+ \nu_e \bar{\nu}_\mu$ decay. Application of a fixed cut to each variable would cause a non-negligible acceptance loss. In order to achieve a higher acceptance at the same rejection as the fixed cuts, a Neural Network (NN) technique is adopted.

The NN function is derived via a Multi-Layer Perception (MLP) program incorporated in the library of Physics Analysis Workstation (PAW) [54]. To create the NN function, the π^+ scattering and $K_{\mu 2}$ range tail events in the $\pi \nu \bar{\nu}(1)$ trigger, which pass all other $\pi^+ \rightarrow \mu^+ \rightarrow e^+$ decay sequence cuts, are used as signal and background samples, respectively. A 5-variable NN function is obtained using the six variables shown in Figure 34 with the differences in z position and time combined to create a single input variable, $\chi^2(z, t) \equiv (dz/\sigma_{dz})^2 + (dt/\sigma_{dt})^2$, where σ_{dz} (σ_{dt}) is the resolution of the dz (dt) distribution. The distributions of the output of the NN function for π^+ s and μ^+ s are shown in Figure 35.

As an added benefit of the combination of variables in a single NN, the rejection as a function of acceptance can be easily obtained by changing the NN cut position as shown in Figure 36. The cut position at 0.76 in the output of the NN function is determined so that the acceptance of this cut is 85%.

3.5.4 Photon veto

Backgrounds from the $K_{\pi 2}$ and $K_{\mu \nu \gamma}$ decays involve photons. Since the photon energy varies from 0 to 236 MeV, especially for the $K_{\mu \nu \gamma}$ decays, the photon energy are mostly below 50 MeV [55], an effective background suppression requires a detector ability down to a few MeV. From the level that the cuts on the energy, momentum and range can achieve, the total rejection against backgrounds associated with photons is required to be in an order of 10^6 , including those from both online and offline. A rejection of 10^4 is already achieved by the online photon veto, leaving a further 10^2 rejection to be achieved by the offline analysis.

Searches for the photons coincidence with the track time are performed in the subsystems of BV, BVL, RS, EC, target, IC, VC, CO and MC. Different time windows and energy thresholds are set to the individual subsystems. For the BV, BVL and RS, whose scintillator signals are read out by both-end PMTs, energies and times of photon hits are

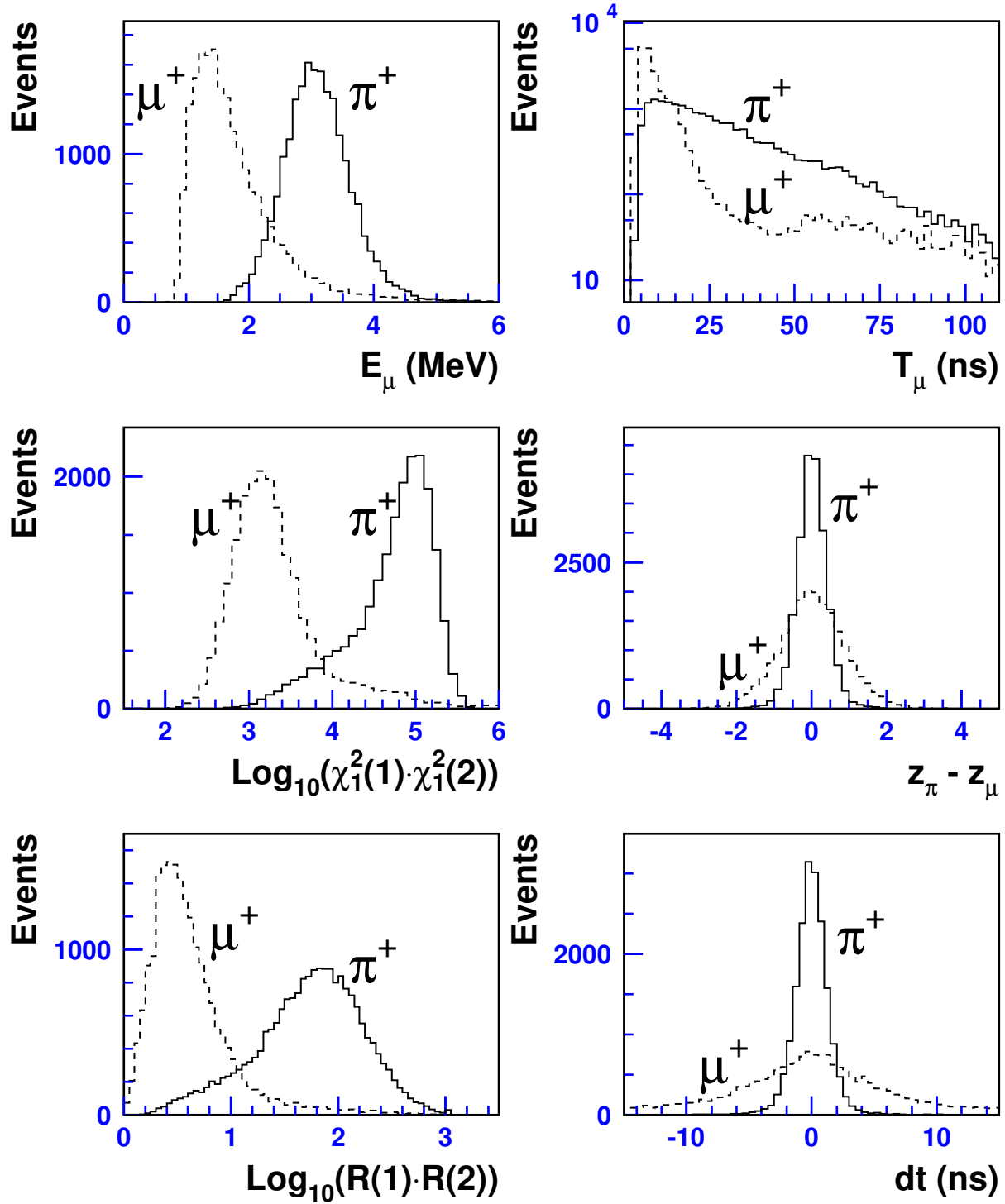


Figure 34: Distributions of the input variables for the Neural Net function in $\pi^+ \rightarrow \mu^+ \nu_\mu$ induced (solid) and $\mu^+ \rightarrow e^+ \nu_e \bar{\nu}_\mu$ induced (dashed) decays. The energy of the second pulse (top left), time of the second pulse (top middle), log of the product of the χ^2 ratios of single- to double-pulse fits for both ends (top right), log of the product of the single-pulse fit χ^2 's for both ends (bottom left), z position difference between the first and second pulses obtained from the energy ratio of both ends (bottom middle), and time difference of the second pulses in both ends (bottom right).

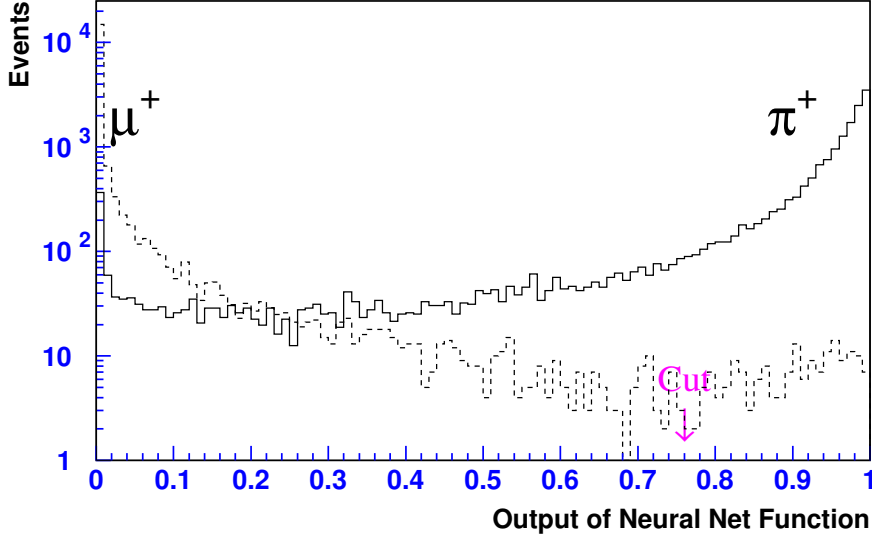


Figure 35: Distributions of the outputs of the NN function for π^+ (dashed) and μ^+ (solid) events. Events with an output of the NN function less than 0.76 are rejected.

basically obtained from the geometrical mean and the average time of both ends, respectively. Occasionally, the energies or times may be missed in a single end of the ADCs or TDCs. In order to maintain high photon veto rejection, these single-end hits are also employed by means of different time windows and energy thresholds, taking into account the worse measurement on the time and energy.

The time window and energy threshold in each category are optimized by changing their cut positions to achieve better acceptance and rejection. Signal and background are from the $K_{\pi 2}$ and $K_{\mu 2}$ peak events. Figure 37 shows the rejection of the photon veto cuts against the $K_{\pi 2}$ background as a function of acceptance. The cut position for each category is determined so that the $K_{\pi 2}$ background is reasonably suppressed in the background estimation. An acceptance of 90.5% and a rejection of 84.3 are achieved using this set of cut positions.

3.6 Signal and background

In this analysis the signal region will be masked out until all the background analyzes are completed. The data sample is randomly divided into 1/3 and 2/3 portions. The 1/3 sample will be used for cuts' tuning. And the 2/3 sample will give the final background estimations. In order to simplify the background study for $K^+ \rightarrow \pi^+ \nu \bar{\nu}$, they are categorized into four groups: 1) The $K_{\pi 2}$ background. 2) The μ^+ background, including both the $K_{\mu 2}$ range tail and μ^+ band backgrounds. 3) The beam background, including both single beam and double beam. 4) The CEX background. All of which, except for the CEX background, are estimated using the real data. A so-called “bifurcation method” is used, in order to give a reliable background evaluation.

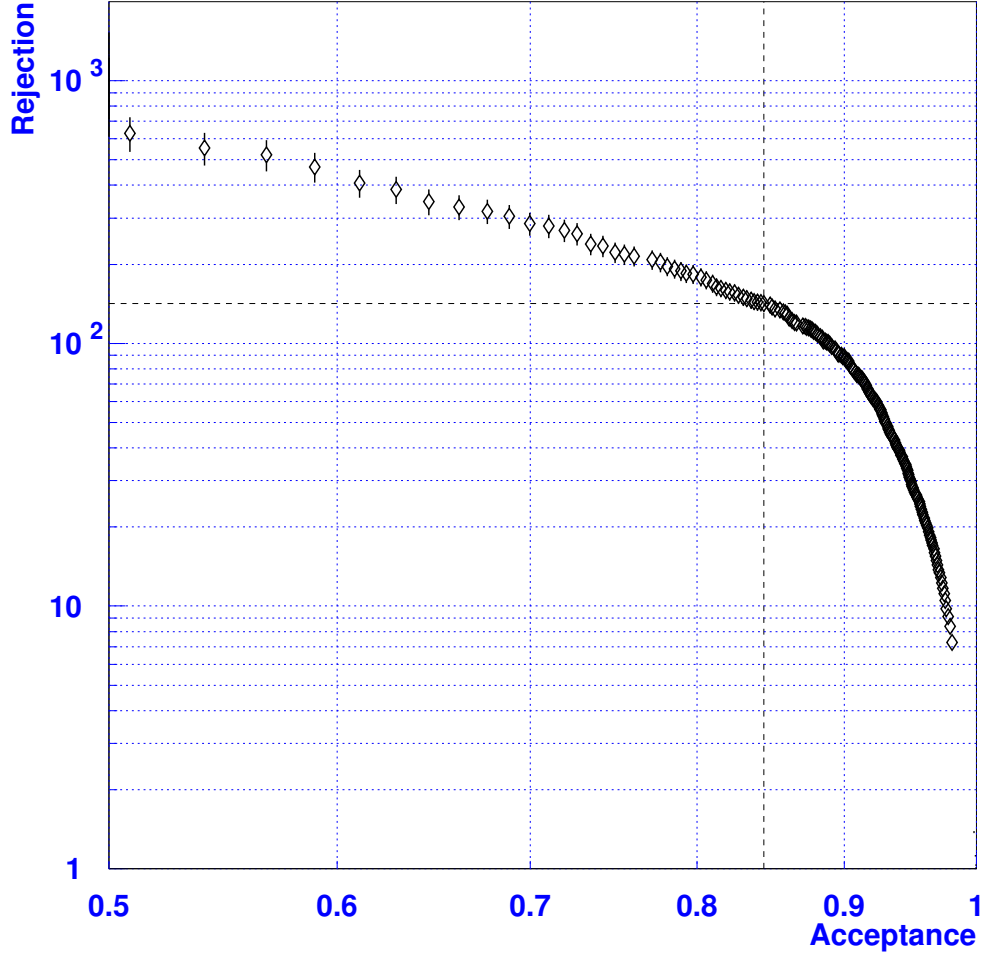


Figure 36: Rejection of the Neural Net $\pi^+ \rightarrow \mu^+$ decay cut as a function of the acceptance. The intersection of the vertical and horizontal dashed lines shows the rejection and acceptance at the nominal cut position.

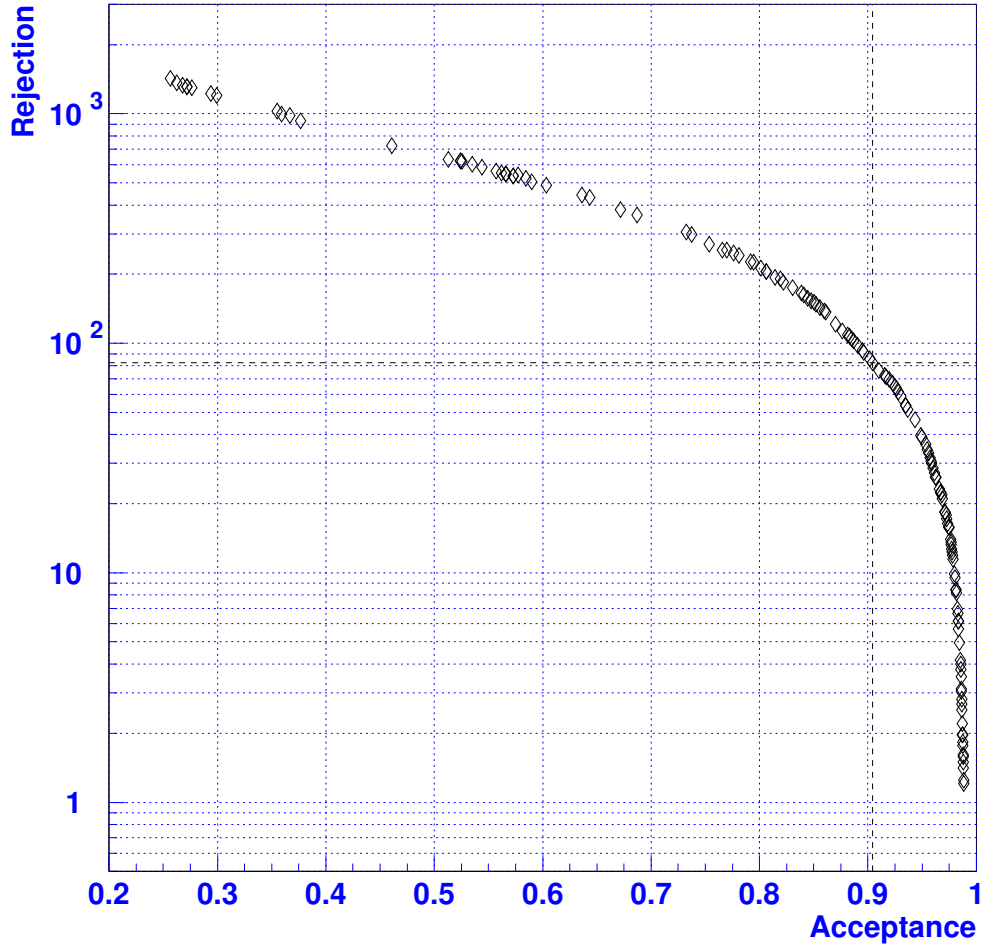


Figure 37: Rejection of the photon veto cuts against the $K_{\pi 2}$ background as a function of the acceptance. The cross point of the vertical and horizontal lines shows the rejection and acceptance at the cut position.

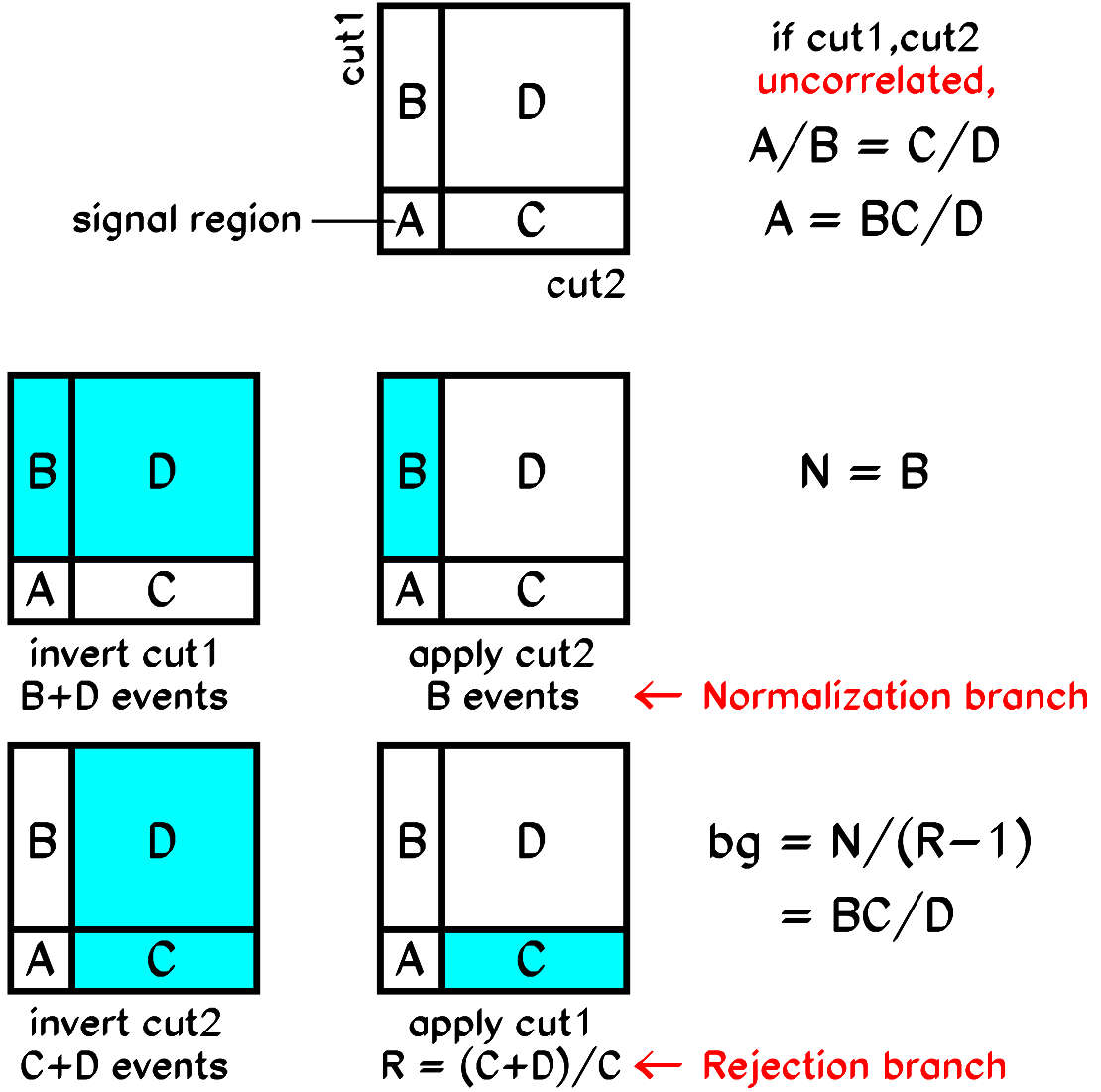


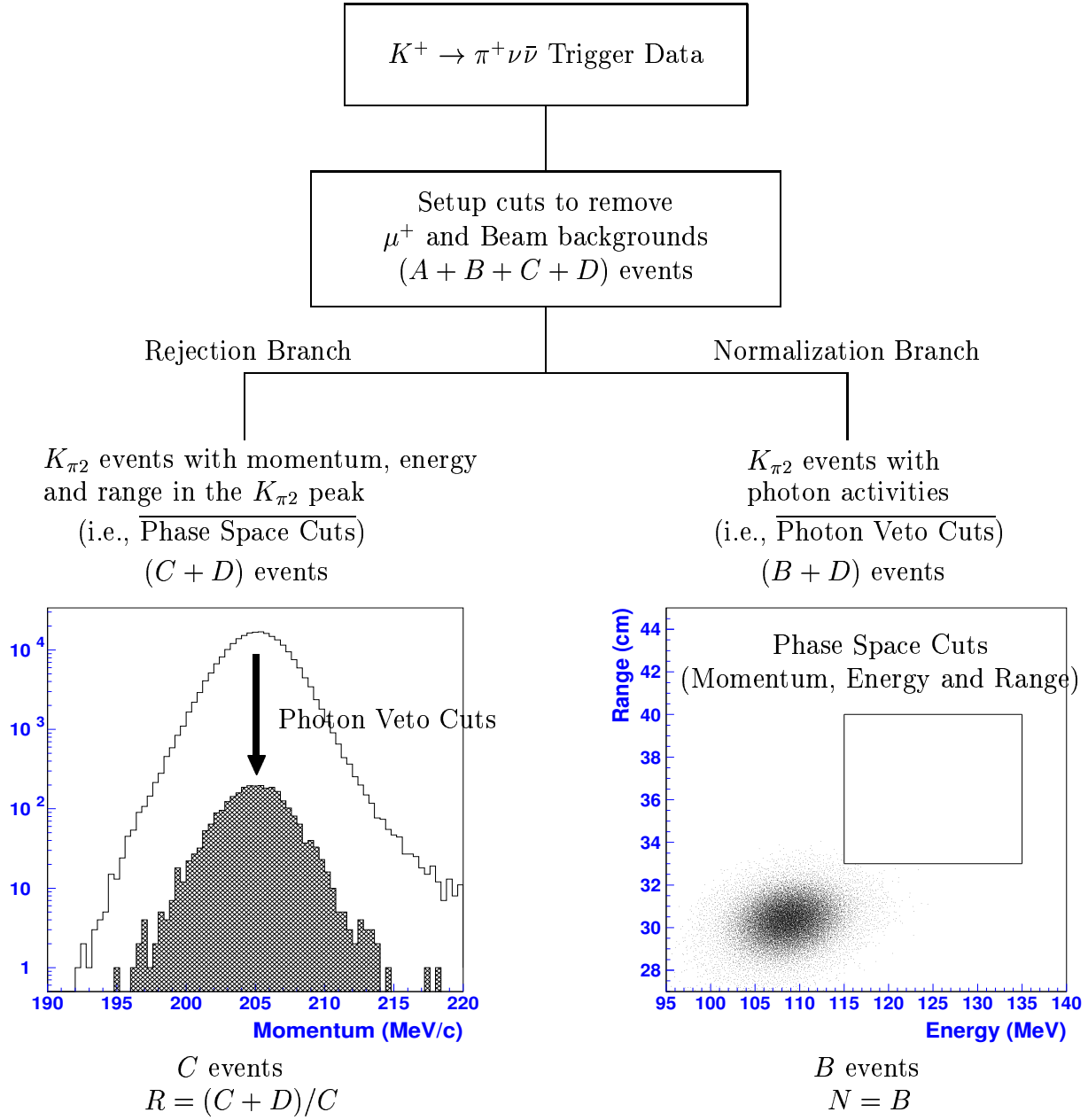
Figure 38: Pictorial explanation of the Bifurcation Method.

3.6.1 Technique of background measurement

The bifurcation method is based on the a simple algebra, and uses the large statistics outside the signal region. Three separated background regions are defined by the different cut configurations, in order to give an estimate of the background level inside the signal region. A pictorial explanation for the bifurcation method is shown in Figure 38. This method of cause must rely on the assumption that these two cuts or groups of cuts are uncorrelated. First of all, a sample targeting one specific background source is selected by removing the other background sources. The number of events remaining after applying the setup cuts is $A + B + C + D$ events. Each figure in Figure 38 shows the parameter space of two cuts, namely "cut1" and "cut2". The number of background events in the signal region (i.e., region "A") is A events. If the two cuts are uncorrelated, that is, if the rejection of a cut does not depend on the rejection of the other cut, the ratio of the

number of background events in region "A" to region "B" must be equal to the ratio in region "C" to region "D", i.e., $A/B = C/D$. Background events in the signal region are therefore obtained from the relation $A = BC/D$. This is how background levels in the signal region are estimated using events outside the signal region. In practice, the way to proceed with the bifurcation method is as follows: 1) A specific background sample is prepared by inverting "cut1" ($B + D$ events remain); "cut2" is applied to the sample and B events remain (see the second row in Figure 38). This stream is called a "normalization branch". 2) On the other hand, another background sample is also prepared by inverting "cut2" ($C + D$ events remain). By imposing "cut1", the ratio D/C is obtained (see the third row in Figure 38). The rejection factor of this "cut1", R , is calculated from the ratio $(C + D)/C$. This stream is called a "rejection branch". 3) The number of background events in the signal region is estimated by the number of events remaining in the normalization branch, N ($= B$), divided by the rejection factor, $R - 1$ ($= D/C$), i.e., $N_{Bkg} = N/(R - 1)$.

As an example, a brief explanation for the $K_{\pi 2}$ background estimation via the bifurcation method is presented in Figure 39. The $K_{\pi 2}$ background sample in the $K^+ \rightarrow \pi^+ \nu \bar{\nu}$ trigger data is selected by removing the μ^+ and Beam backgrounds (corresponding to the first row in Figure 38). In the normalization branch, $K_{\pi 2}$ events are selected by requiring photon activities (i.e., the photon veto cuts ("cut1") are inverted). The phase space cuts (i.e., cuts on momentum, energy and range, "cut2") are applied to the $K_{\pi 2}$ sample and N events remain in the normalization branch (corresponding to the second row in Figure 38). In the rejection branch, $K_{\pi 2}$ events with momentum, energy and range in the $K_{\pi 2}$ peak are selected (i.e., the phase space cuts, "cut2", are inverted). the photon veto cuts ("cut1") are applied to the $K_{\pi 2}$ events in the kinematic peak (corresponding to the third row in Figure 38) and the rejection factor of the photon veto cuts, $R - 1$, is measured. Finally, the $K_{\pi 2}$ background level is estimated based on the number of remaining events in the normalization branch (N) and the rejection factor ($R - 1$).



$$\text{Background Level (A events)} = BC/D = N/(R - 1)$$

Figure 39: Example of the Bifurcation Method.

Cuts	Loosening factor	Acceptance gain
$\pi^+ \rightarrow \mu^+ \rightarrow e^+$	4.2	$\times 1.12$
$K_{\pi 2}$ kinematic	9.5	$\times 1.12$
Photon Veto	4.0	$\times 1.07$
Total acceptance gain		$\times 1.31$

Table 5: Loosening factors for the $\pi^+ \rightarrow \mu^+ \rightarrow e^+$ decay sequence cuts, the $K_{\pi 2}$ kinematic cuts and the photon veto cuts (second column) with their acceptance gains (third column).

3.6.2 Determination of signal region

In cut developments using uniformly sampled 1/3 data in the $pnn1$ trigger, all of the cut positions have been determined. Although the signal region should basically be a region inside the cut positions of all the selection criteria, the definition of the signal region is modified, before looking into the potential signal regions, in order to enlarge the signal acceptance. The modification is motivated as follows: 1) The distributions of both signals and backgrounds in the cut space are understood well by the functions. 2) The background levels can also be controlled well in the enlarged signal regions. 3) In the likelihood ratio technique, the signal-to-background ratios of the cells that contain candidate events, not the total background level in the whole signal region, contribute to the branching-ratio measurement.

The cuts to be loosened are those related to the $K_{\pi 2}$ kinematic, photon veto and $\pi^+ \rightarrow \mu^+ \rightarrow e^+$ functions. The cuts for the μ^+ and beam backgrounds are not loosened, because the cut positions for the $K_{\mu 2}$ range tail and μ^+ band backgrounds are at the knee in the background level v.s. acceptance curve; loosening them does not provide much acceptance gain. Loosening the cut positions of the $K_{\pi 2}$ kinematic, photon veto and $\pi^+ \rightarrow \mu^+ \rightarrow e^+$ functions provides a relatively large acceptance gain. However, loosening three cuts simultaneously increases the background levels. The signal region is the combination of the following three cases: 1) The cuts for the $K_{\pi 2}$ kinematics are loosened, 2) The photon veto cuts are loosened, 3) The $\pi^+ \rightarrow \mu^+ \rightarrow e^+$ decay sequence cuts are loosened. When one of the three is loosened, the cut positions of the other two are kept unchanged. The schematic figure of the signal region in 3-dimensional space is shown in Figure 40.

The revised (enlarged) signal region consists of the standard signal region, which is created without loosening any cuts, plus three extensions. Hereafter, the revised and standard signal regions are referred to as the signal region and the 1×1 region, respectively. The regions created by loosening the photon veto cuts, $\pi^+ \rightarrow \mu^+ \rightarrow e^+$ decay sequence cuts and $K_{\pi 2}$ kinematic cuts are referred to as PV extended, $\pi^+ \rightarrow \mu^+ \rightarrow e^+$ extended and $K_{\pi 2}$ kinematics extended regions, respectively. All of which include the 1×1 region. The loosening factors for the cuts ($f_{\pi\mu e}$, $f_{K\pi 2}$ and f_{PV}) are developed so that the background levels after loosening them are acceptable. The loosening factors and acceptance gains are summarized in Table 5. The loosening factors for these three cuts are $f_{\pi\mu e} = 4.2$, $f_{K\pi 2} = 9.5$ and $f_{PV} = 4.0$, which means 4.2-times more background related to the $\pi^+ \rightarrow \mu^+ \rightarrow e^+$ identification, 9.5-times more $K_{\pi 2}$ background and 4.0-times more background related to Photon Veto. The total acceptance gain by enlarging the signal

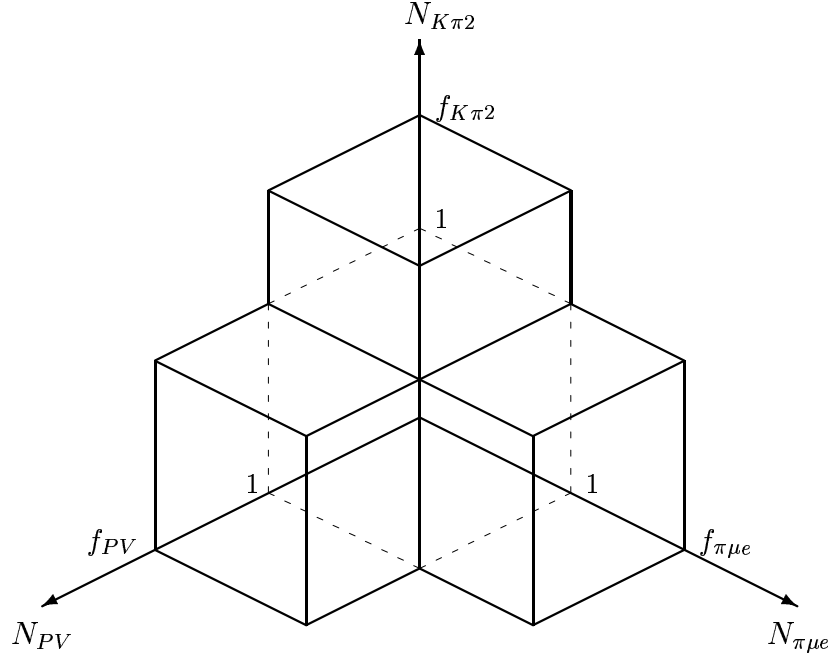


Figure 40: Schematic figure of the signal region in the 3-dimensional parameter space of the $\pi^+ \rightarrow \mu^+ \rightarrow e^+$, $K_{\pi 2}$ kinematic and photon veto functions (in the unit of relative background level).

region is 31%, which is the sum of the individual acceptance gains (12% from $K_{\pi 2}$, 12% from $\pi^+ \rightarrow \mu^+ \rightarrow e^+$ identification, and 7% from the photon veto).

3.6.3 $K_{\pi 2}$ background

The $K_{\pi 2}$ decay has a charged track with monochromatic momentum, range and energy, and has two photons at the track time. Two cuts used in the bifurcation are therefore the phase space cuts to the π^+ track and the photon veto Cuts.

The $K_{\pi 2}$ background level is estimated in the following way. Setup cuts are applied to the $pnn1$ trigger sample in order to remove other backgrounds, and to select events with well-reconstructed π^+ tracks. In the rejection branch, $K_{\pi 2}$ peak events are selected (i.e., inverse of the phase space cuts), giving a measurement on the rejection of the photon veto cuts

$$R_{PV} = \frac{481362}{5710} = 84.3 \pm 1.2(stat.). \quad (24)$$

In the normalization branch, $K_{\pi 2}$ events are selected by requiring photon activities (i.e., inverse of the photon veto cuts). The phase space cuts with $P_{dev} \geq 2.5$, $E_{dev} \geq 2.5$ and $R_{dev} \geq 2.75$ are imposed on this sample, giving a measurement on the number of events in the normalization branch. It is observed that the phase space cuts almost get rid of the $K_{\pi 2}$ events, leaving the statistics is so low that the background estimate suffers too much statistical fluctuation. In order to perform a more precise estimation, this analysis also apply a so-called second bifurcation method on the study of the normalization branch.

In the second bifurcation, the phase space cut on the energy and on the range and momentum are separated as two independent cuts, since the energy measurement is independent of the other two measurements. The expected number of events in the normalization branch (N_{NB}) can be estimated by $N_{NB} = N_{RP}/(R_E - 1)$, where N_{RP} is the number of events that remain after the range and momentum cuts are imposed, and R_E is the rejection for the energy cut only.

The second bifurcation method estimates 1.04 ± 0.20 events in the normalization branch, giving a smaller error than that in the first bifurcation. To get the estimations for the PV extended, $\pi^+ \rightarrow \mu^+ \rightarrow e^+$ extended and $K_{\pi 2}$ kinematics extended regions, one can perform the study in the same way as the 1×1 region, except that the corresponding cuts are loosened. The expected numbers of events in the normalization branch are summarized in Table 6.

Region	N_{NB} (events)
1×1	1.04 ± 0.20
PV Extended	0.97 ± 0.24
$\pi^+ \rightarrow \mu^+ \rightarrow e^+$ Extended	1.15 ± 0.20
$K_{\pi 2}$ Kinematics Extended	9.01 ± 1.00

Table 6: Expected numbers of events remaining in the normalization branch. The errors are statistical.

The background level in the signal region is evaluated by the sum of the background levels in the individual extended regions. Since each extended region contains the 1×1 region, the over-counted background should be subtracted as illustrated in Figure 41. The $K_{\pi 2}$ background level in the signal region is therefore obtained in the following way:

$$N_{K_{\pi 2}} = 1.5 \times \left[\frac{N_{NB}(PV)}{R'_{PV} - 1} + \frac{N_{NB}(\pi\mu e)}{R_{PV} - 1} + \frac{N_{NB}(K_{\pi 2})}{R_{PV} - 1} - 2 \frac{N_{NB}(1 \times 1)}{R_{PV} - 1} \right], \quad (25)$$

where R'_{PV} represents the photon veto rejection at the loose cut position and is by a factor of 4 smaller than the standard photon veto rejection. In this analysis, the photon veto rejection at the loose cut position is used for the estimation in the PV extended region. The coefficient 1.5 is the normalization factor from a 2/3 sample to the full sample. The $K_{\pi 2}$ background level is estimated to be

$$N_{K_{\pi 2}} = 0.216 \pm 0.023(stat.) \quad \text{in the Signal Region}, \quad (26)$$

$$N_{K_{\pi 2}} = 0.019 \pm 0.005(stat.) \quad \text{in the } 1 \times 1 \text{ Region}. \quad (27)$$

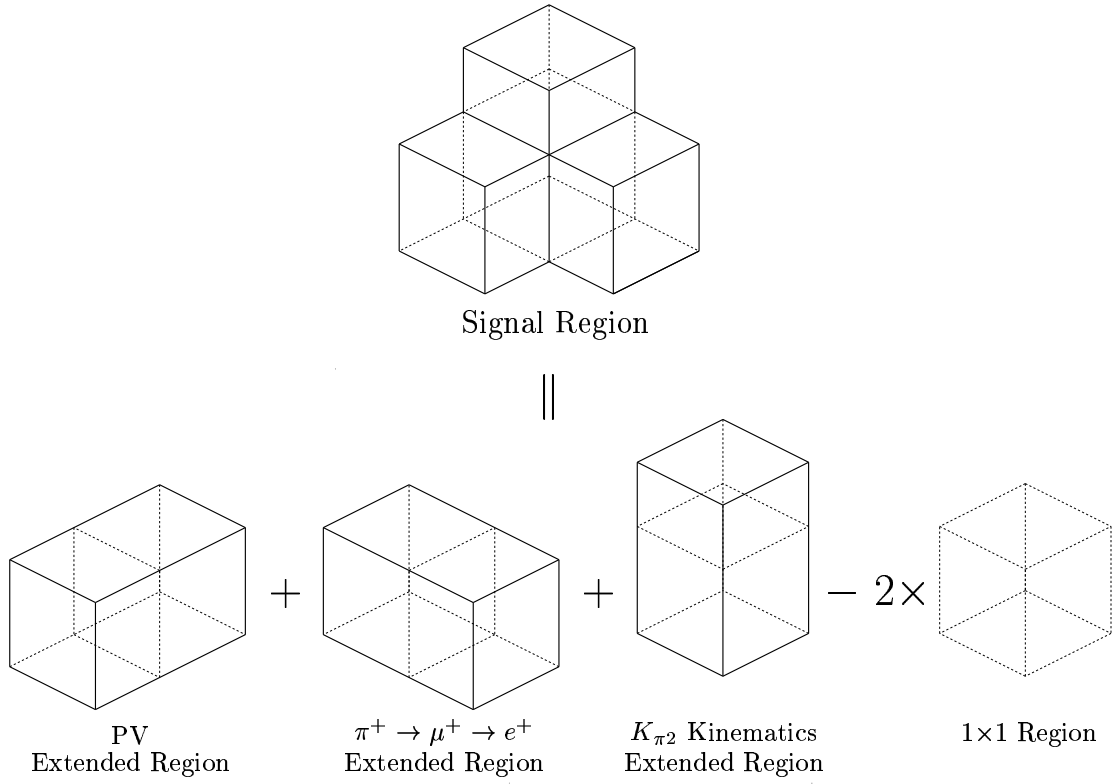


Figure 41: Method of the background level calculation in the signal region.

3.6.4 μ^+ background

The μ^+ background consists of the $K_{\mu 2}$ range tail events and the μ^+ band events as indicated in Figure 18. All of these μ^+ 's come to rest, or interacts in the RS. The $\pi^+ \rightarrow \mu^+ \rightarrow e^+$ decay sequence cuts can significantly suppress these events. Independent from this cut, the cut on the lower boundary of momentum and the cut on the range-momentum are also the effective cuts to suppress the the $K_{\mu 2}$ range tail and the μ^+ band background, respectively.

The μ^+ background level is estimated in the following way. Setup cuts are applied to the $pnn1$ trigger sample, removing the $K_{\pi 2}$ and beam backgrounds in it. The $\pi^+ \rightarrow \mu^+$ double pulse fitting cut is applied to select events with the $\pi^+ \rightarrow \mu^+$ decay signature. In the rejection branch, the $K_{\mu 2}$ range tail events are selected by inverting the momentum cut, while the μ^+ band events are selected by inverting the range-momentum cut. The phase space cuts on the range and energy are required for both backgrounds. The rejection of the $\pi^+ \rightarrow \mu^+ \rightarrow e^+$ decay sequence cuts is measured for the whole μ^+ background as given below

$$R_{\pi\mu e} = \frac{38268}{85} = 450.2 \pm 48.8(stat.). \quad (28)$$

In the normalization branch, the μ^+ events that fail the $\pi^+ \rightarrow \mu^+ \rightarrow e^+$ decay sequence cuts are selected. The number of μ^+ events remaining in the normalization branch is obtained by applying the phase space cuts and all other kinematic cuts. Since only a few events remain in the normalization branch, the second bifurcation method is also performed. This method treats the $K_{\mu 2}$ range tail and μ^+ band events separately. The background levels in the signal region are estimated by using the template momentum and range deviation distributions (referred as the line shape method).

The estimation from the line shape method gives 4.65 ± 0.14 and 2.19 ± 0.14 events of the $K_{\mu 2}$ range tail and μ^+ band backgrounds in the normalization branch, respectively. Results for the extended regions are also estimated as summarized in Table 7. The

Region	N_{NB} (events)	
	μ^+ Band	$K_{\mu 2}$ Range Tail
1×1	2.19 ± 0.14	4.65 ± 0.14
PV Extended	3.85 ± 0.24	5.07 ± 0.14
$\pi^+ \rightarrow \mu^+ \rightarrow e^+$ Extended	2.18 ± 0.14	4.56 ± 0.13
$K_{\pi 2}$ Kinematics Extended	2.27 ± 0.14	4.65 ± 0.14

Table 7: Numbers of events remaining in the normalization branch for the estimations of the μ^+ band and $K_{\mu 2}$ range tail background levels. The errors are statistical.

$K_{\mu 2}$ range tail and μ^+ band background levels in the signal region are obtained by

$$N_{\mu^+} = \frac{N_{NB}(PV)}{R_{\pi\mu e} - 1} + \frac{N_{NB}(\pi\mu e)}{R'_{\pi\mu e} - 1} + \frac{N_{NB}(K_{\pi 2})}{R_{\pi\mu e} - 1} - 2 \frac{N_{NB}(1 \times 1)}{R_{\pi\mu e} - 1}, \quad (29)$$

where $R'_{\pi\mu e}$ represents a rejection of the $\pi^+ \rightarrow \mu^+ \rightarrow e^+$ decay sequence cuts at the loose cut position and is by a factor of 4.2 smaller than the standard one. In this analysis,

the rejection of the $\pi^+ \rightarrow \mu^+ \rightarrow e^+$ decay sequence cuts at the loose cut position should be used for estimations in the $\pi^+ \rightarrow \mu^+ \rightarrow e^+$ extended region. The final μ^+ background levels in the signal region for the $K_{\mu 2}$ range tail and μ^+ band backgrounds are given in Table 8.

Background	Signal Region	1×1 Region
$K_{\mu 2}$ Range Tail	0.0439 ± 0.0050	0.0103 ± 0.0011
μ^+ Band	0.0244 ± 0.0030	0.0049 ± 0.0006
Total	0.0683 ± 0.0058	0.0152 ± 0.0013

Table 8: Summary of the μ^+ background levels. The errors are statistical only.

The μ^+ background level is therefore estimated to be

$$N_{\mu^+} = 0.0683 \pm 0.0058(stat.) \quad \text{in the signal region,} \quad (30)$$

$$N_{\mu^+} = 0.0152 \pm 0.0013(stat.) \quad \text{in the } 1 \times 1 \text{ region.} \quad (31)$$

3.6.5 Single beam background

The single beam background events are defined as either the beam π^+ 's scattering or the beam K^+ 's decaying in flight in the target, in which the later one also includes the beam K^+ 's decay between the Čerenkov counter and the target. In both cases the incoming particles scatter or decay immediately after they enter the target. The delayed coincidence cuts can therefore be used to suppress the type of background. In addition, the timing cuts in the beam instrumentation can also suppress the single beam background, since the times are expected to be close to the track time measured in the RS due to the prompt scattering or decay. These two cuts will be used in the bifurcation study for the single beam background.

The analysis is performed in the following way. Setup cuts are first applied to the $pnn1$ trigger sample to remove other backgrounds. In the rejection branch, the photon veto cuts except for the ones using the measurement from target are applied to remove $K_{\pi 2}$, $K_{\mu\nu\gamma}$, and $K_{\mu 3}$ decay-in-flight events. The delayed coincidence rejection is measured with the π^+ scattering events, which are tagged by requiring a small dE/dx measurement from the B4 hodoscope. The delayed coincidence rejection for K^+ decay-in-flight events is assumed to be the same as that for the π^+ scattering events, since it is difficult to isolate K^+ decay-in-flight events without ambiguity. It is noted that the contribution of the K^+ decay-in-flight events is much smaller than that of the π^+ scattering events, and can thus be neglected. The delayed coincidence rejection is summarized in Table 9.

Region	Rejection
Signal Region	$56178/16 = 3511.1 \pm 877.7$
1×1 Region	$51471/16 = 3216.9 \pm 804.1$

Table 9: Rejection of the delayed coincidence cuts for the single beam background.

In the normalization branch, some additional setup cuts are applied for cleanup the other type for background. The prompt events are tagged by inverting the delayed coincidence cuts. The π^+ scattering and K^+ decay-in-flight events are both estimated together. The timing cut in the K^+ Čerenkov counter, the photon veto cuts and the $\pi^+ \rightarrow \mu^+ \rightarrow e^+$ decay sequence cuts are applied to suppress the $K_{\pi 2}$, $K_{\mu\nu\gamma}$ and $K_{\mu 3}$ decay-in-flight events. The timing cut in the π^+ Čerenkov counter and the dE/dx cut in the B4 hodoscope are also applied to suppress the π^+ scattering events. There are 14 events remaining in the signal region, in which 9 out of these 14 events are observed in the 1×1 region. With the rejection of delayed coincidence measured above, the background level of single beam is estimated to be

$$N_{1BM} = \frac{1.5 \times 14}{3511.1 - 1} = 0.00598 \pm 0.00219(stat.) \quad \text{in the signal region,} \quad (32)$$

$$N_{1BM} = \frac{1.5 \times 9}{3216.9 - 1} = 0.00420 \pm 0.00175(stat.) \quad \text{in the } 1 \times 1 \text{ region.} \quad (33)$$

Again, the coefficient 1.5 is the normalization factor from the $2/3$ sample to the full sample.

3.6.6 Double beam background

The double beam background events include those with extra K^+ 's or π^+ 's in addition to the K^+ 's that come at first. When both beam particles are K^+ , this event is called as a $K^+ - K^+$ event. When the π^+ comes after the studied K^+ , this event is called as a $K^+ - \pi^+$ event. Because of the time difference between these two beam particles, the timings used the delayed coincidence cuts are not the usual meaning of $t_{K^+} - t_{\pi^+}$, and cannot be used to remove the double beam background. One way to reject this background is to the timing of each beam particle registered by the beam instrumentation, including the K^+ and π^+ Čerenkov counters, BWPCs and B4 hodoscope, since the second beam particle is correlated to the track time produced by the extra K^+ or π^+ . The other way is to use the target pattern recognition to find out the extra particles other than the initial K^+ hit.

The double beam background level is estimated in the following way. Setup cuts are applied to the *pnn1* trigger sample in order to remove $K_{\pi 2}$, μ^+ and single beam backgrounds. In the rejection branch, some additional setup cuts are applied to select π^+ tracks. The double beam background events are selected by requiring hits in the B4 hodoscope at the track time. The rejection of the timing cuts in the K^+ (π^+) Čerenkov counter and BWPCs is measured with the $K^+ - K^+$ ($K^+ - \pi^+$) events tagged by requiring that the second particle has a large (small) dE/dx in the B4 hodoscope. The rejections are summarized in Table 10.

Region	$K - K$ event	$K - \pi$ event
Signal Region	2454/28 = 87.6±16.5	43876/14 = 3134.0±837.5
1×1 Region	2323/27 = 86.0±16.5	42661/14 = 3047.2±814.3

Table 10: Rejection of the timing cuts in the beam instrumentation for the double beam background.

In the normalization branch, the estimations for the $K^+ - K^+$ and $K^+ - \pi^+$ events are separately performed with the second bifurcation method. The predicted numbers of the $K^+ - K^+$ and $K^+ - \pi^+$ events remaining in the normalization branch are $N_K = 0.16$ and $N_\pi = 0.30$ ($N_K = 0.15$ and $N_\pi = 0.29$ in the 1×1 region), respectively. With the measured rejection of the timing cuts in the beam instrumentation, the double beam background level is estimated to be

$$N_{2beam} = 1.5 \times \left(\frac{0.156}{87.6 - 1} + \frac{0.298}{3134.0 - 1} \right) = 0.00284 \pm 0.00207(stat.) \quad (34)$$

in the signal region and

$$N_{2beam} = 1.5 \times \left(\frac{0.152}{86.0 - 1} + \frac{0.293}{3047.2 - 1} \right) = 0.00283 \pm 0.00207(stat.) \quad (35)$$

in the 1×1 region.

3.6.7 Charge exchange background

A charge exchange (CEX) reaction of K^+ in the target creates a K_L^0 . The semi-leptonic decay of $K_L^0 \rightarrow \pi^+ l^- \bar{\nu}_l$ could produce a π^+ track with the kinematic values in the signal

phase space. As described in Section 3.1, the CEX events are expected to have a gap between the fibers of the incoming K^+ and the outgoing π^+ , and to have an extra l^- track. This gives a particular target pattern that can be used to remove the CEX background. In addition, a CEX event usually has no time delay, especially when the K_L^0 decays not so far away from the location where it is created. The time delayed coincidence cut can be applied to remove this type of background. Therefore, the same cuts used for the other beam backgrounds can also be applied to remove the CEX background.

There is no reliable way to isolate the CEX events from the data, the background estimate can only rely on the Monte Carlo simulation. However, the simulation needs a number of inputs, such as the CEX cross section as a function of energy, the decay vertex and momentum of K_L^0 , etc, which cannot be well modelled without looking into the real data. Since the K_S^0 created from a CEX process has no difference from its counterpart K_L^0 in term of the cross section, momentum distribution, etc, one can apply the knowledge obtained from the study of K_S^0 to the K_L^0 case. In this analysis, two charged tracks in the final state for the $K_S^0 \rightarrow \pi^+\pi^-$ decay is used as a distinguish feature in designing the corresponding trigger. By analyzing the K_S^0 trigger data, one can observe a clear K_S^0 signal in the two-pion invariant mass. These selected K_S^0 events are used to measure the K_S^0 production rate, momentum spectrum, decay vertex distribution, and pattern of target K^+ fibers' time and energy. From a study of the K_S^0 events, one can calculate the K_L^0 production rate by means of

$$R_{K_L^0} \equiv \frac{N_{K_S^0}}{\epsilon_{K_S^0} \cdot A_{PV} \cdot \mathcal{B}(K_S^0 \rightarrow \pi^+\pi^-) \cdot KB_{live}/PS}, \quad (36)$$

$$= 2.73 \times 10^{-5} \quad (37)$$

Where the quantities used this calculation are summarized in Table 11. Monte Carlo

Description	Parameter	Values
# of selected K_S^0 events	$N_{K_S^0}$	8086
K_S^0 selection efficiency	$\epsilon_{K_S^0}$	0.138
Photon Veto efficiency	A_{PV}	0.680
$K_S^0 \rightarrow \pi^+\pi^-$ Branching Ratio	$\mathcal{B}(K_S^0 \rightarrow \pi^+\pi^-)$	0.686
# of K^+ Triggers (10^{12})	KB_{live}	1.77
Prescale Factor	PS	384
K_L^0 Production Rate	$R_{K_L^0}$	2.73×10^{-5}

Table 11: K_L^0 production rate and the quantities that are used to estimate it.

simulates both $K_L^0 \rightarrow \pi^+\mu^-\bar{\nu}_\mu$ ($K_{\mu 3}^0$) and $K_L^0 \rightarrow \pi^+e^-\bar{\nu}_e$ ($K_{e 3}^0$) decays to estimate the CEX background level. In total, there are 2.076×10^{11} events generated for each decay mode, divided by the K_L^0 production rate gives 7.604×10^{15} for the corresponding number of K^+ entering the target.

These Monte Carlo events pass through all of the signal selection cuts, except for the $\pi^+ \rightarrow \mu^+ \rightarrow e^+$ decay sequence cuts and the beam cuts that are not related to the target quantities. Seventy-seven K_L^0 events survive in the signal region, in which 67 events are

in the 1×1 region. It is observed that 56 events are from the K_{e3}^0 decay mode and 21 are from the $K_{\mu 3}^0$ decay mode. Therefore, the expected CEX events can be estimated by means of

$$\begin{aligned}
N_{CEX} &= \left(N_{pass}^{K_{e3}^0} \times \frac{KB_{live}^{real}}{KB_{live}^{MC}} + N_{pass}^{K_{\mu 3}^0} \times \frac{KB_{live}^{real}}{KB_{live}^{MC}} \right) \times A \\
&= \left(56 \times \frac{1.77 \times 10^{12}}{7.604 \times 10^{15}} + 21 \times \frac{1.77 \times 10^{12}}{7.604 \times 10^{15}} \right) \times 0.250 \\
&= 0.00448 \pm 0.00051(stat.),
\end{aligned} \tag{38}$$

where $N_{pass}^{K_{e3}^0}$ and $N_{pass}^{K_{\mu 3}^0}$ are the numbers of K_{e3}^0 and $K_{\mu 3}^0$ events passing all cuts, KB_{live}^{real} is the KB_{live} for the real data and A is the acceptance of the cuts that are not used for the Monte Carlo CEX events, and estimated to be 0.250. The error is taken from the statistical error of the surviving Monte Carlo events.

3.6.8 Correlation study and single cut failure study

In the bifurcation method, it is assumed that the two bifurcation cuts used are not correlated; if there are correlations, the estimation becomes unreliable. The method is tested by comparing the predicted and observed rates near but outside the signal region. If the distributions of each background source both inside and outside the signal region are well understood with the two functions associated with the bifurcation cuts, the amount of the background inside and outside the signal region should be estimated correctly. A schematic representation of the region near, but outside, the signal region is shown in Figure 42. A region outside the Signal Region (A' in Figure 42) is defined by loosening two Bifurcation cuts ($cut1$ and $cut2$) simultaneously by fixed factors a and b , respectively. It should be noted that the Signal Region is still masked out. This region A' is referred to as the “outside-the-box” region. If the background functions associated with the $cut1$ and $cut2$ are correct, the expected number of background events in the outside-the-box region is estimated to be

$$BG(\text{predicted}) = a \times b \times BG(1 \times 1 \text{ Region}) - BG(\text{Signal Region}), \tag{39}$$

where $BG(1 \times 1 \text{ Region})$ and $BG(\text{Signal Region})$ are the background levels in the 1×1 and Signal Regions, respectively. If a deviation between the number of observed events in the outside-the-box region and this predicted number of background events is observed, then a correlation between the bifurcation cuts could be indicated and the background estimate may be unreliable. The observation is performed in the same way as the bifurcation method used in the background estimation in the signal region, except that two bifurcation cuts are loosened by factors of a and b .

The results of the correlation study for the $K_{\pi 2}$, $K_{\mu 2}$ range tail and μ^+ band backgrounds are summarized in Table 12.

To quantify the degree of consistency in Table 12, the observations and predictions are fitted with the form

$$N_{\text{obs}} = c \times N_{\text{pred}}, \tag{40}$$

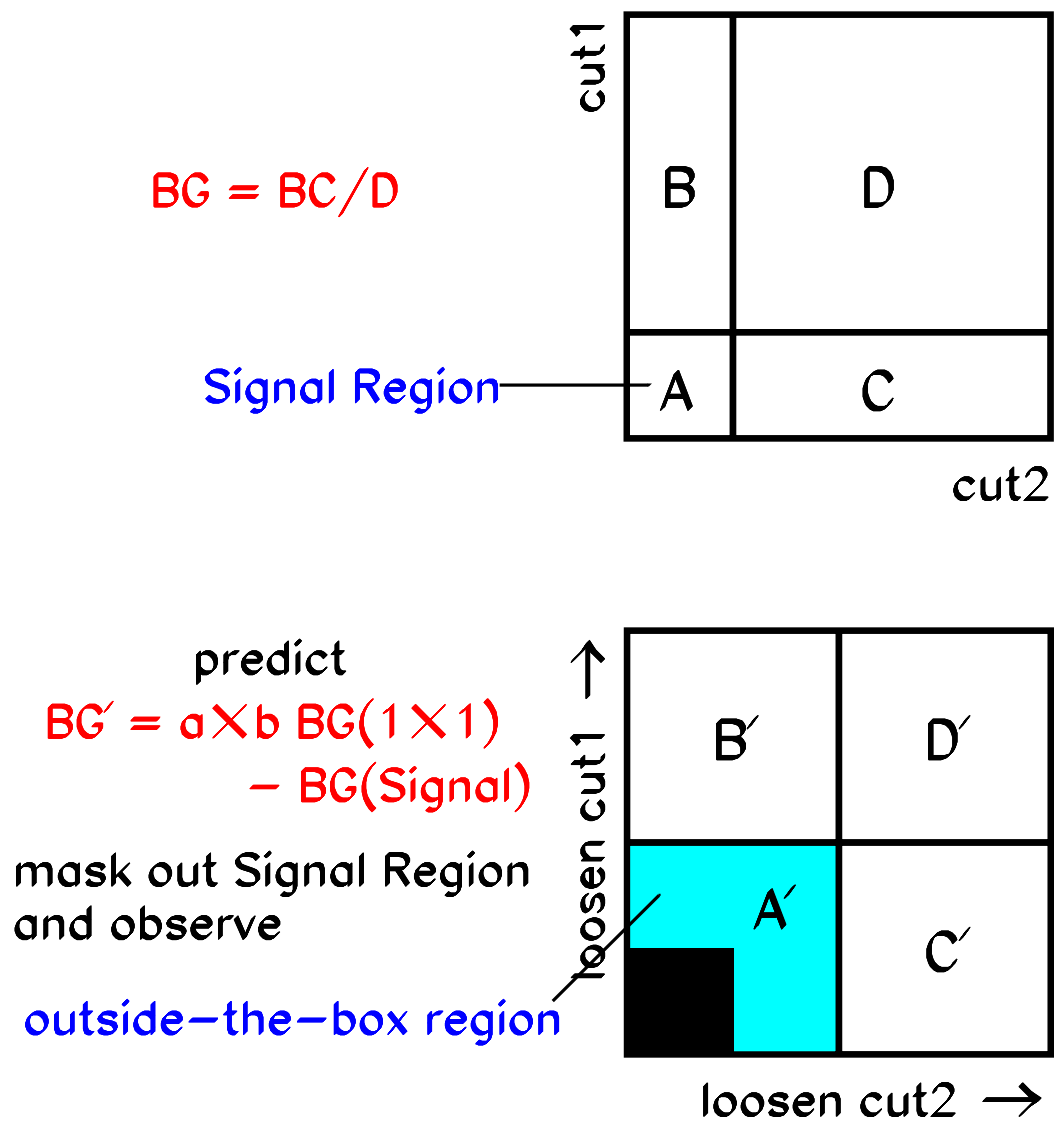


Figure 42: Pictorial explanation of the correlation study using the events near, but outside, the Signal Region.

$K_{\pi 2}$	(Photon Veto) \times ($K_{\pi 2}$ kinematics)				
	10 \times 10	20 \times 20	20 \times 50	50 \times 50	50 \times 100
	1.11 \pm 0.18 3	4.86 \pm 0.61 4	12.36 \pm 1.26 9	31.11 \pm 3.14 22	62.36 \pm 5.59 53
$K_{\mu 2}$ Range Tail	$(\pi^+ \rightarrow \mu^+ \rightarrow e^+) \times (K_{\mu 2} \text{ kinematics})$				
	10 \times 10	20 \times 20	50 \times 50	80 \times 50	120 \times 50
	0.35 \pm 0.03 0	1.44 \pm 0.10 1	9.07 \pm 0.62 12	14.52 \pm 0.99 16	21.78 \pm 1.48 25
μ^+ Band	$(\pi^+ \rightarrow \mu^+ \rightarrow e^+) \times (K_{\mu 2} \text{ kinematics})$				
	10 \times 10	20 \times 20	50 \times 20	80 \times 20	80 \times 40
	0.31 \pm 0.03 1	1.28 \pm 0.11 1	3.22 \pm 0.27 4	5.17 \pm 0.44 5	10.35 \pm 1.07 11

Table 12: Results of a correlation study for the $K_{\pi 2}$ (top), $K_{\mu 2}$ range tail (middle) and μ^+ band (bottom) backgrounds. The first row in each background represents the loosening factors of the bifurcation cuts; the second represents the predicted number of events in each outside-the-box region, which is obtained from Equation (39); and the third represents the number of observed events in each region. The errors in the predictions are statistical uncertainties.

where the values of N_{obs} and N_{pred} are arranged so as to be independent bin-to-bin. For example, $N(a' \times b') = n(a' \times b') - n(a \times b)$ where $a' \geq a$, $b' \geq b$ and $n(a \times b)$ is the total number of predicted or observed in events with loosening factors a and b . The uncertainty on N_{pred} for the $a' \times b'$ bin is taken as the difference in quadrature of the corresponding uncertainties in the table. The coefficient c is estimated by minimizing [6]

$$\chi^2 \equiv \sum_{i=1}^5 [2(cN_{\text{pred}}^i - N_{\text{obs}}^i) + 2N_{\text{obs}}^i \ln(N_{\text{obs}}^i / (cN_{\text{pred}}^i))], \quad (41)$$

where N_{obs}^i and N_{pred}^i are the observed and predicted contents of bin i , respectively. The results of the fit are summarized in Table 13.

Background	c	χ^2	χ^2 Probability
$K_{\pi 2}$	0.850 $^{+0.122+0.150}_{-0.112-0.111}$	6.486	0.166
$K_{\mu 2}$ range tail	1.148 $^{+0.245+0.156}_{-0.214-0.123}$	2.374	0.667
μ^+ band	1.063 $^{+0.353+0.210}_{-0.289-0.151}$	4.046	0.400

Table 13: Results of fits for the $K_{\pi 2}$, $K_{\mu 2}$ range tail and μ^+ band backgrounds. The first and second uncertainties on c are the statistical uncertainty in N_{obs} and the uncertainty due to N_{pred} , respectively.

The systematic uncertainty is taken as the variation in the c when N_{pred} is varied by its uncertainty. The value of c for each background source is consistent with unity and confirms that the background estimations via the Bifurcation Method are reliable.

In addition to the study of correlation between the cuts used for the Bifurcation Method, events that fail a single cut are examined to check if each cut operates as designed

for the appropriate background mechanism. Such a study is also a way to discover any new type of background. In the 1/3 sample, six of the eight events that failed a single cut were far from the cut position, while the other two events showed potential analysis flaws. The first flaw would artificially increase the measured range and momentum of π^+ s from $K_{\pi 2}$ decay that exited the upstream end of the target. Additional cuts with minimal acceptance loss were devised to eliminate such events. The second revealed a possible correlation between the photon veto and the π^+ dip angle that was subsequently eliminated with a relative acceptance loss of 0.96%. Examination of the 2/3 sample revealed that all of the 14 events that failed a single cut only were far from the cut position.

3.6.9 Summary of background

The final background levels are summarized in Table 14. The total background level in the signal region is estimated to be 0.297 ± 0.024 events, in which the $K_{\pi 2}$ background contribution is the largest (0.216 events). This total background level is relatively large given the expectation of a few candidate events; however, the expected background in the 1×1 region, which has 76% of the acceptance (Table 15, is only 15% of the total background. These differential background and acceptance levels in the signal region is exploited by using the likelihood technique described in Section 4.

Background	Background Level (event)	
	Signal Region	1×1 Region
$K_{\pi 2}$	0.216 ± 0.023	0.019 ± 0.005
$K_{\mu 2}$	0.068 ± 0.006	0.015 ± 0.001
Beam	0.013 ± 0.003	0.011 ± 0.003
Total	0.297 ± 0.024	0.045 ± 0.006

Table 14: Total background level and the contribution from each background source. The errors are statistical.

3.7 Examining the signal region

When the final background analysis is completed, all the selection criteria are applied to the data. One candidate event is observed near the upper kinematic limit for $K^+ \rightarrow \pi^+ \nu \bar{\nu}$ decay. Figure 43 shows the range and kinetic energy of the events that pass all of the selection criteria, except for the phase space cuts on both the range and energy. Checking the information for the target, UTC and RS shows no obvious mistake in the reconstruction as displayed in Figure 44. No other beam particle coincident with the track time is detected in the beam instrumentation. No activity is detected at the track time in the photon detectors. The charged track of the candidate event has a momentum of 227.3 MeV/c, a kinetic energy of 128.9 MeV and a range of 39.2 cm. The momentum, kinetic energy and range distributions $K_{\pi 2}$ monitor events are also checked in the run that contains the candidate event. The corresponding peak positions and resolutions are all located at the expected positions. Kinematically, this candidate event agrees with all the requirements

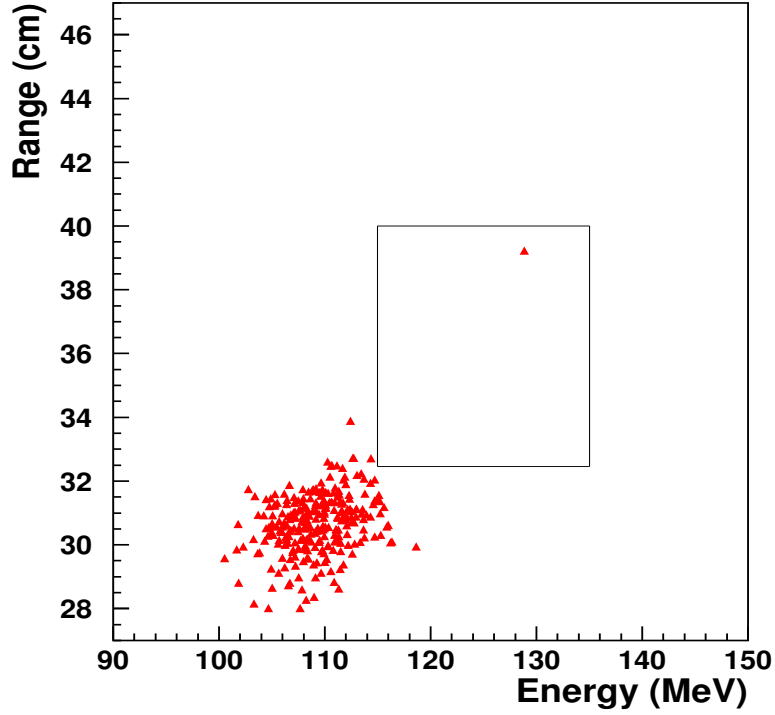


Figure 43: Range vs kinetic energy of the events satisfying all of the cuts, except for the phase space cuts on both the range and energy. The rectangle represents the signal region in the range vs energy plane. Events around $E = 110$ MeV/c are due to $K_{\pi 2}$, which are not removed by the photon veto cuts.

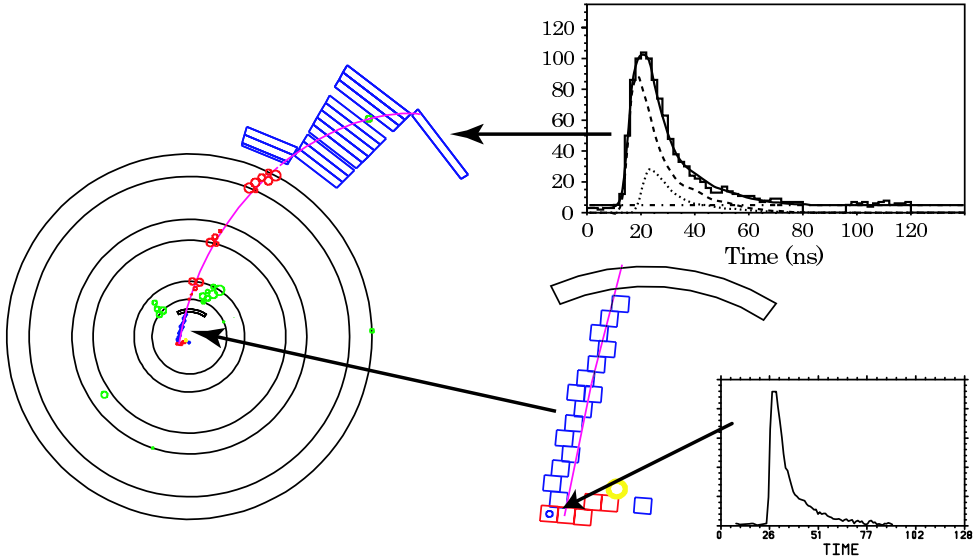


Figure 44: Reconstruction of the candidate event (end view). The TD data in the π^+ stopping counter and the reconstruction in the target are also displayed.

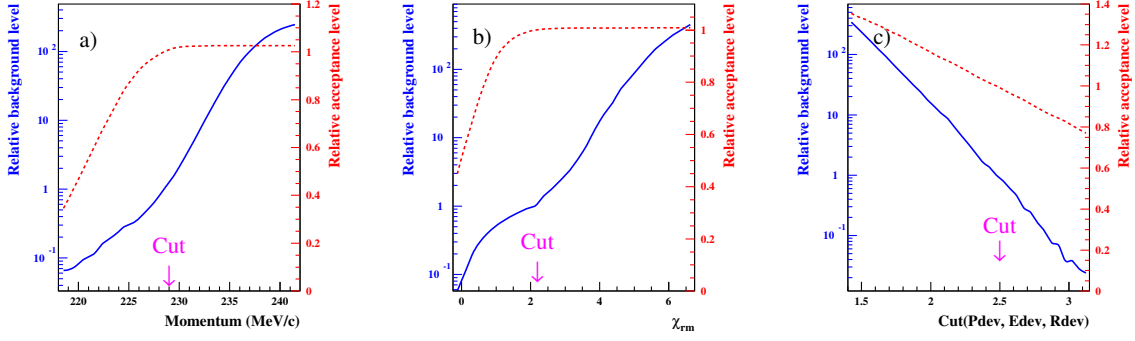


Figure 45: Background and acceptance functions related to the kinematics of the $K_{\mu 2}$ range tail a) the μ^+ band b) and the $K_{\pi 2}$ background c). The relative background levels are shown in the solid curves, while the relative acceptance are shown in the dashed curves. They are all normalized to the standard cut positions as indicated in the plots.)

as a signal, though it exists in a relatively small acceptance region. All the other selection criteria are also checked. No evidence indicates that this candidate event like a junk or show up through a loop hole.

3.8 Background distributions inside the signal region

Since the background distribution is not uniform in the signal region, an observed candidate can have different possibility being a background event. Therefore, it is necessary to make full use of the knowledge obtained in the background analysis and construct the so-called background functions.

3.8.1 $K_{\mu 2}$ and $K_{\pi 2}$ background functions

Because the $K_{\mu 2}$ background contributes to the signal region via two ways. When the momentum is greater than 220 MeV/c, it is thought to be through momentum resolution effect. Otherwise it is through the range-momentum resolution effect. The background level for both $K_{\mu 2}$ range tail and μ^+ band events are studied using the $pnn1$ trigger data. The acceptance loss due to the momentum cut is estimated using Monte Carlo simulation, which can give a reliable result in term of momentum resolution effect. The π^+ scattering events in the $pnn1$ trigger are directly used to give the evaluation of acceptance loss due to the range-momentum cut. Because the $K_{\pi 2}$ background contribute to the signal purely through the resolution effect, the background function is constructed with respect to the energy, momentum and range cuts positions. The $K_{\pi 2}$ events in the $pnn1$ trigger data are used to measure this effect, while the Monte Carlo $K^+ \rightarrow \pi^+ \nu \bar{\nu}$ events are used to give the estimate of the corresponding acceptance loss. Figure 45 show the relative $K_{\mu 2}$ and $K_{\pi 2}$ background levels varying with the cut positions. Also shown are the corresponding relative acceptance changes.

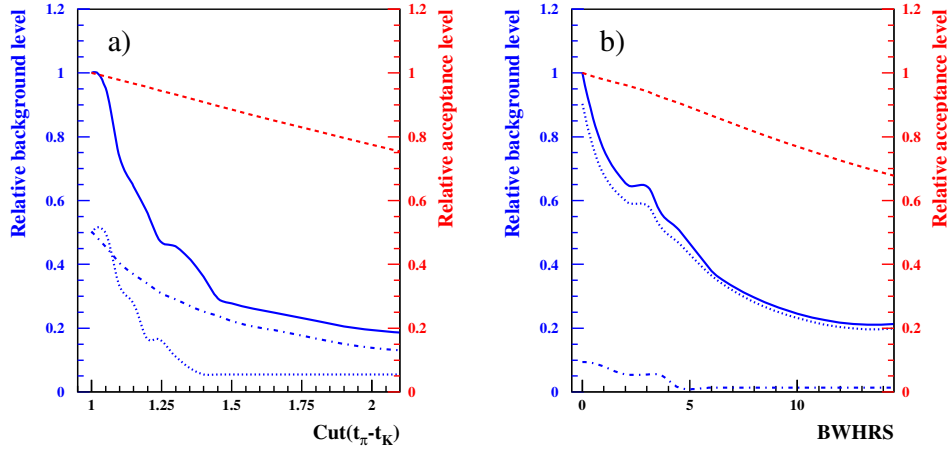


Figure 46: Background functions for the single beam background a) and the double beam background b). The relative background level variations are shown in solid curves, while the relative acceptance level changes are shown in dashed curves. For the single beam background, the component for the K^+/π^+ single beam and the CEX background are shown in dotted-dashed and dotted curves, respectively. For the double beam background, the dotted-dashed and dotted curves represent for the $K^+ - K^+$ and $K^+ - \pi^+$ contributions separately.

3.8.2 Beam background functions

Single beam and double beam functions are constructed with respect to the delayed coincidence cut and the BWPCs timing cut separately. The *pnn1* trigger data are used to give the background distribution for the K^+/π^+ single beam, while the CEX background distribution is from the Monte Carlo simulation. Since the CEX background event also belongs to the single beam, it is added in the single beam background. The acceptance is measured with the stopped K^+ events in the $K_{\mu 2}$ monitor trigger. Similar as the single beam background, the double beam background distribution also comes from the *pnn1* trigger data. The acceptances are measured with the single K^+ beam events in the $K_{\mu 2}$ monitor trigger. Since the double beam background includes both the $K^+ - K^+$ and $K^+ - \pi^+$ events, the background functions are also given separately. Figure 45 show the relative single and double beam background levels varying with the cut positions. Also shown are the corresponding relative acceptance changes.

3.9 Acceptance measurement and sensitivity

In this analysis, except for the acceptances of phase space and most of the trigger conditions, all the rest are measured using the monitor trigger data. The single event sensitivity will be defined as the inverse product of the total number of K^+ 's stop in the target multiplying the acceptance.

3.9.1 Acceptance measurements

The acceptances of the $K^+ \rightarrow \pi^+ \nu \bar{\nu}$ decay can be split into several parts as already tabulated in Table 15. The acceptance evaluations are done separately. The motivation is to give an unbiased estimate by all means, since there are so many cuts being applied in this analysis, and it is not so easy to simulate all the physics processes and the experimental conditions. The signature of the $K_{\mu 2}$ decay (a single charged track and no other activities from the K^+ decay) is the same as that of the $K^+ \rightarrow \pi^+ \nu \bar{\nu}$ signals. $K_{\mu 2}$ events are therefore suitably used to measure the charged-track reconstruction efficiency, the beam and target analysis acceptances, and the accidental loss due to both the online and offline photon veto cuts. The $K_{\pi 2}$ decay, on the other hand, is suitably used for calculating the acceptances of the target reconstruction cuts. The π^+ scattering events provide the π^+ tracks whose stopping layer spreads throughout the RS. They are useful to measure the acceptances of the kinematic constraints on π^+ tracks, including the RS dE/dx cuts, track reconstruction in the UTC and RS, as well as the $\pi^+ \rightarrow \mu^+ \rightarrow e^+$ decay sequence. The trigger acceptance, the phase-space and solid-angle acceptances, and the acceptance loss due to π^+ nuclear interactions and decay-in-flights are obtained by using Monte Carlo simulations of the $K^+ \rightarrow \pi^+ \nu \bar{\nu}$ decay, because they are related to the $K^+ \rightarrow \pi^+ \nu \bar{\nu}$ kinematics and can not be measured by using any monitor trigger data. There are other acceptance factors: one is the T·2 efficiency, where T·2 is the trigger bit that requires a coincident hit in the first two layers of the RS counters. The definition is explained in Section 2.8, and the another is the K^+ stop efficiency. The T·2 efficiency accounts for the efficiency of the trigger counter in the RS (i.e., the T-Counter). The acceptance loss due to the counter inefficiency and the geometrical inefficiency (which is due to azimuthal gaps between sectors) is estimated using both $K_{\pi 2}$ and $K_{\mu 2}$ events. Since the number of incoming K^+ 's are counted by the beam counters, some of them, however, may decay before entering into the target or pass through the target without stopping, one must correct this effect on the total number K^+ exposures. The K^+ stop efficiency is the fraction of K^+ 's stopping in the target to those entering the target and satisfying the KB requirement. $K_{\mu 2}$ decay is used for this measurement because the signature of $K_{\mu 2}$ events is similar to that of $K^+ \rightarrow \pi^+ \nu \bar{\nu}$. The K^+ stop efficiency is measured to be $0.7740 \pm 0.0011(stat.)$. The acceptances of the $K^+ \rightarrow \pi^+ \nu \bar{\nu}$ signal selection cuts are summarized in Table 15.

3.9.2 $K_{\pi 2}$ branching ratio measurement

Measurement of the $K_{\pi 2}$ branching ratio can be used to confirm the correctness in evaluating the acceptances of the $K^+ \rightarrow \pi^+ \nu \bar{\nu}$ selection cuts. Stopped $K_{\pi 2}$ events are selected from the $K_{\pi 2}$ monitor trigger data by imposing the cuts similar to the $K^+ \rightarrow \pi^+ \nu \bar{\nu}$ selection criteria except for those used for the photon veto and for defining the kinematic signal region. Good $K_{\pi 2}$ events also satisfy the requirements on the energy, momentum and range, which are defined to be within the $\pm 3\sigma$ region of the $K_{\pi 2}$ peaks. The acceptance of the $K_{\pi 2}$ mode is estimated in the same way as that of the $K^+ \rightarrow \pi^+ \nu \bar{\nu}$ mode. Figure 47 shows the variation of $K_{\pi 2}$ branching ratio as a function of run. A stable branching ratio is observed. The $K_{\pi 2}$ branching ratio is measured to be $\mathcal{B}(K_{\pi 2}) = 0.2190 \pm 0.0050(stat.)$. This value agrees with the PDG value 0.212 ± 0.001 within 3.3%, which give us confidence that the acceptance measurements are correct.

Factor	Acceptance	Sample source
Trigger acceptance	$0.1796 \pm 0.0010 \pm 0.0090$	MC
K^+ stop efficiency	0.7740 ± 0.0011	$K_{\mu 2}$
Beam and target analysis	0.5483 ± 0.0007	$K_{\mu 2}$
Phase space and solid angle	0.4020 ± 0.0030	MC
π^+ nucl. int. and decay-in-flight	$0.4953 \pm 0.0077 \pm 0.0248$	MC
Reconstruction efficiency	0.9956 ± 0.0001	$K_{\mu 2}$
Other kinematics constraints	$0.5013 \pm 0.0071 \pm 0.0154$	$\pi_{scatter}$
$\pi^+ \rightarrow \mu^+ \rightarrow e^+$ decay acceptance	$0.3914 \pm 0.0085 \pm 0.0074$	$\pi_{scatter}$
Accidental loss	0.8204 ± 0.0019	$K_{\mu 2}$
T-2 efficiency	$0.9357 \pm 0.0011 \pm 0.0168$	$K_{\mu 2}, K_{\pi 2}$
Total acceptance	$(2.22 \pm 0.07 \pm 0.18) \times 10^{-3}$	

Table 15: Acceptances for the $K^+ \rightarrow \pi^+ \nu \bar{\nu}$ analysis.

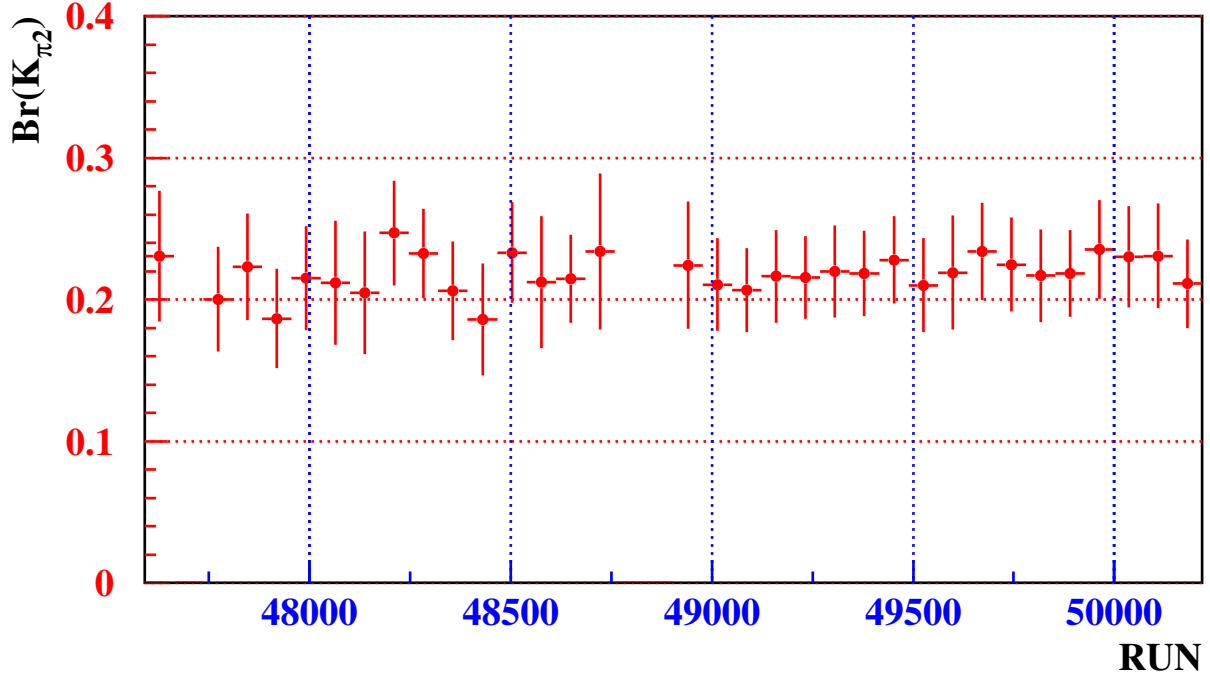


Figure 47: Measurement of the $K^+ \rightarrow \pi^+ \pi^0$ branching ratio as a function of run number in E949.

3.9.3 Summary of acceptance and sensitivity

Once the acceptances of the $K^+ \rightarrow \pi^+ \nu \bar{\nu}$ selection cuts are measured, the sensitivity for the $K^+ \rightarrow \pi^+ \nu \bar{\nu}$ analysis in E949 is calculated. In the physics run of the E949 the number of the K^+ triggers for $K^+ \rightarrow \pi^+ \nu \bar{\nu}$ was 1.77×10^{12} . By using the measured total acceptance of $0.00222 \pm 0.00007(stat.) \pm 0.00015(sys.)$, the sensitivity of the E949 2002 run is calculated to be $(2.55 \pm 0.08 \pm 0.18) \times 10^{-10}$, where the first and second uncertainties represent the statistical and systematic uncertainties, respectively.

Function	Bin	$N(BG)$
$K_{\pi 2}$ kinematics	$0.0 \leq N_{K\pi 2} < 0.2$	0.00
PV	$0.1 < N_{PV} < 0.2$	0.11
Muon Band	$0.0 < N_{Band} < 0.5$	0.29
$K_{\mu 2}$ Range Tail	$0.4 < N_{Tail} < 0.6$	0.51
$\pi^+ \rightarrow \mu^+ \rightarrow e^+$	$1.0 < N_{\pi \rightarrow \mu \rightarrow e} < 1.5$	1.23
1-Beam	$0.0 \leq N_{1beam} < 0.2$	0.00
2-Beam	$0.0 \leq N_{2beam} < 0.2$	0.00

Table 16: Bin in each background function (2nd column) and relative background level (3rd column) for the candidate event.

Source	Background Level (event)
$K_{\pi 2}$	0.029×10^{-5}
Muon	5.632×10^{-5}
(Muon Band)	(0.715×10^{-5})
($K_{\mu 2}$ Range Tail)	(4.917×10^{-5})
1 Beam (including CEX)	0.058×10^{-5}
2 Beam	0.026×10^{-5}
Total Background b_i	5.745×10^{-5}
Relative Cell Acceptance A_i	1.210×10^{-4}

Table 17: Contribution of each background source to the background level in the cell for the candidate event. Each background level is represented as the number of events. The ratio of the acceptance in the cell to the total acceptance in the 1×1 region is also tabulated in this table.

4 Branching ratio of $K^+ \rightarrow \pi^+ \nu \bar{\nu}$

In this section, we will present how to extract the branching ratio of $K^+ \rightarrow \pi^+ \nu \bar{\nu}$ based on our knowledge for the background distribution in the single box. This can give a proper weight in determining the branching ratio.

4.1 Signal/noise cell definitions and likelihood estimator

The $K^+ \rightarrow \pi^+ \nu \bar{\nu}$ branching ratio is measured via a likelihood analysis. All of the cells inside the signal region are pre-determined before an examination of the signal region. The cell for the candidate event is defined by the bins in the functions, as shown in Table 16. The background levels of all the background sources in this cell are summarized in Table 17. The largest contribution to the total background level in this cell (5.745×10^{-5} events) is the $K_{\mu 2}$ Range Tail background (4.917×10^{-5} events). The ratio of the acceptance in this cell to the total acceptance in the 1×1 region ($A_{total}^{1 \times 1} = 0.001694$) is estimated to be 1.21×10^{-4} . The expected number of signal events in this cell is therefore

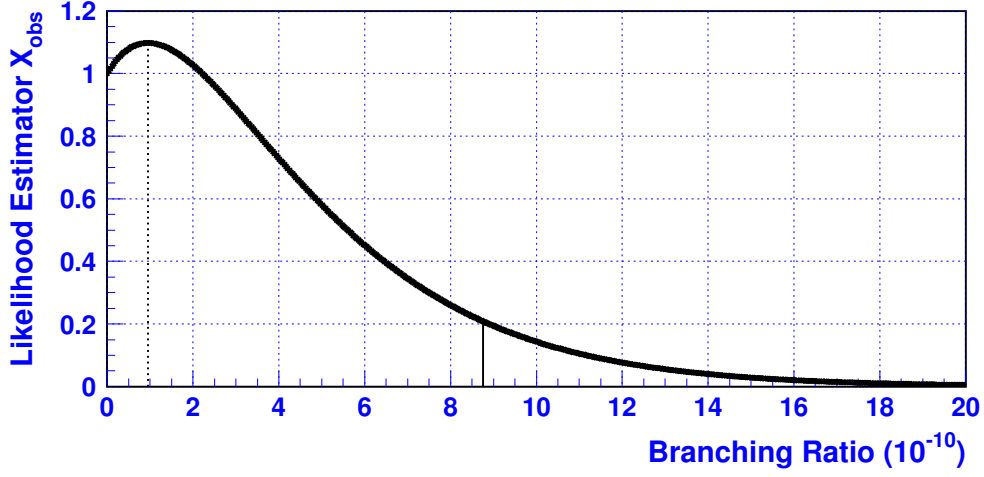


Figure 48: Likelihood estimator, X_{obs} , for the E949 2002 data set as a function of the $K^+ \rightarrow \pi^+ \nu \bar{\nu}$ branching ratio, \mathcal{B} .

calculated as

$$\begin{aligned}
 s_i &= N_K \cdot \mathcal{B} \cdot A_{total}^{1 \times 1} \cdot A_i \\
 &= 1.770 \times 10^{12} \cdot \mathcal{B} \cdot 0.001694 \cdot 1.21 \times 10^{-4} \\
 &= 3.628 \times 10^5 \cdot \mathcal{B},
 \end{aligned} \tag{42}$$

where \mathcal{B} represents the $K^+ \rightarrow \pi^+ \nu \bar{\nu}$ branching ratio and N_K is the number of K^+ triggers for $K^+ \rightarrow \pi^+ \nu \bar{\nu}$. With these expected number and background level in the candidate event cell, the likelihood estimator, X :

$$X \equiv \prod_{i=1}^n X_i, \quad \text{with} \quad X_i = \frac{e^{-(s_i+b_i)}(s_i+b_i)^{d_i}}{d_i!} / \frac{e^{-b_i}(b_i)^{d_i}}{d_i!} = e^{-s_i} \left(1 + \frac{s_i}{b_i}\right)^{d_i} \tag{43}$$

gives the central value of the $K^+ \rightarrow \pi^+ \nu \bar{\nu}$ branching ratio when the likelihood estimator with the given configuration of $\{s_i\}$, $\{b_i\}$ and $\{d_i\}$ (referred to as X_{obs}) gives the maximum value.

4.2 Branching ratio of $K^+ \rightarrow \pi^+ \nu \bar{\nu}$

Figure 48 shows the likelihood estimator, X_{obs} , as a function of the $K^+ \rightarrow \pi^+ \nu \bar{\nu}$ branching ratio, \mathcal{B} . This plot indicates that, even though X_{obs} has the maximum value at $\mathcal{B} = 0.96 \times 10^{-10}$, the case that $\mathcal{B} = 0$ is not necessarily ruled out because the candidate event observed in the E949 data has a small signal-to-background ratio. An upper limit for $\mathcal{B}(K^+ \rightarrow \pi^+ \nu \bar{\nu})$ is calculated with a Bayesian approach. Assuming that $X_{obs}(\mathcal{B})$ represents the probability density function for the branching ratio, one can have the probability to obtain a branching ratio, \mathcal{B} , with a given X_{obs} as follow

$$P(\mathcal{B}|X_{obs}) = \frac{X_{obs}(\mathcal{B})S(\mathcal{B})}{\int_{-\infty}^{+\infty} X_{obs}(\mathcal{B})S(\mathcal{B})d\mathcal{B}}, \tag{44}$$

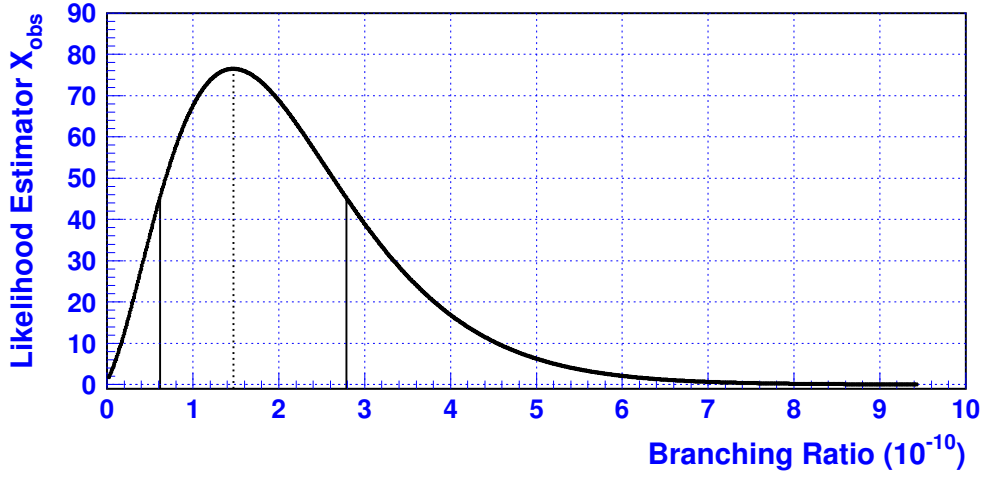


Figure 49: Likelihood estimator, X_{obs} , for the combined E787 and E949 results as a function of the $K^+ \rightarrow \pi^+ \nu \bar{\nu}$ branching ratio, \mathcal{B} .

where $S(\mathcal{B}) = 1$ when $\mathcal{B} \geq 0$ and $S(\mathcal{B}) = 0$ when $\mathcal{B} < 0$. The confidence level $(1 - \alpha)$ is calculated as

$$1 - \alpha = \int_{-\infty}^{\mathcal{B}_0} P(\mathcal{B}|X_{obs})d\mathcal{B} = \frac{\int_0^{\mathcal{B}_0} X_{obs}(\mathcal{B})d\mathcal{B}}{\int_0^{+\infty} X_{obs}(\mathcal{B})d\mathcal{B}}. \quad (45)$$

With Equations (44) and (45), an upper limit for $\mathcal{B}(K^+ \rightarrow \pi^+ \nu \bar{\nu})$ at the 90% confidence level (CL) is obtained as

$$\mathcal{B}(K^+ \rightarrow \pi^+ \nu \bar{\nu}) < 8.76 \times 10^{-10} \quad (90\% \text{ CL}) \quad (46)$$

based on the single candidate event. This limit is consistent with the previous results from E787.

The results from both E787 and E949 are combined to calculate the branching ratio for $K^+ \rightarrow \pi^+ \nu \bar{\nu}$. In the E787 $K^+ \rightarrow \pi^+ \nu \bar{\nu}$ analysis, two $K^+ \rightarrow \pi^+ \nu \bar{\nu}$ candidate events were observed in the signal region [23, 24]. Since all of the measurements (background and acceptance functions, background levels, sensitivity, etc.) of E787 and E949 were performed independently, what should be done for combining both results is to evaluate the likelihood estimator, X_{obs} , from all of the sets of $\{s_i\}$, $\{b_i\}$, and $\{d_i\}$ for both results. For the E949 data set, the signal region is divided into 3781 cells, while the E787 signal region has 488 cells. Figure 49 shows the likelihood estimator, X_{obs} , for the combined E787 and E949 results as a function of the $K^+ \rightarrow \pi^+ \nu \bar{\nu}$ branching ratio, \mathcal{B} . X_{obs} has the maximum value at $\mathcal{B} = 1.47 \times 10^{-10}$, and the case that $\mathcal{B} = 0$ is unlikely. By using Equation (44), a confidence level interval $(1 - \alpha)$ is calculated so that the probability that the true value of the branching ratio is included between \mathcal{B}_1 and \mathcal{B}_2 ($0 < \mathcal{B}_1 < \mathcal{B}_2$) is

$$1 - \alpha = \int_{\mathcal{B}_1}^{\mathcal{B}_2} P(\mathcal{B}|X_{obs})d\mathcal{B} = \frac{\int_{\mathcal{B}_1}^{\mathcal{B}_2} X_{obs}(\mathcal{B})d\mathcal{B}}{\int_0^{+\infty} X_{obs}(\mathcal{B})d\mathcal{B}}, \quad \text{where } X_{obs}(\mathcal{B}_1) = X_{obs}(\mathcal{B}_2). \quad (47)$$

The $K^+ \rightarrow \pi^+ \nu \bar{\nu}$ branching ratio at the 68% CL interval is obtained as

$$\mathcal{B}(K^+ \rightarrow \pi^+ \nu \bar{\nu}) = (1.47_{-0.86}^{+1.32}) \times 10^{-10} \quad (68\% \text{ CL interval}) \quad (48)$$

CL interval	Branching Ratio
68%	$[0.61, 2.79] \times 10^{-10}$
80%	$[0.45, 3.25] \times 10^{-10}$
90%	$[0.29, 3.90] \times 10^{-10}$
95%	$[0.17, 4.53] \times 10^{-10}$

Table 18: $K^+ \rightarrow \pi^+ \nu \bar{\nu}$ branching ratios at the 68%, 80%, 90%, 95% confidence level intervals.

	E787		E949
Candidate	1995A	1998C	2002A
s_i/b_i	50	7	0.9
$W_i \equiv s_i/(s_i + b_i)$	0.98	0.88	0.48
Background Prob.	0.006	0.02	0.07

Table 19: Signal to background ratio (s_i/b_i), signal weight ($W_i \equiv s_i/(s_i + b_i)$), and probability that the background alone gives rise to the candidate event ($1 - CL_b$) for each candidate event. The first and second candidate events in E787 and the E949 candidate event are called 1995A, 1998C and 2002A, respectively.

based on three candidate events. This measured branching ratio takes only the statistical uncertainty into account. This value is consistent with the SM prediction, although the central value is twice as large as the SM prediction. The $K^+ \rightarrow \pi^+ \nu \bar{\nu}$ branching ratios at several confidence level intervals are summarized in Table 18.

The signal-to-background ratio (s_i/b_i) and the signal weight ($W_i \equiv s_i/(s_i + b_i)$) for each candidate event are summarized in Table 19. The value of s_i for each candidate event is calculated based on the central value of the measured branching ratio, 1.47×10^{-10} . The signal-to-background ratio for the E949 candidate event is 0.9. The probability that the background alone gives rise to the E949 candidate event, or a more signal-like configuration, is 0.074; this value is not small, because the candidate event is observed in a region with a relatively small acceptance and a large background. On the other hand, the probability that the background alone gives rise to the three candidate events, or a more signal-like configuration, is 0.001.

4.3 Estimation of systematic uncertainty

Since the branching-ratio calculation depends on the magnitudes of the expected signal events and the background levels in the candidate event cells, the uncertainties concerning the sensitivity and background levels would affect the branching ratio. In Section 3.6.8, the correlation between the two Bifurcation cuts in each background source is considered, and the quantity that represents the consistency between the predicted and observed b backgrounds outside the Signal Region (the value c) is estimated. The magnitudes for the assumed systematic uncertainties are based on the uncertainties concerning the value c in Table 13; from the table, the uncertainty on each background source was estimated to be 20%. From the sensitivity calculation explained in Chapter 3.9, the uncertainty on

Source	68% CL interval (10^{-10})		
	$+1\sigma$	-1σ	relative error
No systematic	[0.615, 2.786]		
$K_{\pi 2}$	[0.614, 2.785]	[0.616, 2.787]	+0.043% -0.163%
$K_{\mu 2}$ Range Tail	[0.595, 2.749]	[0.639, 2.829]	+1.533% -3.270%
Muon Band	[0.611, 2.780]	[0.619, 2.792]	+0.226% -0.602%
1 Beam	[0.599, 2.768]	[0.631, 2.804]	+0.646% -2.587%
2 Beam	[0.614, 2.785]	[0.615, 2.786]	+0.007% -0.098%
Sensitivity	[0.676, 3.065]	[0.553, 2.507]	+10.00% -10.00%
Total			+10.14% -10.85%

Table 20: 68% CL intervals with $\pm 1\sigma$ variations of the background levels and the sensitivity. The 2nd and 3rd columns represent the 68% CL intervals with $+1\sigma$ and -1σ variations of each source, respectively. The top and bottom values in the 4th column represent the relative uncertainties with respect to the upper (2.786) and lower (0.615) bounds of the 68% CL interval, respectively.

the sensitivity was estimated to be 10%. These magnitudes concerning the uncertainties are regarded as being one standard-deviation (1σ) of their systematic uncertainties. The differences in the lower and upper boundaries of the 68% CL interval when the background levels and the sensitivity are varied by $\pm 1\sigma$ are treated as a systematic uncertainty. Table 20 summarizes the 68% CL intervals at $\pm 1\sigma$ variations of the background levels and the sensitivity; the main contribution to the systematic uncertainty on the 68% CL intervals is the uncertainty concerning the sensitivity. The systematic uncertainty on the branching ratio is obtained by summing the quadrature of the relative uncertainties, assuming that the uncertainties are not correlated. The systematic uncertainties on the upper and lower bounds (2.786 and 0.615) of the 68% CL interval are estimated to be +10.14% and -10.85%, respectively. The branching ratio at the 68% CL interval is therefore estimated to be

$$\mathcal{B}(K^+ \rightarrow \pi^+ \nu \bar{\nu}) = (1.47_{-0.86}^{+1.32}(\text{stat})_{-0.07}^{+0.28}(\text{sys})) \times 10^{-10} \quad (49)$$

$$= (1.47_{-0.93}^{+1.60}) \times 10^{-10}, \quad (50)$$

where the first and second uncertainties in (49) represent the statistical and systematic uncertainties, respectively, and the uncertainty in (50) represents the sum of the statistical and systematic uncertainties [57].

4.4 Implication for $BR(K^+ \rightarrow \pi^+ X^0)$

The experimental signature of a $K^+ \rightarrow \pi^+ X^0$ event is the same as that of a $K^+ \rightarrow \pi^+ \nu \bar{\nu}$ event except that the kinematic values of π^+ are monochromatic ($P = 227.1$ MeV, $E = 127.0$ MeV, $R = 38.6$ cm). The same analysis method as used in the $K^+ \rightarrow \pi^+ \nu \bar{\nu}$ analysis is used to search for $K^+ \rightarrow \pi^+ X^0$ except for the Phase Space Cuts (and the acceptance factors for it).

The signal region for the $K^+ \rightarrow \pi^+ X^0$ is the same as the $K^+ \rightarrow \pi^+ \nu \bar{\nu}$ except that the Phase Space Cuts are $\pm 2\sigma$ regions of momentum, energy, range peaks. The upper edges of the Phase Space Cuts are tightened ($P \leq 229$ MeV/c, $E \leq 135$ MeV, and $R \leq 40$ cm as in $K^+ \rightarrow \pi^+ \nu \bar{\nu}$) so that the Muon background can be suppressed. The expected background level is small (0.05 events), because the region is far from the $K_{\pi 2}$ peaks.

The candidate event observed in the signal region for $K^+ \rightarrow \pi^+ \nu \bar{\nu}$ is also in the $K^+ \rightarrow \pi^+ X^0$ signal region; the candidate event is not exactly identified as $K^+ \rightarrow \pi^+ X^0$ signal, and only the upper limit is set with the assumption that the background is absent.

All the acceptance studies for the $K^+ \rightarrow \pi^+ X^0$ decay mode are exactly the same as those for the $K^+ \rightarrow \pi^+ \nu \bar{\nu}$ decay mode. The total acceptance and sensitivity for the $K^+ \rightarrow \pi^+ X^0$ analysis are measured to be $(6.89 \pm 0.20 \pm 0.52) \times 10^{-3}$ and $(0.82 \pm 0.02 \pm 0.06) \times 10^{-10}$, where the first and second errors are the statistical and systematic uncertainties. It is noted that the acceptance for the $K^+ \rightarrow \pi^+ X^0$ decay mode is higher than the $K^+ \rightarrow \pi^+ \nu \bar{\nu}$ decay mode. This is completely due to the phase space effect.

There was no candidate event in the $K^+ \rightarrow \pi^+ X^0$ signal region of E787. The combined E787 and E949 sensitivity of 0.196×10^{-10} and the Feldman and Cousins method [60] in the assumption of one signal event and no background give the upper limit for the $K^+ \rightarrow \pi^+ X^0$ decay as:

$$\mathcal{B}(K^+ \rightarrow \pi^+ X^0) < 3.81 \times 0.196 \times 10^{-10} = 0.747 \times 10^{-10} \quad (51)$$

at 90% confidence level. This limit is larger than the previous limit 0.59×10^{-10} (90% CL) from the E787 result [23, 24] due to one candidate event in E949.

4.5 Impact of $K^+ \rightarrow \pi^+ \nu \bar{\nu}$ branching ratio on unitarity triangle

The $K^+ \rightarrow \pi^+ \nu \bar{\nu}$ branching ratio constrains the CKM matrix element, $|V_{td}|$. The quantity that is directly extracted from $\mathcal{B}(K^+ \rightarrow \pi^+ \nu \bar{\nu})$ is $|\lambda_t| \equiv |V_{ts}^* V_{td}|$. To extract $|V_{td}|$, $|\lambda_t|$ should be divided by $|V_{cb}| \simeq |V_{ts}|$. Since $|V_{cb}|$ should be measured from B decays, the quantity $|\lambda_t|$ is extracted in order to perform an independent measurement from B decays. $|V_{td}|$ is extracted by dividing $|\lambda_t|$ by $|V_{cb}|$.

Equation (9) can be written as

$$\mathcal{B}_{\pi^+ \nu \bar{\nu}} = \xi \left[(\text{Im} \lambda_t X_t)^2 + (\lambda_c \bar{X} + \text{Re} \lambda_t X_t)^2 \right], \quad (52)$$

where

$$\xi \equiv \frac{3\alpha^2 \mathcal{B}(K^+ \rightarrow \pi^0 e^+ \nu)}{|V_{us}|^2 2\pi^2 \sin \Theta_W^4}, \quad \bar{X} \equiv \lambda^4 P_c(X) = \frac{1}{3}(2X_{\text{NL}}^e + X_{\text{NL}}^\tau), \quad \text{and} \quad X_t \equiv X(x_t). \quad (53)$$

From the upper limit of $\mathcal{B}(K^+ \rightarrow \pi^+ \nu \bar{\nu})$ the above equation has the relation

$$\mathcal{B}_{\pi^+ \nu \bar{\nu}}^{\text{MAX}} \geq \xi \left[(\text{Im} \lambda_t X_t)^2 + (\lambda_c \bar{X} + \text{Re} \lambda_t X_t)^2 \right]. \quad (54)$$

Assuming the extreme case that the second term equals zero (i.e., real parts of the charm and top contributions cancel each other exactly), one obtains the following relations:

$$\begin{aligned} \mathcal{B}_{\pi^+ \nu \bar{\nu}}^{\text{MAX}} &> \xi (\text{Im} \lambda_t X_t)^2, \\ |\text{Im} \lambda_t X_t| &< \sqrt{\mathcal{B}_{\pi^+ \nu \bar{\nu}}^{\text{MAX}} / \xi}. \end{aligned} \quad (55)$$

Using $\xi = 1.5226 \times 10^{-4}$ and the measured branching ratio at the 68% CL interval, $\mathcal{B}_{\pi^+\nu\bar{\nu}}^{MAX} = 3.07 \times 10^{-10}$. All of the values of the branching ratio used in this calculation include the systematic uncertainty. Taking $m_t = 168.1$ GeV to give $X_t = 1.529$, one can get $|\text{Im}\lambda_t| < 0.928 \times 10^{-3}$ from Equation (55).

The limits on the real part of λ_t can be set by assuming the extreme case that the imaginary part of λ_t is equal to zero.

$$\begin{aligned}\mathcal{B}_{\pi^+\nu\bar{\nu}}^{MAX} &> \xi (\lambda_c \bar{X} + \text{Re}\lambda_t X_t)^2 \\ |\lambda_c \bar{X} + \text{Re}\lambda_t X_t| &< \sqrt{\mathcal{B}_{\pi^+\nu\bar{\nu}}^{MAX}/\xi}.\end{aligned}\tag{56}$$

Since λ_c is negative,

$$\text{Re}\lambda_t X_t < \sqrt{\mathcal{B}_{\pi^+\nu\bar{\nu}}^{MAX}/\xi} + |\lambda_c \bar{X}|,\tag{57}$$

$$\text{Re}\lambda_t X_t > -\sqrt{\mathcal{B}_{\pi^+\nu\bar{\nu}}^{MAX}/\xi} + |\lambda_c \bar{X}|.\tag{58}$$

\bar{X} has a large uncertainty and depends on the charm quark mass, m_c , the scale factor, $\mu_c = \mathcal{O}(m_c)$, and the coupling constant, $\alpha_s(M_Z^2)$. Maximizing \bar{X} ($= 1.098 \times 10^{-3}$) in Equation (57) gives $\text{Re}\lambda_t < 1.085 \times 10^{-3}$. Minimizing \bar{X} ($= 0.761 \times 10^{-3}$) in Equation (58) gives $\text{Re}\lambda_t > -0.8197 \times 10^{-3}$. Note that the limit given in Equation (57) is also a limit on $|\lambda_t X_t|$, because, for a given $\mathcal{B}_{\pi^+\nu\bar{\nu}}$, $|\lambda_t|$ is maximum when it is real and directed opposite to $\lambda_c \bar{X}$.

From the lower limit of $\mathcal{B}(K^+ \rightarrow \pi^+ \nu \bar{\nu})$ we obtain

$$\begin{aligned}\mathcal{B}_{\pi^+\nu\bar{\nu}}^{MIN} &< \xi |\lambda_c \bar{X} + \lambda_t X_t|^2, \\ \sqrt{\mathcal{B}_{\pi^+\nu\bar{\nu}}^{MIN}/\xi} &< |\lambda_c \bar{X} + \lambda_t X_t| \\ &< |\lambda_c \bar{X}| + |\lambda_t X_t|, \\ \sqrt{\mathcal{B}_{\pi^+\nu\bar{\nu}}^{MIN}/\xi} - |\lambda_c \bar{X}| &< |\lambda_t X_t|.\end{aligned}\tag{59}$$

By maximizing \bar{X} , we obtain $|\lambda_t| > 2.355 \times 10^{-4}$.

In summary, from $\mathcal{B}(K^+ \rightarrow \pi^+ \nu \bar{\nu}) = (1.47_{-0.93}^{+1.60}) \times 10^{-10}$ (68% CL) the limits on λ_t are

$$\begin{aligned}0.236 \times 10^{-3} &< |\lambda_t| < 1.085 \times 10^{-3}, \\ -0.820 \times 10^{-3} &< \text{Re}\lambda_t < 1.085 \times 10^{-3}, \\ \text{Im}\lambda_t &< 0.928 \times 10^{-3}.\end{aligned}\tag{60}$$

From $\mathcal{B}(K^+ \rightarrow \pi^+ \nu \bar{\nu}) = (1.47_{-1.22}^{+2.83}) \times 10^{-10}$ (90% CL) the limits on λ_t are

$$\begin{aligned}0.107 \times 10^{-3} &< |\lambda_t| < 1.256 \times 10^{-3}, \\ -0.990 \times 10^{-3} &< \text{Re}\lambda_t < 1.256 \times 10^{-3}, \\ \text{Im}\lambda_t &< 1.099 \times 10^{-3}.\end{aligned}\tag{61}$$

The limits on $|V_{td}|$ are extracted from Equations (60) and (61) by using the measured limits $|V_{cb}| \simeq [0.039, 0.044]$ from PDG2004[6].

$$0.0054 < |V_{td}| < 0.0278 \quad (68\% \text{ CL}),\tag{62}$$

$$0.0024 < |V_{td}| < 0.0322 \quad (90\% \text{ CL}).\tag{63}$$

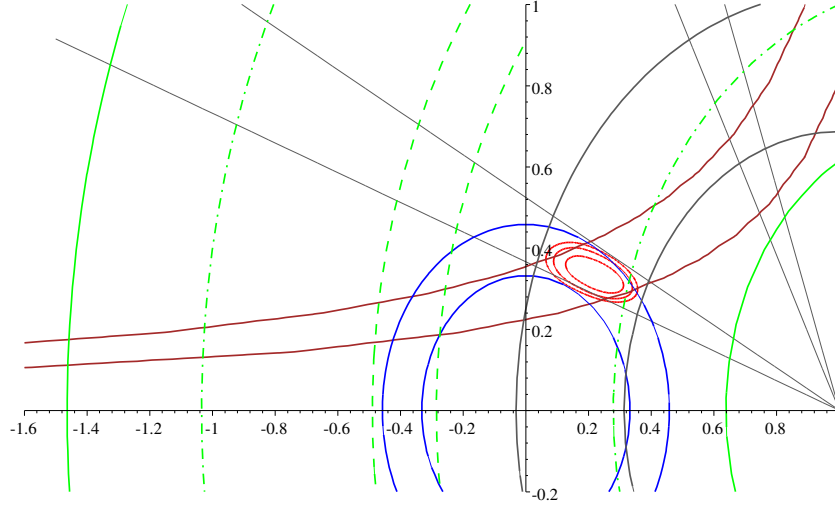


Figure 50: Impact of the $K^+ \rightarrow \pi^+ \nu \bar{\nu}$ branching ratio on the unitarity triangle [58]. The green lines indicate the constraints from the $K^+ \rightarrow \pi^+ \nu \bar{\nu}$ branching ratio (with theoretical uncertainty): central value (dashed), 68% CL interval (dot-dashed), 90% CL interval (solid). The red ovals show the 68%, 90%, 95% CL areas from other measurements ($|V_{ub}|$, ϵ_K , $\sin 2\beta$, Δm_d).

The latter is compared with the current experimental range of $|V_{td}|$, $0.0048 < |V_{td}| < 0.014$ in PDG2004[6]. The limits on $|V_{td}|$ obtained from our results are a bit wider than those from other measurements. Figure 50 shows the impact of the $K^+ \rightarrow \pi^+ \nu \bar{\nu}$ branching ratio on the unitarity triangle. The central value of the measured $K^+ \rightarrow \pi^+ \nu \bar{\nu}$ branching ratio does not intersect with the area of (ρ, η) constrained by $|V_{ub}|$, ϵ_K , $\sin 2\beta$, and Δm_d in other measurements, all of which support the SM prediction. This result is very interesting in that the discrepancy may indicate new physics. For example, once the constraints from the measurements of $\sin 2\beta$ and Δm_d , both of which are obtained from the $\Delta F = 2$ weak processes, are removed, the central value intersects with the area constrained by the other K and B decays in the region $\gamma > 90^\circ$ (Figure 51) [59]. The $K^+ \rightarrow \pi^+ \nu \bar{\nu}$ branching ratio should be measured precisely with more statistics and, with the measurement of the $K_L^0 \rightarrow \pi^0 \nu \bar{\nu}$ branching ratio, independent measurements of ρ and η from K and B decays are necessary to see whether there is a discrepancy or not.

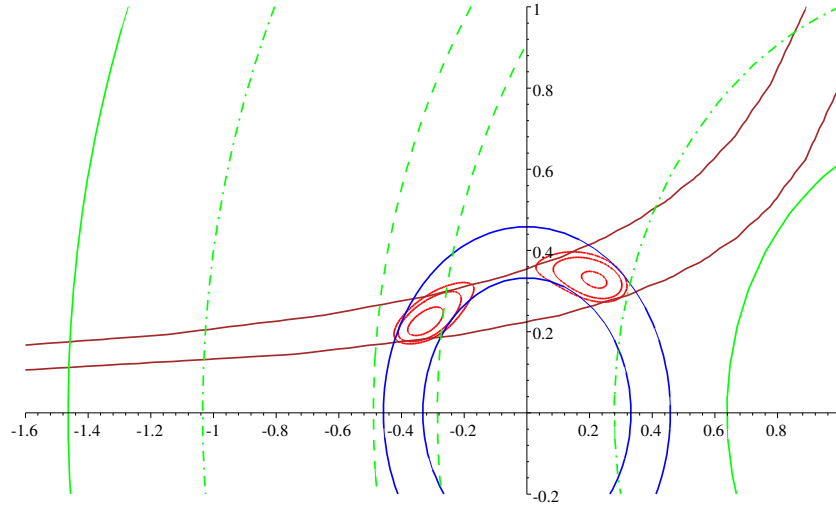


Figure 51: Impact of the $K^+ \rightarrow \pi^+ \nu \bar{\nu}$ branching ratio on the unitarity triangle excluding the constraints from the $\sin 2\beta$ and Δm_d measurements [58]. The green lines indicate the $K^+ \rightarrow \pi^+ \nu \bar{\nu}$ branching ratio (with theoretical uncertainty): central value (dashed), 68% CL interval (dot-dashed), 90% CL interval (solid). The red ovals show 68%, 90%, 95% CL areas from other measurements ($|V_{ub}|$ and ϵ_K).

5 Conclusion

The rare decay $K^+ \rightarrow \pi^+ \nu \bar{\nu}$ is a flavor-changing-neutral-current process and proceeds via 1-loop diagrams that mediate the top quark. This decay involves the coupling of top to down quarks. The branching ratio of $K^+ \rightarrow \pi^+ \nu \bar{\nu}$ is expressed by the magnitude of the CKM matrix element, $|V_{td}|$. Measuring $\mathcal{B}(K^+ \rightarrow \pi^+ \nu \bar{\nu})$ is one of the cleanest ways to extract $|V_{td}|$.

BNL-E949 is a successor to BNL-E787. The E949 detector was upgraded to achieve better measurements in the beam rate, twice that of E787. E949 examined stopped K^+ decays. A high-intensity K^+ beam was produced at the Alternating Gradient Synchrotron (AGS) by exposing 65 trillion protons per spill to a platinum target. Kaons with 710 MeV/c were transported to the E949 detector, and came to rest in a scintillating fiber target. 3.9×10^6 K^+ 's decayed at rest in the target per spill. The data were collected in 2002, which corresponded to 1.77×10^{12} K^+ decays.

The data were analyzed by a blind analysis. The Signal Region was masked out until the selection criteria were determined and the background levels were estimated. The development of the cuts and the estimation of the background levels were performed by using the Bifurcation Method. The Signal Region was enlarged compared to that in E787 with an increased confidence in the likelihood analysis. The enlargement of the Signal Region increased the acceptance by 30%. The total background level in the Signal Region was estimated to be 0.30 ± 0.02 events.

An examination of the Signal Region yielded one event near the upper kinematic limit of the $K^+ \rightarrow \pi^+ \nu \bar{\nu}$ decay. Based on the candidate event, an upper limit was set to be $\mathcal{B}(K^+ \rightarrow \pi^+ \nu \bar{\nu}) < 8.76 \times 10^{-10}$ at the 90% CL. E787 and E949 results were combined and the branching ratio was measured to be $(1.47_{-0.93}^{+1.60}) \times 10^{-10}$ at the 68% CL interval based on three events observed in the momentum region $211 \leq P \leq 229$ MeV/c. The measured branching ratio was twice as large as the SM prediction of $(0.78 \pm 0.12) \times 10^{-10}$, but was consistent within the error. At the measured central value of the branching ratio, the candidate event had a signal-to-background ratio of 0.9.

From the measured branching ratio, we set the limits on both $|\lambda_t|$ and $|V_{td}|$ to be

$$0.107 \times 10^{-3} < |\lambda_t| < 1.256 \times 10^{-3} \quad \text{and} \quad 0.0024 < |V_{td}| < 0.0322,$$

at the 90% CL interval, which was consistent with the current experimental range of $0.0048 < |V_{td}| < 0.014$ at the 90% CL interval.

References

- [1] W. Buchmiller, hep-ph/0306047
- [2] A.D. Sakharov, JETP Lett 5(1967) 24
- [3] V.A. Rubakov, M.E. Shaposhnikov, Usp. Fiz Nauk 166 (1996) 493; Phys. Usp. 39 (1996) 461; A Riotto and M. Trodden, Annu. Rev. Nucl. Part. Sci. 49(1999) 35.
- [4] M. Kobayashi and T. Maskawa, Prog. Theor. Phys. **49**, 652 (1973).
- [5] L. Wolfenstein, Phys. Rev. Lett. **51**, 1945 (1983).
- [6] Particle Data Group, S. Eidelman *et al.*, Phys. Lett. **B592**, 1 (2004)
- [7] C. Jarlskog, Phys. Rev. Lett. **55**, 1039 (1985); C. Jarlskog, Z. Phys. **C29**, 491 (1985); C. Jarlskog and R. Stora, Phys. Lett. **B208**, 268 (1988).
- [8] A.J. Buras, F. Schwab, and S. Uhlig, arXiv:hep-ph/0405132 (2004).
- [9] T. Inami and C.S. Lim, Prog. Theor. Phys. **65**, 297 (1981).
- [10] G. Buchalla and A.J. Buras, Nucl. Phys. **B548**, 309 (1999).
- [11] G. Buchalla and A.J. Buras, Nucl. Phys. **B398**, 285 (1993).
- [12] M. Musiak and J. Urban, Phys. Lett. **B451**, 161 (1999).
- [13] W.J. Marciano and Z. Parsa, Phys. Rev. **D53**, 1 (1996).
- [14] Particle Data Group, K. Hagiwara *et al.*, Phys. Rev. **D66**, 010001 (2002).
- [15] A.J. Buras, M.E. Lautenbacher, and G. Ostermaier, Phys. Rev. **D50**, 3433 (1994).
- [16] D. Rein and L.M. Sehgal, Phys. Rev. **D39**, 3325 (1989); J.S. Hagelin and L.S. Littenberg, Prog. Part. Nucl. Phys. **23**, 1 (1989); M. Lu and M.B. Wise, Phys. Lett. **B324**, 461 (1994); S. Fajfer, arXiv:hep-ph/9602322 (1996); C.Q. Geng, I.J. Hsu, and Y.C. Lin, Phys. Rev. **D54**, 877 (1996).
- [17] K. Anikeev *et al.*, Workshop Report "B Physics at the Tevatron: Run II and Beyond", arXiv:hep-ph/0201071 (2002).
- [18] A. Belyaev *et al.*, Kaon Physics working Group Report "Kaon Physics with a High-intensity Proton Driver", arXiv:hep-ph/0107046 (2001); G. Isidori, arXiv:hep-ph/0110255 (2001); G. Buchalla, arXiv:hep-ph/0110313 (2001).
- [19] A.J. Buras, arXiv:hep-ph/0402191 (2004); G. Isidori, arXiv:hep-ph/0301159 (2003).
- [20] A.J. Buras *et al.*, arXiv:hep-ph/0402112 (2004); A.J. Buras *et al.*, arXiv:hep-ph/0408142 (2004).

- [21] Y. Grossman and Y. Nir, Phys. Lett. **B398**, 163 (1997).
- [22] F. Wilczek, Phys. Rev. Lett. **49**, 1549 (1982); J.L. Feng *et al.*, Phys. Rev. **D57**, 5875 (1998).
- [23] S. Adler *et al.*, Phys. Rev. Lett. **79**, 2204 (1997).
- [24] S. Adler *et al.*, Phys. Rev. Lett. **88**, 041803 (2002); S. Adler *et al.*, Phys. Rev. Lett. **84**, 3768 (2000);
- [25] R. J. Oakes, Phys. Rev. **183**, 1520 (1969).
- [26] U. Camerini *et al.*, Phys. Rev. Lett. **23**, 326 (1969).
- [27] D. Ljung and D. Cline, Phys. Rev. **D8**, 1307 (1973).
- [28] J.H. Klems, R.H. Hildebrand, and R. Steining, Phys. Rev. **D4**, 66 (1971).
- [29] G.D.Cable *et al.*, Phys. Rev. **D8**, 3807 (1973).
- [30] Y. Asano *et al.*, Phys. Lett., **B107**, 159 (1981).
- [31] M.S. Atiya *et al.*, Phys. Rev. **D48**, R1 (1993).
- [32] M.S. Atiya *et al.*, Nucl. Instr. Meth. **A321**, 129 (1992).
- [33] S. Adler *et al.*, Phys. Rev. Lett. **76**, 1421 (1996).
- [34] B. Bassalleck *et al.*, E949 proposal, BNL-67247, TRI-PP-00-06 (1999), <http://www.phy.bnl.gov/e949/> .
- [35] T. Yoshioka *et al.*, IEEE Trans. Nucl. Sci. **51**, 199 (2004).
- [36] J. Doornbos *et al.*, Nucl. Instr. Meth. **A444**, 546 (2000).
- [37] D.A. Bryman *et al.*, Nucl. Instr. Meth. **A396**, 394 (1997).
- [38] M. Atiya *et al.*, Nucl. Instr. Meth. **A279**, 180 (1989).
- [39] E.W. Blackmore *et al.*, Nucl. Instr. Meth. **A404**, 295 (1998).
- [40] R.A. McPherson, "Chasing the Rare Decay $K^+ \rightarrow \pi^+ \nu \bar{\nu}$ ", Princeton University, Ph.D. Thesis, November, 1995.
- [41] I.H. Chiang *et al.*, IEEE Trans. Nucl. Sci. **42**, 394 (1995).
- [42] T.K. Komatsubara *et al.*, Nucl. Instr. Meth. **A404**, 315 (1998).
- [43] T. Yoshioka *et al.*, IEEE Trans. Nucl. Sci. **51**, 334 (2004).
- [44] blah blah
- [45] blah blah

- [46] blah blah
- [47] C. Caso *et al.*, European Physical Journal **C3**, 1 (1998).
- [48] P. Meyers, "A modified Version of the UMC Multiple Scattering Routine MSCAT1", E787 Technical Note No.77 (1985). Unpublished.
- [49] A.J. Stevens, "Nuclear Interactions in CH revisited", E787 Technical Note No.140 (1987). Unpublished.
- [50] W.R. Nelson *et al.*, "The EGS4 Code Syatem", SLAC 265, SLAC (1985).
- [51] T. Sekiguchi, "Development of Silicon Strip Detector for Rare Kaon Decay Experiments", University of Tokyo, Master Thesis, January, 2002.
- [52] N. Khovansky *et al.*, NIM. A351 (1994), 317
- [53] J.B. Birks, Proc. Phys. Soc. **A64**, 874 (1951).
- [54] The reference manual can be found in
<http://paw.web.cern.ch/paw/mlpfit/pawmlp.html>.
 The PDF version of the reference manual can also be available in
<http://schwind.home.cern.ch/schwind/MLPfit/doc/pawmlp.pdf>.
- [55] S. Adler *et al.*, Phys. Rev. Lett. **85**, 2256 (2000); M.R. Convery, "First Measurement of Structure Dependent $K^+ \rightarrow \mu^+ \nu_\mu \gamma$ ", Princeton University, Ph.D. Thesis, November, 1996.
- [56] T. Junk, Nucl. Instr. Meth. **A434**, 435 (1999).
- [57] The branchig ratio published by the E949 collaboration (V.V. Anisimovsky *et al.*, Phys. Rev. Lett. **93**, 031801 (2004)), $(1.47^{+1.30}_{-0.89}) \times 10^{-10}$, was based on a statistical technique developed by T. Junk [56].
- [58] Figures 50 and 51 are made by G. Isidori.
- [59] G. Isidori, arXiv:hep-ph/0307014 (2003); G. Isidori, arXiv:hep-ph/0301159 (2003).
- [60] G.J. Feldman and R.D. Cousins, Phys. Rev. **D57**, 3873 (1998).